

THE SIERRA MADRE ORIENTAL OROCLINE. PALEOMAGNETISM OF THE NAZAS SYSTEM IN NORTH-CENTRAL MÉXICO

Rafael Guerra Roel¹, Daniel Pastor-Galán², Gabriel Chávez-Cabello³, César Francisco Ramírez-Peña³, José Jorge Aranda Gómez⁴, Gerardo Patiño-Mendez¹, Giovanni Nova R⁵, Alejandro Rodríguez-Parra⁶, and Roberto Stanley Molina-Garza⁷

¹Universidad Autónoma de Nuevo León

²Universidad de Granada

³Universidad Autónoma de Nuevo León, Facultad de Ciencias de la Tierra

⁴Centro de Geociencias, Universidad Nacional Autónoma de México

⁵Instituto de Geociências, Universidade de São Paulo

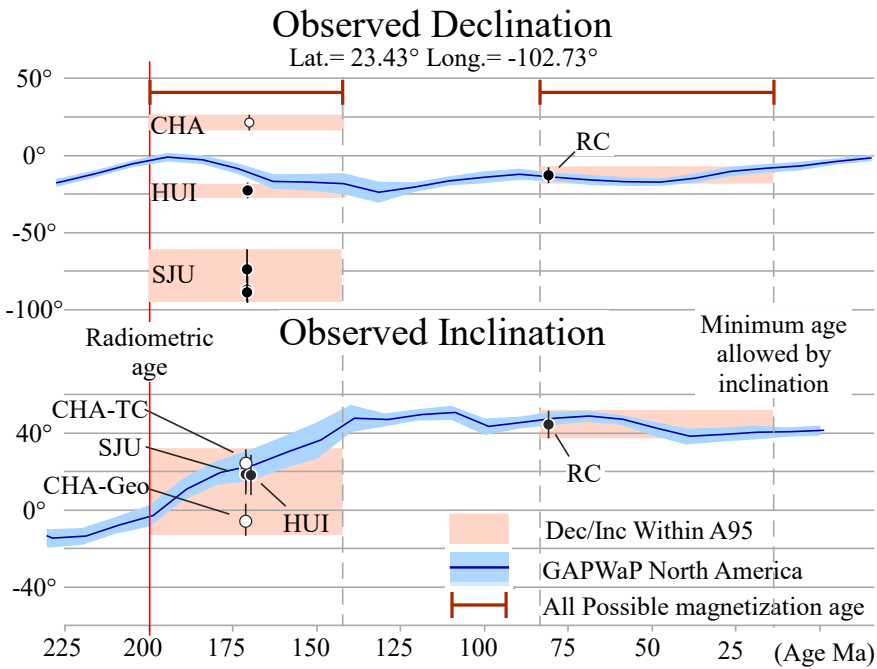
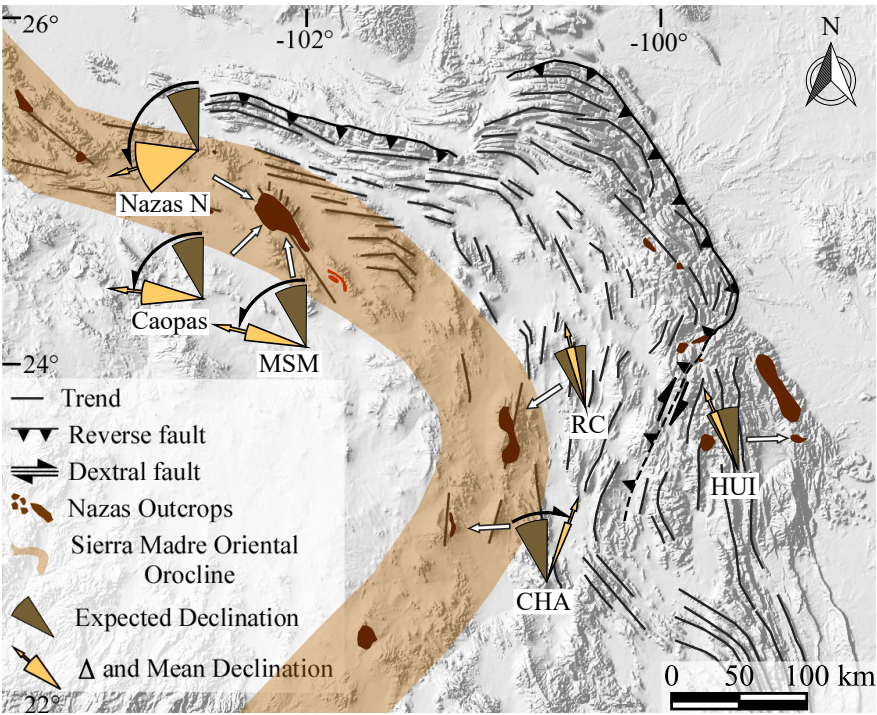
⁶Ministerio de Minas y Energía, Colombia

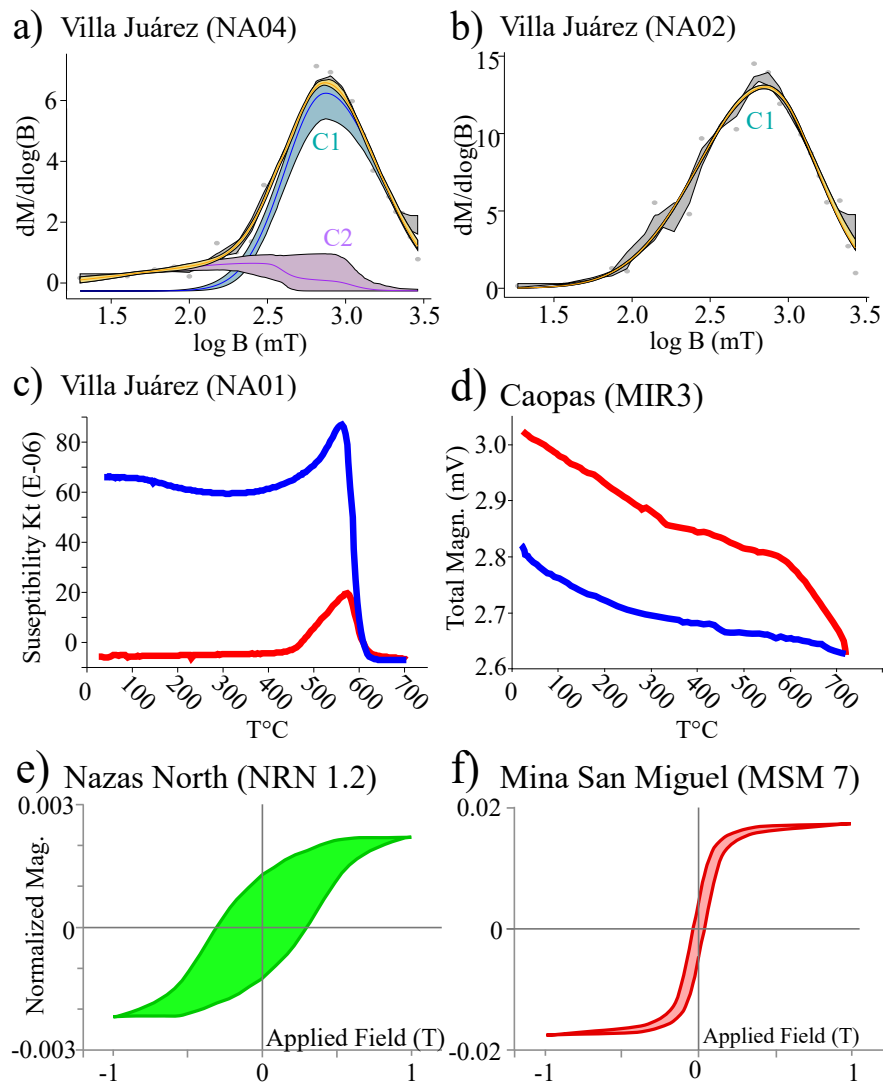
⁷Universidad Nacional Autónoma de México

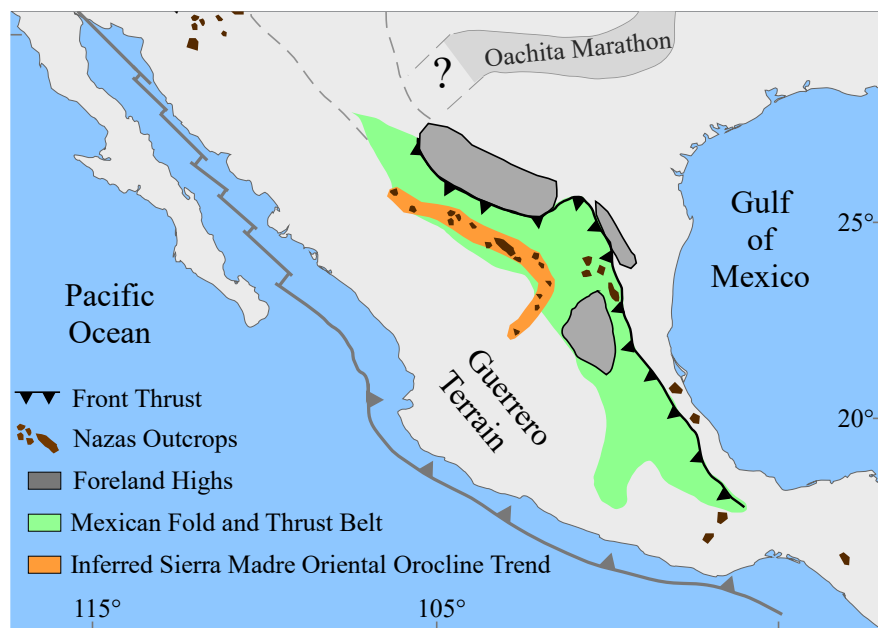
August 12, 2023

Abstract

Curved mountain belts are spectacular natural features, which contain crucial 3D information about the tectonic evolution of orogenic systems. The Mesozoic units exposed at the Cordilleran Mexican Fold and Thrust belt in NE Mexico show a striking curvature that has not been explained nor included in the existent tectonic models of the region. We have investigated with paleomagnetism and rock magnetism the kinematic history of that curvature, which is observed in the rocks of the Jurassic Nazas igneous province and its overlying red beds. Our results show a complex history of remagnetizations that occurred during the Late Jurassic and Cretaceous, as well as clockwise and counterclockwise vertical axis rotations of up to 50° respectively in each limb of the curvature. Although our data cannot provide precise timing for such rotations yet, our results confirm that the Mexican Fold and Thrust Belt underwent post-Late Jurassic orocline bending or bucking in NE Mexico.







The Sierra Madre Oriental Orocline. Paleomagnetism of The Nazas System in North-Central México

Rafael Guerra Roel¹, Daniel Pastor Galán^{2,3}, Gabriel Chávez-Cabello^{*4}, César Francisco Ramírez-Peña⁴, José Jorge Aranda Gómez⁵, Gerardo Patiño Méndez⁴, Giovanny Nova R.⁶, Alejandro Rodríguez-Parra⁷, Roberto Stanley Molina Garza^{†5}.

1 Universidad Autónoma de Nuevo León, Posgrado de la Facultad de Ciencias de la Tierra. Carretera a Cerro Prieto Km 8, Ex. Hacienda de Guadalupe, Linares N.L., México, C.P. 67700.

2 Universidad de Granada. Facultad de Ciencias de la Universidad de Granada. Av. de Fuente Nueva, s/n, 18071 Granada, España.

3 Frontier Research Institute for Interdisciplinary Science, Tohoku University, Japan.

4 Universidad Autónoma de Nuevo León, Facultad de Ciencias de la Tierra. Carretera a Cerro Prieto Km 8, Ex. Hacienda de Guadalupe, Linares N.L., México, C.P. 67700.

5 Universidad Nacional Autónoma de México, Centro de Geociencias, Juriquilla, Qro. 76230, México.

6 Instituto de Geociências, Universidade de São Paulo. São Paulo, Brasil

7. Ministerio de Minas y Energía, Colombia; Calle 43 # 57 -31, Can, Bogotá, Bogotá Colombia.

† Deceased

* Corresponding author: gabriel.chavezcbi@uanl.edu.mx

ABSTRACT

Curved mountain belts are spectacular natural features, which contain crucial 3D information about the tectonic evolution of orogenic systems. The Mesozoic units exposed at the Cordilleran Mexican Fold and Thrust belt in NE Mexico show a striking curvature that has not been explained nor included in the existent tectonic models of the region. We have investigated with paleomagnetism and rock magnetism the kinematic history of that curvature, which is observed in the rocks of the Jurassic Nazas igneous province and its overlying red beds. Our results show a complex history of remagnetizations that occurred during the Late Jurassic and Cretaceous, as well as clockwise and counterclockwise vertical axis rotations of up to 50° respectively in each limb of

the curvature. Although our data cannot provide precise timing for such rotations yet, our results confirm that the Mexican Fold and Thrust Belt underwent post-Late Jurassic orocline bending or bucking in NE Mexico.

KEYWORDS

Sierra Madre Oriental Orocline; Paleomagnetism; Mexican Fold and Thrust Belt; Remagnetization; Nazas Igneous Province.

1 Introduction

Orogenic belts are the most visible product of plate tectonics in the continents. Whereas their cross-section views are the most valuable source of information to understand orogenesis in 2D, their lateral variations are the best opportunity to understand their tectonic evolution and the curvature's kinematics in 3D (Gutiérrez-Alonso et al., 2008; Pastor-Galán, 2022). The kinematic classifications of orogenic curvatures (Johnston et al., 2013; Pastor-Galán et al., 2017; Sussman & Weil, 2004) distinguish (a) Primary arcs, which are those orogens whose curvature pre-dates the orogenic building (e.g., Jura mountains: Hindle & Burkhard, 1999); and (b) Oroclines (Carey, 1955) that are the orogenic curvatures product of vertical axis rotations. Oroclines can be classed as progressive oroclines: that is portions of orogens that were curved during the main deformation pulse, such as the Talesh (Rezaeian et al., 2020); and secondary oroclines, where the portion of an orogen was bent or buckled after the main deformation phase (e.g., the New England Oroclines, Li et al., 2012). The mechanisms that form oroclines may involve from the uppermost portion of the crust at the level where thrust faults develop (Marshak, 1988, 2004), to the whole lithosphere (Gutiérrez-Alonso et al., 2004; Pastor-Galán et al., 2012; Bagheri and Gol, 2020). Although many structural techniques can inform about the kinematics of curved orogens (Hindle & Burkhard, 1999; Kollmeier et al., 2000; Li et al., 2012; Pastor-Galán et al., 2011, 2014, 2017; Shaanan et al., 2014; Shaw et al., 2012; Weil & Yonkee, 2009; Yonkee & Weil, 2010; Bagheri and Gol, 2020), paleomagnetism is the best tool to do it, as the geomagnetic field is independent of the orogenic deformation (Abrajevitch et al., 2005; Eldredge et al., 1985; Pastor-Galán et al., 2015, 2018, 2020; Weil et al., 2001, 2010, 2013).

The American Cordillera runs along the Pacific coast of the Americas and includes several mountain belts (e.g., the Rockies, Sierra Madre Oriental and the Andes), extensive plateaus (Colorado, Atacama), primary curvatures (Colombian Eastern Cordillera: Jiménez et al., 2014); and oroclines (e.g., Alaska, Johnston, 2001; Panama, Montes et al., 2012; Bolivia, Eichelberger & McQuarrie, 2015; Patagonia, Maffione et al., 2010). The Sierra Madre Oriental is the northeastern portion of the Mexican Fold and Thrust Belt and shows a ~110 degrees curvature convex to the NE (Figure 1). The trend of this curvature is marked by outcrops of the Jurassic Nazas system (Nazas Igneous Province and associated sedimentary rock formations). This curvature has been interpreted as a primary arc representing the shape of the subduction zone during the Jurassic (Barboza-Gudiño et al., 2021; Barboza-Gudiño et al., 2014; Barboza-Gudiño et al., 2008; Dickinson & Lawton, 2001; Godínez-Urban et al., 2011; Lawton & Molina Garza, 2014; Martini & Ortega-Gutiérrez, 2018; Molina-Garza et al., 2020; Stern & Dickinson, 2010) or as the result of large-scale transcurrent faults that fragmented and displaced the Nazas system (Anderson et al., 2005; Anderson & Schmidt, 1983; Jones et al., 1995; Molina-Garza & Iriondo, 2005; Silver & Anderson, 1974). Lack of data precludes testing these or any other hypotheses since the map view kinematics of the Mexican Fold and Thrust Belt are woefully unknown. In this work, we analyze new paleomagnetic data from the Jurassic Nazas System along this curvature. Our results show counterclockwise and clockwise rotations that allow us to propose the existence of the Sierra Madre Oriental Orocline (Figure 1).

2 Geological Setting

The tectonic history of México during the past 250 million years is coupled with the eastward subduction of the Kula-Farallon (Paleo-Pacific) plates under the North American plate (Fitz-Díaz et al., 2018 and references therein). The interaction of continental and oceanic plates along the Pacific coast formed a ~ 5000 km long arc where voluminous calc-alkaline- to alkaline magmatism occurred. The arc extended from northwestern Canada (DeCelles et al., 2009) to southern México (Campa-Uranga et al., 2004; Godínez-Urban et al., 2011) and included the Nazas igneous province (a.k.a. Mesozoic arc of Western North America or the Nazas Rift Province; Barboza-Gudiño et al., 2008; Busby & Centeno-García, 2022). This magmatic subprovince was active from the beginning of the Jurassic (~200 Ma) to the Callovian (~165 Ma) (Barboza-Gudiño et al., 2008; Bartolini et al., 2003; Busby & Centeno-García, 2022; Grajales-Nishimura et al., 1992; Jones et al., 1995; Parolari et al., 2022). From Late Triassic to Earliest Cretaceous, the effects of the breakup of Pangea combined with extension related to the roll-back of the paleo-pacific plates in western

Pangea formed a series of continental and marine basins (Barboza-Gudiño et al., 2021; Busby, 2023; Martini & Ortega-Gutiérrez, 2018; Pindell & Kennan, 2001), such as the broad Mesozoic Basin of Central México (Figure 1). In the northeastern portion of that basin, sedimentation began with the accumulation of eroded materials derived from the Nazas Igneous Province. The continued extensional setting during the Oxfordian (~160 Ma) triggered a large marine transgression responsible for the accumulation of a ~ 5 km thick marine sedimentary succession (hereafter “sedimentary cover”; Bartolini et al., 1999; Goldhammer, 1999; Gray & Lawton, 2011; Hernández-Romano et al., 1997; Ocampo-Díaz et al., 2016). In the studied area (Figure 2), there is evidence of ~165 Ma plutonism. The laccolithic emplacement of the Caopas pluton (Anderson et al., 1991; Guerra-Roel, 2019; López-Infanzón, 1986; Ramírez-Peña, 2017) transferred vertical and horizontal stresses that locally deformed the overlying rocks. Afterwards, due to the accretion of the Guerrero terrain during the Early Cretaceous (Busby, 2023; Centeno-García et al., 2008; Martini et al., 2013; Ortega-Flores et al., 2020) the sedimentary rocks of the Mesozoic Basin of Central Mexico were incorporated into the Mexican Fold and Thrust Belt. The Mexican Fold and Thrust Belt style of deformation is dominated by folds and thrusts that developed over a regional decollement (i.e., thin-skinned) where the sedimentary cover was transported in a northeast direction with fold wavelengths that increase from West to East (Eguiluz et al., 2000; Fitz-Díaz et al., 2018 and references therein). The age of regional folding in the hinterland of the Mexican Fold and Thrust Belt, syntectonic plutonism (Teyra and Peñuelo plutons Ramírez-Peña & Chávez-Cabello, 2017) and synorogenic clastic sedimentation (Concepción del Oro Formation; Ocampo-Díaz et al., 2016) has been bracketed between 90 and 65 My (Fitz-Díaz et al., 2018; Ramírez-Peña & Chávez-Cabello, 2017). The Mexican Fold and Thrust Belt contains several recesses (e.g., Torreón and Potosí) and salient that portray obstacle tectonics with the forland highs (Monterrey, Figure 2; e.g., Chávez-Cabello et al., 2004; Nemkin et al., 2019; Padilla y Sánchez, 1985; Zachary, 2012). In localized areas along the trace of the Mexican Fold and Thrust Belt late high angle reverse faults cut the older folds and thrusts and expose Jurassic volcanic strata and, in some cases, Paleozoic basement (Chávez-Cabello et al., 2005; Fitz-Díaz et al., 2018; Guerra Roel, 2019; Mauel et al., 2011; Ramírez-Peña et al., 2019; Ramírez-Peña & Chávez-Cabello, 2017; Zhou et al., 2006).

2.1 The Nazas Igneous Province

The volcanic rocks of the Nazas Igneous Province (i.e., the Nazas Formation in México) crop out scattered in a winding band that crosses north-central México, and turns from a NW trend to a SE direction (Figure 1). The band is sub-parallel to the general trend of the Mexican Fold and Thrust Belt (Figure 2) The type locality of the Nazas Formation is in Cerritos Colorados near Villa Juárez,

Durango (Figure 2a; Lawton & Molina Garza, 2014; Pantoja-Alor, 1972). Isotopic ages of these rocks suggest a diachronic evolution of volcanism, with the oldest rocks (190 Ma) in the South (Barboza-Gudiño et al., 2008; Jones et al., 1995; Lawton & Molina Garza, 2014; López-Infanzón, 1986) and the youngest (160 Ma) in the northern part of the band (González-León et al., 2021; Mauel et al., 2011).

The Nazas Formation is a volcanic succession of lava flows, ignimbrites and volcanic breccias of andesitic to rhyolitic compositions interbedded with siliciclastic sediments (Barboza-Gudiño et al., 2021; Lawton & Molina Garza, 2014; Pantoja-Alor, 1972 and references therein). Its thickness is variable and ranges from 250 m to 1000 m (Clemons & McLeroy, 1965; Pantoja-Alor, 1972). Some hypabyssal and intrusive bodies with the same chemical composition and age have been attributed to the Nazas Igneous Province. These bodies are peraluminous and are interpreted as an arc setting (Barboza-Gudiño et al., 2021; Barboza-Gudiño et al., 2008; Bartolini et al., 2003; González-León et al., 2021; Mauel et al., 2011) or a rift environment as partial melting products of the Panafrican crust (Busby, 2023; Busby & Centeno-García, 2022; Martini & Ortega-Gutiérrez, 2018; Parolari et al., 2022). Bartolini et al. (2003) summarized all the reported ages of the Nazas Formation. Lawton & Molina Garza, (2014) published an updated list that included some correlated volcanic units in the United States and included zircon U-Pb ages of 180-178 Ma for the Lower member and 170-169 Ma for the Upper member. The youngest recorded ages (U-Pb in zircon) in México attributable to the Nazas Igneous Province yielded 158.1 ± 1 Ma and come from intrusive bodies exposed in Sonora (González-León et al., 2021).

2.2 Red Beds

In some localities, the top of the Nazas Formation is overlaid by a Jurassic pre-Oxfordian sedimentary succession of red sandstone, siltstone, conglomerate, breccia, and volcanoclastic reddish beds that have a direct contribution from the igneous province. These materials were deposited in continental to marine transitional environments. They are commonly addressed as Jurassic red beds and have been defined as La Joya and La Boca Formations (Barboza-Gudiño et al., 2008, 2010; Fastovsky et al., 2005; Imlay et al., 1948; Mixon et al., 1959; Rubio Cisneros et al., 2011b).

The La Boca Formation has two informal members. The lower member consists of lapilli tuffs, lava flows, volcanic breccias, and ignimbrites interbedded in equal proportion with volcanoclastics and detritus derived primarily from coeval volcanic rocks that represent deposits from the Nazas Igneous Province (Rubio-Cisneros & Lawton, 2011). The volcanic component in the La Boca

Formation gradually decreases towards the top of the stratigraphic unit. The lower and upper members are separated by an angular unconformity that ranges from a few degrees to 70°, an angle that increases in the vicinity of intrusions (Rubio-Cisneros & Lawton, 2011). The upper informal member of this formation is mostly red siliciclastic strata. These rocks fine upwards in a conglomerate, sandstone, and siltstone succession lacking fossil material (Fastovsky et al., 2005). La Boca Formation is overlain by La Joya Formation a siliciclastic unit with a basal fining upward conglomerate to reddish siltstone and mudstone. It was deposited in continental to a marginal marine environment with subordinate freshwater limestone and is overlain by the upper Jurassic-Paleogene sedimentary cover that starts with the Oxfordian Minas Viejas evaporites (Padilla y Sánchez, 1985; Rubio-Cisneros & Lawton, 2011; Salvador, 1987). The reported maximum depositional age for the La Boca Formation is 184 -183 Ma for the lower member and 167 Ma for the upper member (Rubio-Cisneros & Lawton, 2011). As for the La Joya formation its age has been inferred by stratigraphical correlation, however, Barboza-Gudiño et al. (2012) reported zircon ages as young as 166.2 ± 1.9 Ma at the top of this unit in Real de Catorce and Rubio-Cisneros & Lawton, (2011) reported a U-Pb zircon age of 163.6 ± 2.6 at its base in Huizachal Valley. Barboza-Gudiño et al., (2021) presented a complete summary of the stratigraphy and lithological correlations of all the known localities of the Nazas Igneous Province in Mexico.

During the last recorded episode of horizontal crustal shortening of the Mexican Fold and Thrust Belt (Upper Cretaceous-Eocene), these Jurassic units were exhumed in some parts of the thrust belt (Figure 2b; Fitz-Díaz et al., 2018; Gutiérrez-Navarro et al., 2021; Lawton & Molina Garza, 2014; Ramírez-Peña et al., 2019; Ramírez-Peña & Chávez-Cabello, 2017).

3 Sampling Strategy

We collected a total of 620 core samples of 2.5 cm diameter with a gas-powered drill and oriented them with a Pomeroy orienting fixture and a Brunton Pocket Transit compass. 355 cores come from the Nazas Formation and the remainder 265 from the red bed formations that overlay it. In some localities, we collected oriented blocks and later drilled them in the laboratory. The Nazas Formation samples were collected in three separate localities representing different trends of the Nazas Igneous Province (Figure. 2a): (1) Villa Juárez locality in the state of Durango, located 20 km west of the city of Torreon, Coahuila; (2) The San Julián Uplift locality, in the northern part of the state of Zacatecas; and (3) Charcas which is located 7 km west of the city of the same name in the state of San Luis Potosí. The sedimentary rocks were collected from the La Joya and La Boca Formations: (1) Real de Catorce located in the Sierra de Catorce also in the state of San Luis

Potosi; and (2) in the Huizachal Valley, 18 km SE of the city of Ciudad Victoria, Tamaulipas (Figure 2b).

3.1 Villa Juárez, Durango (25.501°N, -103.621° E)

The local age of the volcanic rocks in this locality is 200-178 Ma for the lower member and 170-169 Ma Upper member (Barboza-Gudiño et al., 2021; Lawton & Molina Garza, 2014). We collected between 2 and 3 oriented blocks in each of the 17 sites (labeled NA01-NA17) from 4 individual andesitic lava flows. We obtained a total of 85 cores from the oriented blocks. Lava flows are interbedded with volcano-sedimentary rocks in the Villa Juárez anticline, which has an axial trend and plunge of $\sim 315^\circ/18^\circ$. The sampled limbs do not show noticeable evidence of penetrative deformation. Although the precise age of the folding is unknown, the structure is attributed to thin-skinned deformation coupled with the buttressing effect of the Coahuila block, an adjacent basement high. Sediments accumulated in the basin were thrust over the southern margin of the block during the Late Cretaceous (Lawton & Molina Garza, 2014).

3.2 San Julián Uplift (24.837°N, -102.174° E)

The San Julian Uplift is a basement block that contains the largest outcrop of the Nazas Formation in México. The block was exhumed during Eocene-Oligocene thick-skinned tectonic event (Guerra-Roel, 2019; Ramírez-Peña, 2017; Ramírez-Peña et al., 2019; Ramírez-Peña & Chávez-Cabello, 2017). The thick-skinned faults cut in high angles the pre-existing Cretaceous thin-skinned structures, which formed during the early stages of development of the Mexican-Fold and Thrust Belt. The NE limit of the San Julián Uplift is the Las Norias fault zone, a high-angle reverse fault that disrupted and refolded the overlying anticlines tilting them towards the NE (Guerra-Roel, 2019, Ramírez-Peña 2017).

In this locality, the Nazas Igneous Province system is represented by volcanosedimentary, volcanic, and sub-volcanic rocks of the Nazas Formation, and the Caopas intrusive body (Gómez-Torres, 2022; López-Infanzón, 1986; Ramírez-Peña, 2017; Rogers et al., 1963). The volcanic rocks of the Nazas formation upper member are primarily composed of andesitic and dacitic lava flows, volcanic domes, and associated volcanic breccias. The Nazas Formation lower member is locally constituted of metasedimentary material, tuff, ash, breccia, and andesitic lava flows. These rocks show foliation and low metamorphic grade of greenschist facies with chlorite as the main metamorphic mineral. The zircon U-Pb age for the Nazas Formation in this locality is 174 ± 2 Ma (Ramírez-Peña, 2017). The Caopas intrusive corresponds to a Middle Jurassic plutonic body of

intermediate composition emplaced in the Nazas Formation. This body shows a porphyritic texture and, in some of its upper parts, evidence of dynamic metamorphism (porphyroblasts and mineral lineation). The Caopas intrusive yielded a U-Pb in zircons age of 165 ± 3 Ma (Ramírez-Peña, 2017).

From this locality, we collected a total of 256 samples in three separate areas: Mina San Miguel (coded MSM), Nazas North (ALI, NRN), and the Caopas intrusive body (MIC, MIR, MIRN; supplementary table ST2). The samples corresponding to the Mina San Miguel were collected in an anticline at the eastern border of the San Julián Uplift; and the Nazas N sites came from the northern part of the block. All the samples belonging to the MSM area and sites Mic1, Mic2, and Mic3 of the Caopas intrusive were drilled in situ (10-15 samples per site). The rest of the sites of the Caopas area (Mic4 – Mic7) were collected as oriented blocks (one per site). From each block, we obtained four cores in the laboratory. The poor outcrop exposure of the lava flow succession in the MSM and Nazas N areas, together with their thickness (20-30 m), weathering conditions, and compositional and textural similarities among flows made the task of identifying individual lava flows a challenge.

The Nazas Formation in the MSM area shows folds with trend/plunge of $142^{\circ}/10^{\circ}$ that is oblique to the main East-West trend of the structures in the transversal sector of the Mexican Fold and Thrust Belt (see Parras thrust in Figure 2). A second series of younger folds with N- to NE-trends was recognized by Ramírez-Peña (2017) and Guerra Roel (2019). This structural trend is absent in rocks of the Nazas Formation, but it is characteristic of the eastern borderline structures of the San Julián Uplift.

3.3 Charcas, San Luis Potosí (23.131°N , -101.188°E)

The Nazas Formation in Charcas is composed by lava flows and pyroclastic rocks of andesitic composition, interbedded with volcanoclastic material and volcanic breccias. These rocks were dated (U-Pb in zircon) in 179 ± 1 Ma (Zavala-Monsiváis et al., 2012). Jurassic red beds overlie unconformably the Nazas Formation. The structure and exhumation mechanism has not been studied in detail in this locality, and it is only described as an anticlinorium. However, it is noted that the structure is in the same crustal block as the Real de Catorce locality (see 3.4).

In this locality we collected samples along the San Antonio River covering about 80 m of the exposed stratigraphic succession of the Nazas Formation. The outcrop is composed by a stack of lava flows, and volcanic breccia of andesitic composition interbedded with thin ignimbrites and

ash-fall tuffs. 60 cores were collected in 10 sites of the Nazas Formation labeled **CHA-1 to CHA-10** that cover four different andesitic lava flows, interbedded tuff, and epiclastic deposits. Each sampled site corresponds to distinct units no thicker than 2 m, with the exception of sites CHA-1 and CHA-2 that were collected from a single epiclastic deposit.

3.4 Real de Catorce (23.621°N, -100.855° E)

In this locality, the older rocks crop out in the core of an antiformal stack (Gutiérrez-Navarro et al., 2021). The antiformal stack structure formed between 91-52 Ma, based on an $^{40}\text{Ar}/^{39}\text{Ar}$ age obtained from neogenic illite collected from a shear zone (Gutiérrez-Navarro et al., 2021). The cooling ages of ~50 Ma (U-Pb-He in zircon) from a dacitic pluton emplaced in the Nazas Formation have been interpreted as the exhumation age due to deep high-angle reverse faults (thick-skinned event), which delimit the Real de Catorce block. The Nazas Formation unconformably rests atop Triassic clastic rocks of the Potosí fan (Centeno-García et al., 2005; Silva-Romo et al., 2000) and yielded U-Pb age of 174.7 ± 1.3 Ma in zircon. (Barboza-Gudiño et al., 2012). The La Joya Formation lies unconformably over the Nazas Formation. In this locality, The La Joya Formation is composed of a 200 m thick sedimentary succession of continental (bottom) to marginal marine (top) conglomerates, sandstones, and shale in a grain-decreasing order from bottom to top. This Formation shows signs of deformation features that suggests that it acted as a decollement, which was developed in the Late Cretaceous during the thin-skinned deformation event (Gutiérrez-Navarro et al., 2021). The La Joya Formation's maximum depositional U-Pb age, inferred from detrital zircons is 166.2 ± 1.9 Ma (Barboza-Gudiño et al., 2012).

We sampled 103 cores in the Real de Catorce area in a coarsening upward 60 m thick succession of sandstones. The samples were collected on the fine-grain portion of the outcrop and distributed in 16 sites labeled **RC11 - RC26**. Each core accounts for a single bed.

3.5 Huizachal Valley (23.588°N-99.222° E)

The locality contains outcrops of the Nazas Formation in the core of a structural dome overlain by the Jurassic red beds of the La Boca and La Joya Formations (Rubio-Cisneros & Lawton, 2011). The top of the Nazas Formation is interbedded with the clastics of the lower member of La Boca Formation and they are separated by an angular unconformity. This lower member consists of lapilli tuffs, lava flows, volcanic breccias, ignimbrites and rhyolites interbedded with volcanoclastics with detritus derived primarily from volcanic rocks of the Nazas igneous province.

The volcanic component in the La Boca Formation gradually decreases towards the top of the stratigraphic unit (Rubio-Cisneros & Lawton, 2011). The La Boca Formation has been divided into two informal members separated by an angular unconformity that ranges from few degrees to 70° (Rubio-Cisneros & Lawton, 2011). The upper member consists of a fining upwards red beds succession that includes conglomerate, sandstone, and siltstone beds with scant fossils (Fastovsky et al., 2005). La Boca Formation is overlain by La Joya Formation. Both formations were deposited in continental to marginal marine environments (Rubio Cisneros et al., 2011a; Salvador, 1987). Detrital zircon analysis in this locality places the maximum deposition age of the La Boca Formation at ~190 Ma (Rubio-Cisneros & Lawton, 2011), as for the La Joya Formation maximum depositional age, inferred from detrital zircons is ~166 Ma (Venegas-Rodríguez et al., 2009). We drilled 105 samples from La Joya and La Boca Formations in this locality. The sampled formations crop out at the core of an anticline along the valley. Seven sites, with a total of 45 samples, labeled **HUI42 – HUI48** correspond to La Boca Formation, which consists of fine to coarse red sandstones. Samples were collected in the middle portion of the upper member, closer to the anticline axis. 62 cores distributed in nine sites labeled **HUI28 – HUI40** were collected from the La Joya Formation on the northwestern limb of the anticline, in an outcrop that lays along a secondary dirt road approximately 1 km SW from the previously sampled La Boca Formation. Each site sampled comprises a single stratum of about two meters thick.

4. Methods and Results

4.1 Isothermal Remanent Magnetization (IRM) and Hysteresis Loops

4.1.1 Villa Juárez

Isothermal Remanent Magnetization (IRM) curves were obtained at the Paleomagnetism and Magnetism Laboratory at the Centro de Geociencias of the Universidad Nacional Autónoma de México. The procedure was carried out using an in-house built impulse magnetizer which is capable of generating fields up to 5 T. The acquired magnetization was measured in a JR6 spinner magnetometer from AGICO. Eleven samples belonging to eight sites in the Villa Juárez locality were selected for IRM acquisition curves (NA01, NA02, NA05, and NA10 of andesitic and tuff composition along with volcano-sedimentary samples labeled NA04, NA06, NA07, NA08). In this process, we induced an IRM in a progressively increasing field (20 – 2900 mT) and afterward, we

applied a back-field demagnetization in a progressive order (10 – 700 mT) following the method described by Kruiver et al. (2001)

IRM curves were unmixed using the MAX Unmix web application (Maxbauer et al., 2016) to determine the main magnetic minerals contributing to the cumulative IRM. The Gradient Acquisition Plots (Figures 4a and 4b) show two components in the coercivity spectra. One with a mid-saturation value $\log B_{1/2}$ between 2.85 and 3 (Figure 3b), and a second one between 1.7 and 2. Most of the results show a gradual increment towards the 1 T and higher and the samples do not reach saturation at 3 T. From the analyses, we infer two mineral phases with distinct coercivities, a “soft phase” that we identified as magnetite with H_{cr} that varies between 50 – 100 mT and a “hard phase” with values between 700 and 1000 mT, possibly hematite. The main contribution to the coercivity spectra is given by the $\log B_{1/2} > 100\text{mT}$ and $< 1000\text{mT}$, which is usually accredited to phases of hematite and is present in both volcanic and volcano-sedimentary rocks of this locality. The remaining IRM unmixing graphs are available in Supplementary file SF1.

4.1.2 San Julián

IRM and hysteresis loops were obtained in a Micromag model 2900 with two Tesla magnets, Princeton Measurements Corporation, noise level $2 \times 10^{-9} \text{ Am}^2$ in the Paleomagnetism and Magnetism Laboratory at the Centro de Geociencias of the Universidad Nacional Autónoma de México. Curves were measured on representative specimens of the sampled localities. These tests were made at room temperature and a field of 1 T was applied in 10 mT increments. The results show noisy curves and are similar for most of the samples. The minerals that hold the NRM for the volcanic samples reach saturation in the range below 400 mT suggesting that their remanence is controlled by ferrimagnetic phases (probably Ti-magnetite; Gubbins & Herrero-Bervera, 2007; Supplementary file SF2).

At the same time, we also measured hysteresis loops at room temperature on a Micromag model 2900 with two Tesla magnets, Princeton Measurements Corporation, noise level $2 \times 10^{-9} \text{ Am}^2$. In total we measured 26 representative samples. Samples mass ranged from 40 to 50 mg and were measured using a P1 phenolic probe. The maximum applied field was 1 T in increments of 20 mT on an average time of 600 ms. The coarse grain texture of the Caopas intrusive along with the scarcity of magnetic mineralogy resulted in noisy results (dia-/para- magnetic) for the intrusive rock samples. Although the curves did not reach saturation at 1 T, interpretable results both show

hysteresis loops that resemble those of superparamagnetic magnetite (grain size <10 nm; Dunlop & Özdemir, 1997) with a possible minor content of a hard phase (likely hematite: Figure 3f). The NRN sites of the sampled andesites from Nazas North area (Figure 3e) also shows a hysteresis loop with a high coercivity phase that does not saturate at 1 T, we also interpret this phase as hematite (Gubbins & Herrero-Bervera, 2007).

4.2 Thermomagnetic curves

4.2.1 Villa Juárez

We performed the thermomagnetic curves for this locality in the Ivar Giæver Geomagnetic Laboratory (University of Oslo) on a Kappabridge AGICO MFK1-FA equipped with a CS-4 furnace and processed with Cureval8 (AGICO) (Chadima & Hrouda, 2009) and were corrected for stability values and density. We measured the magnetic susceptibility in runs from 0° to 700 °C in an Ar atmosphere in nine selected pulverized samples. Irreversible curves are evident due to mineralogical alterations during heating, in most of the curves a drop in susceptibility is noticed around the Curie temperature for low Ti-magnetite (~580 °C), and in some cases a less evident drop around the Néel temperature (~700 °C) for hematite (Figure 2c and supplementary file SF5).

4.2.2 San Julián

We performed one thermomagnetic analysis per site in the San Julián locality in an in-house built horizontal translation type Curie balance with a sensitivity of approximately 5×10^{-9} Am² in the Paleomagnetism and Rock Magnetism Laboratory of the Centro de Geociencias, Universidad Nacional Autónoma de México (UNAM, Querétaro). Due to the small amounts of magnetic material in some of the samples, the tests were carried out on concentrates previously separated using hand magnets. Between 300 to 400 mg of ground, sample was used for each experiment. The Curie balance was programmed to continuously heat the sample to 700 °C and gradually cool to room temperature at heating and cooling rates of approximately 10 °C min⁻¹.

Curves for all the volcanic samples progressively demagnetized when heating, some samples showed sharp drops in magnetization in temperatures between 600 and 700 °C indicative of hematite (O'Reilly, 1984). In other samples (e.g., MSM7), magnetization started to decrease around the 500 °C (supplementary file SF4b), which may indicate the coexistence of magnetite and hematite (Dunlop & Özdemir, 1997). Some curves showed a subtle presence of sulfides

suggested by a small magnetization increase between 400 and 500 °C (e.g., De Boer & Dekkers, 1998). On all the volcanic samples we could only see a major phase with mineralogical alteration during heating, commonly hematite to maghemite due to temperature increment (Dunlop & Özdemir, 1997), and in some cases paramagnetic curves (Gubbins & Herrero-Bervera, 2007). Samples from the Caopas intrusive show analogous behavior as the volcanic samples (Supplementary file SF4a).

4.3 Anisotropy of Magnetic Susceptibility (AMS)

Anisotropy of magnetic susceptibility (AMS) is a sensitive technique that has several applications. We applied this methodology as a proxy for describing deformation in weakly deformed rocks (e.g., Parés, 2015; Weil & Yonkee, 2009). Graphically we represent AMS as an ellipsoid whose principal axes are $k_{\max} > k_{\text{int}} > k_{\min}$ (e.g., Parés, 2015 and references therein). The shape of the AMS ellipsoid depends on different features such as the orientation of mineral grains, compositional layering, the crystallographic orientation of individual minerals, distribution, and size of microfractures, and the grain shape and size (e.g., Butler, 1992; Tarling & Hrouda, 1993). The analyses were carried out in a Kappabridge model KLY-3 in the Paleomagnetism and Rock Magnetism Laboratory of the Centro de Geociencias, Universidad Nacional Autónoma de México (UNAM) in Juriquilla Querétaro, México. We present the AMS ellipsoid in terms of equal area projection (Figure 4) and shape parameter graphs both Flinn, (1962) and Jelinek, (1981) diagrams available in Supplementary file SF6.

4.3.1 San Julián

AMS results for this locality show uniform mean anisotropies close to the mean ($K_m \approx 592.7 \times 10^{-9}$) for both the Caopas and MSM areas. The anisotropy value (P) is low for the MSM area (< 1.02). In contrast, the Caopas intrusive shows slightly higher and more variable values (1.032-1.343). The results for both areas show pseudo-isotropic geometries and no apparent penetrative deformation. The MSM locality, Kmin axes are parallel to the poles of the lava-flow bedding describing an antiformal structure (Figure 4a). After unfolding, the Kmin axes group on the vertical, following the bedding data, suggesting a pre-folding vertical fabric (Figure 4a). The Caopas intrusive and the MSM areas show low anisotropy values that are archetypal pseudo-isotropic geometries. The Caopas intrusive locality shows a good grouping of the Kmin axis on the vertical which is representative of an internally undeformed intrusive body that only recorded the effects

of magmatic flow and gravity (Figure 4d). At the same time, the general direction of the magnetic lineation (Kmax) corresponds to the direction of the mineral lineation (NE-SW) observed on the field (Guerra- Roel, 2019).

4.3.2 Villa Juárez

The mean anisotropy value (Km) varies per site from 1.95×10^{-05} to 1.59×10^{-04} with mean values of 7.36×10^{-05} . And most of the samples show oblate shapes with low degree of anisotropy ($P = 1.026$). The results of the AMS ellipsoid show widespread distribution and poor grouping (Figure 4b). This behavior could represent an undeformed volcanic rock, which is consistent with field observations.

4.3.3 Charcas

The magnetic susceptibility (Km) in the analyzed samples from the Charcas locality, varies from 120.9×10^{-06} to 335.3×10^{-06} with a mean value of 207.8×10^{-06} and a $P = 1.24$. Samples from sites CHA1, CHA2, CHA4, CHA9, and CHA10 show oblate geometries. Sites CHA3, CHA5, and CHA8 show both prolate and oblate, and CHA6 and CHA7 only show prolate geometries (Supplementary file SF6). Kmin axes are parallel to the poles of the bedding except for sites CHA2, CHA3, and CHA6. AMS in Charcas seems to respond, at least partially, to loading (Figure 4c).

4.4 Scanning Electron Microscopy (SEM) and polarized light Microscopy

We analyzed the samples using a Scanning Electron Microscope (SEM) model TM-1000 Hitachi equipped with energy-dispersive X-ray spectroscopy (EDS: Oxford). This procedure was done in the Laboratory of Crustal Fluids in the Centro de Geociencias, Universidad Nacional Autónoma de México (CEGEO UNAM, Querétaro).

4.4.1 Villa Juárez

The SEM images were complemented with EDS scans that showed percentages of the elements present in the minerals (Supplementary file SF7). The images for this locality show the presence of Ti-Magnetite set in a non-conductive granular matrix (Figure 5a). Additionally, lamellar hematite crystals were observed in this locality (Figure 5b, see also supplementary file SF7).

4.4.2 San Julián

The results show the presence of anhedral magnetite crystals surrounded by hematite weathering rims. Hematite is also present as a secondary mineral that filled the fractures and, to a lesser extent, along the crystal cleavages of amphibole phenocrysts. These two magnetic mineral phases are the most prominent in the samples from this locality (Figures 5c and 5d, see also supplementary file SF7).

4.5 Paleomagnetism

We progressively demagnetized the samples using thermal (TH) and alternating fields (AF) demagnetization procedures. The paleomagnetic directions were analyzed with Paleomagnetism.org software (Koymans et al., 2016, 2020), which uses principal component analysis to define magnetic components (Kirschvink, 1980) and Fisher (1953) statistics to calculate averages and errors in directions and virtual geomagnetic poles (VGPs). Only directions with five or more demagnetization steps in line and maximum angular deviation (MAD) $< 15^\circ$ (McElhinny & McFadden, 1999) were considered as valid directions. We applied a 45° cut-off in each site to discard outlying points. We also used the McFadden & McElhinny (1988) method of combining great circles and best-fitted set point directions for samples where components were difficult to isolate (Figure 6). Two localities allow for a fold test (MSM and Real de Catorce localities: Figure 7).

Additionally, the reliability of each data set was tested with Deenen et al. (2011) criteria, that in general terms evaluates the scatter of VGPs. This criterion denotes that the ellipticity of the VGP scatter is the effect of paleosecular variation (PSV) and that a proper VGP distribution tends to be circular. Nonetheless, unaccounted structural corrections, inclination shallowing, and or vertical axis rotations may add additional scatter (ellipticity) to the associated distribution. Finally, to test the reliability of data from unique lava flows, we have compared the differences between the average of site means within a locality against the average of all individual directions (Figure 7). Summary of locality means is shown in Table 1.

Most of the samples from all localities show a low temperature/low coercivity component ($< 200^\circ\text{C}$ and $< 16\text{ mT}$.) that roughly fits with the Geo-axial dipole (GAD) expected for NE México during the Holocene. We interpret this component as a viscous remanent magnetization. (*e.g.*, Figure 6a) (Supplementary file SF8).

4.5.1 Villa Juárez (Nazas Formation)

The samples of this locality were demagnetized and measured in the shielded room of the Ivar Giæver Geomagnetic Laboratory in Norway. We demagnetized the samples in progressive variable steps using thermal and alternating fields demagnetization using a furnace model MMTD8oA for TH and an alternating fields demagnetizer model LDA-3A. After initial pilot tests, we determined that AF demagnetization was ineffective due to the presence of a high coercivity mineral (hematite). The NRM was measured in a superconducting rock magnetometer WSGI model 755 (2G Enterprises). The Zijderveld diagrams (Zijderveld, 1967) show a single component that progressively demagnetizes to the origin (Figure 6d). The ChRM components were isolated at high temperatures (~450 – 700 °C). At the site level, the direction means show high precision parameters in all samples but three ($k > 45$), whereas 5 out of 10 sites with $n > 3$ samples show $k > 100$, which we consider spot readings of the geomagnetic field. However, site averages do not concentrate ($k < 2$, without a cut-off and $k = 13$ after discarding more than half of site averages). Some site directions may represent reversed chrons, however, data is too scarce to confirm. For this reason, we were not able to obtain a mean dec/inc of this locality (results are available in Supplementary Table ST1).

4.5.2 San Julián Uplift (MSM, Caopas, and Nazas North)

We analyzed the samples from this locality in the paleomagnetism and rock magnetism laboratory in the Centro de Geociencias, UNAM Querétaro. The remanent magnetization was measured using an AGICO JR-6 spinner magnetometer. Thermal (TH) and Alternating Field (AF). Demagnetization was performed in a magnetically shielded room using a shielded furnace with a heating capacity up to 640 °C in increasing steps of 50 °C up to 500 °C. From 500 °C to 640 °C was finished 20 °C increments. After pilot tests, we determined that AF demagnetization was ineffective due to the presence of a high coercivity mineral (hematite).

Upon demagnetization, we identified a Characteristic Remanent Magnetization (ChRM) with a downward inclination and westerly direction, isolated between 500°-580 °C and 40-60 mT. We named this component W (for west). This component was present in 12 sites of the MSM locality (Figure 6a), 15 sites of the Caopas intrusive (Figure 6b), and 7 sites of the Nazas N (Figure 6e) in a total of 129 samples (for site mean parameters see Supplementary Table ST2). The W component in the MSM area shows a mean dec/inc of 285°/ 21° (geographic coordinates) downward and single polarity with a k of 10 and $K = 17.4$. The VGP projection is well rounded and the A95 value is in between the maximum and minimum of the Deenen (2011) envelope, suggesting that the

observed distribution scatter can be explained only as a function of the PSV. The dispersion (k) at the site level ranges between 20-50 with only MSM5 and MSM3 over 200 and MSM10 with the lowest (13) (Table 1). The fold test (Tauxe & Watson, 1994) shows a maximum between 1 and 31% unfolding (Figure 7a). This negative fold test reveals that the W component in MSM is the product of a post-folding remagnetization. The average of means and overall average show akin results (Figure 7a).

The W component in the Caopas intrusive shows progressive demagnetization and high unblocking temperatures between 400 and 560 °C (Figure 6b), and an average dec/inc 271°/ 17° in geographic coordinates (Figure 7c) with a precision parameter $k=10$. The VGPs plotted for this area have a K of 13.40 and an A95 of 5.66 in between the A95min and A95max envelope (Table 1). The VGP plot reveals an elliptical shape, elongated W-E (Figure 7c). Despite being within Deenen's limits, we think that the elliptical shape indicates an external cause of additional scatter apart from PSV. We suspect an unaccounted structural or magnetic acquisition problem. Thus, we used this result with caution.

The last group of samples in the San Julián Uplift "Nazas North" behaves similarly but with larger dispersion for the W component. This locality lies on the northern part of the San Julián Uplift and they lack reliable structural correction due to poor exposure in the area. The mean dec/inc of the W component is 261°/26° and has a dispersion parameter $k=8.3$. With almost 20° of Δ inclination and 11° Δ declination (Table 1). The directions in this area seem to follow a great circle and it shows an elongated W-E VGP projection (Figure 7e). Its A95 of 11.21 is larger than Deenen's A95max, indicating additional sources of scatter not attributable to PSV. Although we cannot precisely identify the additional source of scatter, we think that it might be due to unidentified structural problems or magnetic acquisition. "Nazas North" area did not provide a dataset with enough quality to quantify vertical axis rotations or latitudinal motion. However, its average declination and inclination are analogous to MSM and Caopas intrusive areas reinforcing their meaning.

4.5.3 Charcas (Nazas Formation)

We performed part of the paleomagnetic analyses of this locality in the Paleomagnetism and Rock magnetism Laboratory of the Universidad Nacional Autónoma de México, Centro de Geociencias (UNAM, Querétaro) with an AGICO JR-6 spinner magnetometer. The rest of them were processed

in the University of Texas at Dallas (UTD, Geoscience Department Paleomagnetism and Rock Magnetism Lab) with the use of a cryogenic magnetometer 2G Enterprises. All demagnetization process was performed with AF. The components isolated by this procedure show a straight demagnetization line to the origin (Figure 6c) with low MAD (<5), only on sites CHA1, CHA9, and CHA10 (17 samples). Samples from sites CHA3, 4, 5, and 6 (22 samples) show little demagnetization, due to the presence of hematite, but all of them tend to the origin with analogous directions to CHA9 and CHA10. The component was isolated between 35 and 90 mT. CHA3 to CHA10 group well with a $\text{dec/inc} = 22^\circ/-05^\circ$ and $k = 53$; $K = 76$; and $A95 = 2.58$ (Table 1). Samples from CHA1 and CHA2 are different and discardable by any statistical cut-off criterion (Figure 7f). The dispersion parameter before and after tectonic correction is $k > 50$ and $K > 70$ in both specimen and site mean averages (Supplementary table ST3). This data suggests that sites CHA3-CHA10 represent a single spot-reading of the geomagnetic field, either because all sample layers represent a single cooling unit or because they were quickly remagnetized later.

4.5.4 Real de Catorce (Red beds “La Joya Formation”)

The samples were measured in the laboratories of the UNAM Querétaro and at UT Dallas, Texas. These samples were thermally demagnetized in progressive steps from 100 °C up to 670 °C. Samples show a single ChRM component showing a gradual demagnetization to the origin (Figure 6f). Overall results group around two sets of directions: one with $\text{dec/inc} = 358^\circ/40^\circ$ and $k = 45$, which is similar to the Holocene GAD for México; and a second one with reverse polarity $\text{dec/inc} = 166^\circ/42^\circ$ and $k = 41$. These two directions do not share a bootstrapped common true mean direction (Tauxe, 2010). However, they are not far from it, being the reversed component slightly rotated counterclockwise ($< 10^\circ$) (Figure 7b). The data of this locality allowed for a fold test (Tauxe & Watson, 1994) (Figure 7b). The fold test is negative with a maximum grouping between -15% to -5% unfolding. The VGPs projection shows a rounded shape (Figure 7b). By flipping the reversed directions, we obtain a mean dec/inc of $346^\circ/42^\circ$ with a k value of 41 (see Table 1, for site means see also supplementary table ST4).

4.5.5 Huizachal Valley (Red beds “La Joya and La Boca Fm”)

The samples of the Huizachal locality were analyzed in the laboratories of the UNAM, Juriquilla, Querétaro and at UT Dallas, Texas. We demagnetized all samples thermally following progressive heating steps from 100 °C up to 670 °C (Figure 6g). We identified a component isolated in the

temperature range between 450 °C and 650 °C combining 57 directions with 33 great circles (McFadden & McElhinny, 1988). This component has a mean dec/inc of 160°/-26° upwards with a $k = 14$, $K = 22$, and $A95 = 3.5$ (Table 1 for site means see also supplementary table ST5). The VGPs projection shows a roughly circular shape with a slight ellipticity W-E possibly indicating tectonic-induced scatter (Figure 7d).

5 Discussion

The curvature of the Sierra Madre Oriental that the Nazas System draws in North Central México has been mostly overlooked. The Nazas Igneous Province outcrop pattern has been interpreted as the result of: (1) Large scale left lateral faulting during the Late Jurassic (Anderson et al., 2005; Anderson & Schmidt, 1983; Jones et al., 1995; Molina-Garza & Iriondo, 2005; Silver & Anderson, 1974), or (2) The direct result of a curved segment in the subduction zone, thus representing a primary arc in the kinematic classification for curved orogens (Barboza-Gudiño et al., 2014; Barboza-Gudiño et al., 2008; Dickinson & Lawton, 2001; Godínez-Urban et al., 2011; Lawton & Molina Garza, 2014; Martini & Ortega-Gutiérrez, 2018; Molina-Garza et al., 2020; Stern & Dickinson, 2010). In our investigation of the studied area, we have found a tangled history of remagnetizations and vertical axis rotations, which are the result of a complex tectonic history that involved orocline bending or buckling.

5.1 Magnetization processes and timing: a complex puzzle

Our sample collection came from the Nazas system in NE México as defined by different authors (Barboza-Gudiño et al., 2004; Busby & Centeno-García, 2022; Lawton & Molina Garza, 2014; Parolari et al., 2022; Rubio-Cisneros & Lawton, 2011; Zavala-Monsiváis et al., 2012). All available data from these outcrops suggest that they share the same tectonic history and define an ~110° curvature (Fitz-Diaz 2018). The Mesozoic and Cenozoic geological history of NE México is complex and includes a wide range of tectonic processes: such as subduction, transtension, terrain accretion, folding and thrusting, and extension; all of them capable of producing remagnetizations and vertical axis rotations.

We think that the Villa Juárez locality is the only one from our collection whose magnetization is primary. Each site from this locality corresponds to a single lava flow. Lava flows cool quickly and record snapshots of the magnetic field. Therefore, many lava flows representing enough time

are needed to average out PSV (Deenen et al., 2011; Gerritsen et al., 2022). Most of our sites from the Villa Juárez locality show high concentration parameters (k) that are consistent with spot-readings of the geomagnetic field (Deenen et al., 2011; Gerritsen et al., 2022; Figure 7g and Supplementary table ST1). Although some remagnetization processes can produce high concentration parameters (e.g., Pastor-Galán et al., 2021) they usually remagnetize all lava flows from a rather small sampling area like Villa Juárez. In this locality, the average declination and inclination obtained from each lava flow differ noticeably (Figure 7g), and site averages fail to group around VGPs that resemble the GAD's PSV despite the strong consistency within each lava flow. We think that this particular result is the consequence of a primary magnetization acquired during the 195-180 Ma lapse, a time when the magnetic field was quite unstable and reversed and excursed frequently (e.g., Ogg, 2020). Unfortunately, our sampling did not include a large enough number of lava flows to average such a highly variable PSV. The dataset, therefore, does not meet the current reliability criteria (e.g., Gerritsen et al., 2022; Meert et al., 2020). In this locality, we have identified magnetite and hematite as the magnetic carriers (Figures 3a, 3b, and 3c). SEM images (Figure 5a and 5b) show a texture of well-formed euhedral to subhedral crystals of magnetite and hematite with no apparent neo-forming minerals, signs of alteration, weathering, nor apparent penetrative deformation, which supports the primary magnetization origin for Villa de Juárez locality. We, therefore, interpret an Early Jurassic (195 ± 7 My) magnetization corresponding with lava cooling (Barboza-Gudiño et al., 2021).

The samples collected at three areas of the San Julián Uplift locality (Mina San Miguel, Caopas, and Nazas North) contain the same two main magnetic carriers (hematite + magnetite), both documented in rock magnetic analyses (Figures 3d, 3e, and 3f) and in SEM studies (Figures 5c and 5d). However, in the MSM area hematite is associated with a secondary texture (newforming) as it appears to fill crystallographic cleavages and secondary cracks in other minerals (Figure 5d). This mineralogical ensemble together with a negative fold test (Figure 7a) indicate that NRM, at least for the MSM area, is the product of a post-folding remagnetization. The similarity between the obtained directions in the three areas in geographic coordinates and the lack of observed reversals recorded in them support the idea that the areas of Caopas and Nazas N were also (re)magnetized at the same time as the MSM area. All three areas of the San Julián Uplift locality show shallow inclinations (Figure 8) that fit the expected inclination for the Late Jurassic following Torsvik et al., (2012) Global APWP (GAPWaP) adapted for NE México (Koymans et al., 2016; Koymans et al., 2020).

Previous studies have interpreted the MSM anticline as a drape fold formed together with the reverse fault that exhumed the San Julián Uplift during the Eocene (Guerra Roel, 2019; Patiño-Mendez, 2022; Ramírez-Peña & Chávez-Cabello, 2017). However, the inferred age of folding (Eocene) and the post-folding magnetization but with shallow inclinations consistent with a Jurassic origin observed in this locality are incompatible (Figure 8). One option that explains the results could be a quick post-Eocene remagnetization of the studied samples that yielded a biased shallow inclination as a consequence of insufficient PSV averaging. However, this hypothesis is weak since the VGP circular shape and k parameters are both compatible with a correct averaging of the PSV. We think that our data supports a Late Jurassic remagnetization, and that the emplacement of igneous rocks is the best candidate to blame for this remagnetization event. So far, the only Jurassic deformation event described in the studied localities was caused by the emplacement of the plutonic intrusions ~165 Ma, such as the Caopas laccolith. This broadly spaced magmatism includes the emplacement of several intrusions at the Huizachal Valley (Fastovsky et al., 2005; García-Obregón, 2008; Rubio Cisneros, 2012; Rubio Cisneros et al., 2011c), which are blamed for originating the angular unconformities of 10° to 70° between the upper and lower members of La Boca and the one at the contact between La Boca and La Joya formations exposed in the vicinities of intrusions in the Huizachal Valley. We think that the intrusion of the Caopas laccolith might be large enough to generate at least part of the local antiformal structure in the San Julian Uplift. Subsequent cooling of the Caopas laccolith and post-emplacement fluid circulation would be the cause for the remagnetization.

We found eight sites (CHA3 to CHA10) in the Charcas locality that show a large directional consistency with a $k = 52$ at specimen level and $k = 87$ when considering the average of the site means. Such results indicate that either CHA3 to CHA10 sites correspond with a single cooling unit or that all sites were quickly remagnetized at the same time (Figure 6c and 7f Supplementary table ST3). CHA-1 and CHA-2 sites yielded very different directions (Figure 7f). Their differences might be explained either by an extreme PSV event during acquisition (either primarily or during a remagnetization) or by two or three different magnetization events. Unfortunately, our dataset is not large enough to support any of these or an alternative hypothesis.

The rocks sampled at the Huizachal and the Real de Catorce localities show distinctive red color that suggests the presence of pigmentary hematite at first glance. Therefore, we foresaw hematite as a magnetic carrier. Samples from both localities showed a high-temperature component, which was unblocked from 600 °C to the Néel temperature of hematite (700 °C). Samples from the Real

de Catorce locality did not pass the fold test, implying that their magnetization was acquired after folding (Figure 7b). Folding in the area has been dated (Ar-Ar in illite) in the age range between 90 and 70 Ma (Gutiérrez-Navarro et al., 2021). In contrast to San Julián Uplift locality, the inclinations are steeper in Real de Catorce and fit with those expected for Cretaceous and younger rocks (< 140 Ma; Figure 8). The occurrence of double polarity in them indicates that the samples did not remagnetize, or at least not completely, during the Cretaceous superchron that ended ~83 Ma (Ogg, 2020). Hypothesizing a precise age of remagnetization is challenging, but considering the folding age and the documented double polarity, we think that the probable causes are: (1) the initial thrusting of the Mexican Orogen, which in this area started during the Cenomanian (Gutiérrez-Navarro et al., 2021); and (2) the thin-skinned deformation event that lasted until the Late Cretaceous-Early Eocene (Gutiérrez-Navarro et al., 2021). We cannot rule out, however, a later (e.g., Eocene-Oligocene) remagnetization.

The fold test of the Huizachal locality (Supplementary files SF9) is inconclusive, and we do not have another field test to ascertain a relative timing for the magnetization. Nonetheless, we found no reversals registered in the samples from this locality, which spans over 18 million years of the Jurassic (184 – 166 Ma). We think that a secondary magnetization for the locality can better explain our results, as the geomagnetic field during that lapse in the Jurassic was extremely variable (Ogg, 2020). However, the inclinations (Figure 8), fit with a Late Jurassic remagnetization, no younger than 140 Ma, as they did in the San Julian Uplift locality.

5.2. Significance of vertical axis rotations curvature of the Sierra Madre Oriental in North Central México

Our results from the San Julián Uplift and Charcas locality show significant vertical axis rotations with respect to the expected declinations following the GAPWaP of Torsvik et al. (2012; Figure 9). The data of the San Julián uplift locality (MSM 285°/20°, Caopas 271°/17°, and Nazas N 272°/21°) shows > 59° of counterclockwise rotation regardless of the time of the remagnetization (Figures 8 and 9). In contrast, the Charcas data (020°/01°) show a potential clockwise rotation of up to ~30°. The data from Charcas seems to be a single spot-reading evidenced by its high *k* and *K* values. Therefore, we cannot use it to quantify vertical axis rotations. However, the deviation from the GAPWaP is large enough to, at least, suspect that there may be a significant clockwise rotation. The mean direction obtained (346°/42°) in the Real de Catorce locality, does not differ from the expected declination for anytime younger than 160 Ma (Figures 8 and 9).

To our knowledge, the main tectonic events that may explain the observed rotations in NE México are: (1) The Late Jurassic-Early Cretaceous extensional-transtensional (right lateral) event responsible for the opening of the Gulf of México and the translation of the Yucatan block (Martini & Ortega-Gutiérrez, 2018; Pindell & Kennan, 2001) and/or the Nazas back-arc extension (Busby, 2023; Barboza-Gudiño et al., 2021; Dickinson and Lawton, 2001); (2) the Early to Late Cretaceous closure of the Mesozoic Basin of Central México during the Guerrero Superterrane accretion (Centeno-García et al., 2008; Martini et al., 2016; Ortega-Flores et al., 2020) and the subsequent formation of the Mexican Fold and Thrust Belt (Fitz-Díaz et al., 2018 and references therein); (3) the Eocene thick-skinned deformation event (Chávez-Cabello et al., 2005; Guerra-Roel, 2019; Gutiérrez-Navarro et al., 2021; Mauel et al., 2011; Patiño-Mendez, 2022; Ramírez-Peña et al., 2019; Ramírez-Peña & Chávez-Cabello, 2017) and (4) the Basin and Range extension event (Henry and Aranda-Gómez, 1992; Aranda-Gómez & McDowell, 1998; Del Pilar-Martínez et al., 2020; Nieto-Samaniego et al., 1999)

The vertical axis rotations documented in the studied localities seem to correlate with the changes in the trend of the regional structures in each locality (Figure 9) suggesting that the inferred curvature (Figure 9) is an orocline *sensu* Johnston et al. (2013) and Pastor-Galán et al. (2017). The Nazas system in NE Mexico represents the base of the stratigraphic successions exposed at the Sierra Madre Oriental in addition, the curvature and the trend of the Mexican Fold and Thrust Belt in NE México are roughly parallel, a fact that suggests a genetic relationship between them (Figure 2). For these reasons, we term the structure the Sierra Madre Oriental Orocline. Preliminarily, we hypothesize two scenarios for the formation of Sierra Madre Oriental Orocline:

(1) The observed rotations of the Nazas system could have started during the late stages of the opening of the Mesozoic Basin of Central México and were amplified during the development of the Mexican orogen (c.f., Fitz-Díaz et al., 2018). In this case, the curvature of the Nazas system would be a secondary orocline. Whether this feature is of crustal or lithospheric scale is yet to be determined. The curvature drawn by the Late sedimentary cover (the Late Jurassic-Cretaceous rocks resting atop the rocks of the Nazas system; Figure 2) could be either: (a) a primary feature that mimics the original shape of the sedimentary basin, a case similar to the Jura mountains (e.g., Hindle & Burkhard, 1999); or (b) a progressive orocline formed due to the tightening of the preexisting curvature during the development of the Mexican Fold and Thrust Belt (Fitz-Díaz et al., 2018), akin to the Sevier belt in the U.S.A. (e.g., Yonkee & Weil, 2015).

(2) The curvature of the Nazas System in NE México is the result of thin-skinned tectonics developed during Late Cretaceous-Paleogene differential shortening. This phenomenon progressively tightened the curvature and caused opposite rotations on each end of the thrust sheets, which simultaneously affected both the Nazas System and the younger sedimentary cover exposed at the Sierra Madre Oriental.

The existence of an orocline bending or buckling event of such magnitude is an intriguing event that can modify the way the tectonic history of Northeastern Mexico has been interpreted. However, we realize that data is still scarce, incomplete, and scattered. We urge for more and better paleomagnetic and structural data to solve this new and exciting challenge.

6. Conclusions

- We have documented a Late Jurassic, widespread, remagnetization event that affected the Nazas System (i.e., the Nazas Formation and overlying red bed formations) in NE Mexico. The 165 Ma plutonism is the best candidate to trigger that event. We have also found another remagnetization event that we dated as young as 75 Ma.
- Rocks of the Nazas System underwent significant vertical axis rotations, which are congruent with the orientations of regional structures exposed in Mexican Fold and Thrust Belt in Northeastern Mexico.
- The recognized rotations in the Nazas system suggest orocline bending or buckling and not a primary curvature.
- We propose the Sierra Madre Oriental Orocline, which is a $\sim 110^\circ$ curved mountain belt that spans from Durango to San Luis Potosí states in Northeastern Mexico, for a distance of at least 450 km.

Acknowledgments

RGR thanks the CONAHCYT for the support in the form of a doctoral scholarship, and also the funding provided by a Ramón y Cajal Fellow granted to DPG (RYC2019-028244-I) funded by MCIN/AEI/ 10.13039/501100011033 and by the “European Social Fund Investing in your future”. **DPG** is funded by a Grant PID2021-128801NA-I00 funded by MCIN/AEI/10.13039/501100011033, a Ramón y Cajal Fellow RYC2019-028244-I funded by MCIN/AEI/ 10.13039/501100011033 and by the “European Social Fund Investing in your future”, and a Leonardo grant 2022 to researchers and cultural creators (LEO22-2-3010) from the bank BBVA. **GCC** is grateful for the support from PAICYT projects: CT1248-20, CT1626-21, and 36-CAT-2022. **JJAG** gratefully acknowledges PAPIIT UNAM grants IN106820 and IG101523. **GN** thanks the Mexican Science Agency (CONAHCYT) for the support in the form of a MSc scholarship. We appreciate the support of Professor John W. Geissman for the access to the University of Texas paleomagnetism laboratory. Part of the data sets in this paper are the late **Roberto Stanley Molina Garza’s** unpublished work, a friend and a mentor that will be missed.

Data Availability

Raw and interpreted Paleomagnetic data will be uploaded and available in open access servers that respect the FAIR principles such as paleomagnetism.org, MagIC and/or Zenodo when the article is accepted for publication. Data will also be available at reviewer’s request if needed.

Captions

Figure 1. Distribution of the Nazas outcrops in México and the alleged trend of the Sierra Madre Oriental Orocline. Dashed lines in the upper part of the map show the inferred orogen continuity in northern Mexico and southern USA. The Mesozoic Basin of Central México is represented as the Mexican Fold and Thrust Belt (modified from Fitz-Díaz et al., 2018).

Figure 2. (a) Synthetic geological map and regional distribution of the localities sampled in northeastern México. (b) General trend of the inferred curvature of the Sierra Madre Oriental Orocline. Note the presence of the Monterrey salient and the Potosí and Torreón recesses, and the distribution and localization of the Nazas Formation and associated Red beds outcrops. Acronyms: **Cd. V**= Ciudad Victoria; **CHA**= Charcas; **GM**= Gulf of México; **HV**= Huizachal Valley; **Mat**= Matehuala; **Mty**= Monterrey; **PO**= Pacific Ocean; **RC**= Real de Catorce; **SJU**= San Julián Uplift; **Tor**= Torreón; **SMO**: Sierra Madre Oriental; **VJ**= Villa Juárez) (Modified from open-source vector data from INEGI, 2023; and SGM, 2023)

Figure 3. Rock magnetic properties graphs of representative samples. (a) and (b) Gradient Acquisition plots of IRM acquisition curves of the Villa Juárez locality using MAX UnMix

(Maxbauer et al., 2016). Grey dots and the yellow curve represent the smoothed IRM data and modeled coercivity distribution, respectively. Shaded areas represent 95% confidence intervals associated with each component. These plots show mid saturation ($B_{1/2}$) of 1.7 for (a) and 2.85 for (b), magnetite, and hematite phases, respectively. (c) Magnetic susceptibility (Kt) vs. temperature ($^{\circ}\text{C}$) curve for the Villa Juárez locality showing Hematite. (d) Total magnetization vs. temperature ($^{\circ}\text{C}$) for the Caopas intrusive showing hematite and magnetite unblocking temperatures. Red and blue lines represent heating and cooling, respectively. The hysteresis loops were executed in magnetic field increments of 20 mT on an average time of 600 ms and are corrected for paramagnetic-diamagnetic influence. The Nazas North loop (e) shows a high coercivity shape (probably hematite), and the Mina San Miguel Locality shows a thin waist loop that we interpret as magnetite (f).

Figure 4. AMS results represented in an equal area projection for the analyzed sites in the (a) Mina San Miguel, (b) Villa Juárez, (c) Charcas show results of the volcanic rocks of the Nazas Formation, and (d) Caopas intrusive. Larger symbols represent site mean values. Light blue lines represent bedding. Shape parameter T vs Mean magnetic susceptibility K_m , and shape parameter T vs Anisotropy parameter P graphs, show low degree of anisotropy (Supplementary file SF6).

Figure 5. Scanning Electron photomicrographs of representative samples of the Nazas Formation in the localities of Villa Juárez and Mina San Miguel. Photomicrographs of samples collected at the Villa Juárez locality (a and b) show Fe oxides with compositions and texture of primary magnetite, Ti-magnetite, and hematite; the MSM locality Photomicrographs from Mina San Miguel samples show primary magnetite with alteration rims of hematite and hematite that grew in the fractures of an amphibole crystal.

Figure 6. Representative directions of the Nazas Formation are expressed in Zijderveld (1967) diagrams, and fitted great circles. (a) Mina de San Miguel locality, (b) Caopas Intrusive, (c) Charcas, (d) Villa Juárez, (e) Nazas North, and from the Red Beds localities. (f) Real de Catorce, and (g) Huizachal in Geographic Coordinate system. **AF** = Alternating Fields, **TH** = Thermal Demagnetization. **PCA** = Principal Component.

Figure 7. Equal area projections of the direction vectors of all the localities, their overall mean, site average and site average means. Bootstrapped fold test of the Mina de San Miguel and Real de Catorce localities. The projections show behavior of paleomagnetic directions during unfolding from 0% (geographic) to 100% (Tectonic). (a) Mina San Miguel locality with Foldtest. (b) Real de Catorce **Geo** = geographic; **Tec** = Tectonic; **VGP** = Virtual Geomagnetic Poles (locality mean parameters see Table 1)

Figure 8. Observed declinations and inclinations from sampled localities and Global Apparent Wander Path of the study area for North America (Torsvik et al., 2012) calculated with Paleomagnetism.org (Koymans et al., 2016, 2020). All localities are represented in geographic

coordinates except Charcas. Acronyms: **CHA-GEO** = Charcas in Geographic Coordinates; **CHA-TC**= Charcas in Tectonic Coordinates; **HUI** = Huizachal Valley; **RC** = Real de Catorce; **SJU** = San Julián Uplift.

Figure 9. Vertical axis rotations and structural trend of the area (**SJU** = San Julián Uplift; **HUI** = Huizachal Valley; **RC** = Real de Catorce; **CHA**= Charcas). The yellow fields represent the expected declinations from 200 Ma to present day (Torsvik et al., 2012). Direction means (observed declinations) within the expected direction range (yellow) are considered not rotated. Δ Dec: Calculated error for direction mean.

References

Abrajevitch, A. V., Ali, J. R., Aitchison, J. C., Badengzhu, Davis, A. M., Liu, J., & Ziabrev, S. V. (2005). Neotethys and the India–Asia collision: Insights from a palaeomagnetic study of the Dazhuqu ophiolite, southern Tibet. *Earth and Planetary Science Letters*, 233(1), 87–102. <https://doi.org/10.1016/j.epsl.2005.02.003>

Anderson, T. H., McKee, J. W., & Jones, N. W. (1991). A northwest trending, Jurassic Fold Nappe, northernmost Zacatecas, Mexico. *Tectonics*, 10(2), 383–401. <https://doi.org/10.1029/90TC02419>

Anderson, T. H., & Schmidt, V. A. (1983). The evolution of Middle America and the Gulf of Mexico–Caribbean Sea region during Mesozoic time. *Geological Society of America Bulletin*, 94(8), 941. [https://doi.org/10.1130/0016-7606\(1983\)94<941:TEOMAA>2.0.CO;2](https://doi.org/10.1130/0016-7606(1983)94<941:TEOMAA>2.0.CO;2)

Anderson, T. H., Silver, L. T., Nourse, J. A., McKee, J. W., & Steiner, M. B. (2005). The Mojave–Sonora megashear–Field and analytical studies leading to the conception and evolution of the hypothesis. *SPECIAL PAPERS–GEOLOGICAL SOCIETY OF AMERICA*, 393, 1.

Aranda-Gómez, J. J., & McDowell, F. W. (1998). Paleogene Extension in the Southern Basin and Range Province of Mexico: Syndepositional Tilting of Eocene Red Beds and Oligocene Volcanic Rocks in the Guanajuato Mining District. *International Geology Review*, 40(2), 116–134. <https://doi.org/10.1080/00206819809465201>

Bagheri, S. and Gol, S.D., 2020. The eastern iranian orocline. *Earth-Science Reviews*, 210, p.103322. ISSN 0012-8252. <https://doi.org/10.1016/j.earscirev.2020.103322>.

820 Barboza-Gudiño, J. R., Hoppe, M., Gómez-Anguiano, M., & Martínez-Macías, P. (2004).
821 Aportaciones para la interpretación estratigráfica y estructural de la porción noroccidental de la
822 Sierra de Catorce, San Luis Potosí, México. *Revista Mexicana de Ciencias Geológicas*, ISSN
823 1026-8774, Vol. 21, No. 3, 2004, 299-319, 21.

824 Barboza-Gudiño, J. R., Molina-Garza, R. S., & Lawton, T. F. (2012). Sierra de Catorce: Remnants
825 of the ancient western equatorial margin of Pangea in central Mexico. In J. J. Aranda-Gómez, G.
826 Tolson, & R. S. Molina-Garza (Eds.), *The Southern Cordillera and Beyond* (Vol. 25, p. 0).
827 Geological Society of America. [https://doi.org/10.1130/2012.0025\(01\)](https://doi.org/10.1130/2012.0025(01))

828 Barboza-Gudiño, J. R., Ocampo-Díaz, Y. Z. E., Zavala-Monsiváis, A., & López-Doncel, R. A.
829 (2014). Procedencia como herramienta para la subdivisión estratigráfica del Mesozoico temprano
830 en el noreste de México. *Revista Mexicana de Ciencias Geológicas*, 31, 303–324. Scopus.

831 Barboza-Gudiño, J. R., Orozco-Esquivel, M. T., Gómez-Anguiano, M., & Zavala-Monsiváis, A.
832 (2008). The Early Mesozoic volcanic arc of western North America in northeastern Mexico.
833 *Journal of South American Earth Sciences*, 25(1), 49–63.
834 <https://doi.org/10.1016/j.jsames.2007.08.003>

835 Barboza-Gudiño, J. R., Zavala-Monsiváis, A., Castellanos-Rodríguez, V., Jaime-Rodríguez, D., &
836 Almaraz-Martínez, C. (2021). Subduction-related Jurassic volcanism in the Mesa Central province
837 and contemporary Gulf of Mexico opening. *Journal of South American Earth Sciences*, 108,
838 102961. <https://doi.org/10.1016/j.jsames.2020.102961>

839 Barboza-Gudiño, J. R., Zavala-Monsiváis, A., Venegas-Rodríguez, G., & Barajas-Nigoche, L. D.
840 (2010). Late Triassic stratigraphy and facies from northeastern Mexico: Tectonic setting and
841 provenance. *Geosphere*, 6(5), 621–640. Scopus. <https://doi.org/10.1130/GES00545.1>

842 Bartolini, C., Lang, H., & Spell, T. (2003). Geochronology, Geochemistry, and Tectonic Setting
843 of the Mesozoic Nazas Arc in North-Central Mexico, and its Continuation to Northern South
844 America. 427–461.

845 Bartolini, C., Wilson, J. L., & Lawton, T. F. (1999). Mesozoic Sedimentary and Tectonic History
846 of North-central Mexico. Geological Society of America.

847 Busby, C. J. (2023). Guerrero-Alisitos-Vizcaino superterrane of western Mexico and its ties to the
848 Mexican continental margin (Gondwana and SW Laurentia). In S. J. Whitmeyer, M. L. Williams,
849 D. A. Kellett, & B. Tikoff (Eds.), *Laurentia: Turning Points in the Evolution of a Continent* (Vol.
850 220, p. 0). Geological Society of America. [https://doi.org/10.1130/2022.1220\(34\)](https://doi.org/10.1130/2022.1220(34))

851 Busby, C. J., & Centeno-García, E. (2022). The “Nazas Arc” is a continental rift province:
852 Implications for Mesozoic tectonic reconstructions of the southwest Cordillera, U.S. and Mexico.
853 *Geosphere*, 18(2), 647–669. <https://doi.org/10.1130/GES02443.1>

854 Butler, R. (1992). *Paleomagnetism: Magnetic Domains to Geologic Terranes*. Blackwell Science
855 Inc.

856 Campa-Uranga, M. F., García-Díaz, J. L., & Iriondo, A. (2004). El arco sedimentario del Jurásico
857 Medio (Grupo Tecocoyunca y Las Lluvias) de Olinalá. *GEOS Unión Geofísica Mexicana*, 24(2),
858 174.

859 Carey, S. W. (1955). The orocline concept in geotectonics-Part I. *Papers and Proceedings of the*
860 *Royal Society of Tasmania*, 89, 255–288.

861 Centeno-García, E., Anderson, T. H., Nourse, J. A., McKee, J. W., & Steiner, M. B. (2005).
862 Review of upper Paleozoic and lower Mesozoic stratigraphy and depositional environments,
863 central and west Mexico: Constraints on terrane analysis and paleogeography. *SPECIAL*
864 *PAPERS-GEOLOGICAL SOCIETY OF AMERICA*, 393, 233.

865 Centeno-García, E., Guerrero-Suastegui, M., & Talavera-Mendoza, O. (2008). The Guerrero
866 Composite Terrane of western Mexico: Collision and subsequent rifting in a supra-subduction
867 zone. In A. E. Draut, Peter. D. Clift, & D. W. Scholl (Eds.), *Formation and Applications of the*
868 *Sedimentary Record in Arc Collision Zones* (Vol. 436, p. 0). Geological Society of America.
869 [https://doi.org/10.1130/2008.2436\(13\)](https://doi.org/10.1130/2008.2436(13))

870 Chadima, M., & Hrouda, F. (2009). *Cureval 8.0: Thermomagnetic curve browser for windows*.
871 Agico. Inc, Brno.

872 Chávez-Cabello, G., Aranda-Gómez, J. J., Molina-Garza, R. S., Cossío-Torres, T., Arvizu-
873 Gutiérrez, I. R., & González-Naranjo, G. A. (2005). La falla San Marcos: Una estructura jurásica

874 de basamento multi reactivada del noreste de México. Boletín de La Sociedad Geológica Mexicana,
875 57(1), 27–52.

876 Chávez-Cabello, G., Cossío-Torres, T., & Peterson-Rodríguez, R. H. (2004). Change of the
877 maximum principal stress during the Laramide Orogeny in the Monterrey salient, northeast
878 México. *Orogenic Curvature: Integrating Paleomagnetic and Structural Analyses*: Geological
879 Society of America Special Paper, 383, 145–159.

880 Clemons, R. E., & McLeroy, D. F. (1965). Resumen de la geología de la Hoja Torreón, 13R-1 (1):
881 Universidad Nacional Autónoma de México. Instituto de Geología, Carta Geológica de México,
882 Serie, 1(100,000).

883 De Boer, C. B., & Dekkers, M. J. (1998). Thermomagnetic behavior of hematite and goethite as a
884 function of grain size in various non-saturating magnetic fields. *Geophysical Journal International*,
885 133(3), 541–552.

886 DeCelles, P. G., Ducea, M. N., Kapp, P., & Zandt, G. (2009). Cyclicality in Cordilleran orogenic
887 systems. *Nature Geoscience*, 2(4), Article 4. <https://doi.org/10.1038/ngeo469>

888 Deenen, M. H., Langereis, C. G., van Hinsbergen, D. J., & Biggin, A. J. (2011). Geomagnetic
889 secular variation and the statistics of palaeomagnetic directions. *Geophysical Journal International*,
890 186(2), 509–520.

891 Del Pilar-Martínez, A., Nieto-Samaniego, A. F., & Alaniz-Alvarez, S. A. (2020). Development of
892 a brittle triaxial deformation zone in the upper crust: The case of the southern Mesa Central of
893 Mexico. *Tectonics*, 39(11), e2020TC006166.

894 Dickinson, W. R., & Lawton, T. F. (2001). Carboniferous to Cretaceous assembly and
895 fragmentation of Mexico. *Geological Society of America Bulletin*, 113(9), 1142–1160.

896 Dunlop, D. J., & Özdemir, Ö. (1997). *Rock magnetism: Fundamentals and frontiers*. Cambridge
897 University Press.

898 Eguluz, S., Aranda, M., & Marrett, R. (2000). Tectónica de la Sierra Madre Oriental, México.
899 Boletín de La Sociedad Geológica Mexicana, 53(1), 1–26.

900 Eichelberger, N., & McQuarrie, N. (2015). Kinematic reconstruction of the Bolivian orocline.
901 *Geosphere*, 11(2), 445–462. <https://doi.org/10.1130/GES01064.1>

902 Eldredge, S., Bachtadse, V., & Van der Voo, R. (1985). Paleomagnetism and the orocline
903 hypothesis. *Tectonophysics*, 119(1–4), 153–179.

904 Fastovsky, D. E., Hermes, O. D., Strater, N. H., Bowring, S. A., Clark, J. M., Montellano, M., &
905 Rene, H. R. (2005). Pre–Late Jurassic, fossil-bearing volcanic and sedimentary red beds of
906 Huizachal Canyon, Tamaulipas, Mexico.

907 Fisher, R. A. (1953). Dispersion on a sphere. *Proceedings of the Royal Society of London. Series*
908 *A. Mathematical and Physical Sciences*, 217(1130), 295–305.

909 Fitz-Díaz, E., Lawton, T. F., Juárez-Arriaga, E., & Chávez-Cabello, G. (2018). The Cretaceous-
910 Paleogene Mexican orogen: Structure, basin development, magmatism and tectonics. *Earth-*
911 *Science Reviews*, 183, 56–84.

912 Flinn, D. (1962). On folding during three-dimensional progressive deformation. *Quarterly Journal*
913 *of the Geological Society*, 118(1–4), 385–428.

914 García-Obregón, R. (2008). Cartografía geológica y petrología del vulcanismo mesozoico en el
915 Valle de Huizachal, Tamaulipas. [Tesis de Licenciatura]. Universidad Autónoma de Nuevo León.

916 Gerritsen, D., Vaes, B., & van Hinsbergen, D. J. (2022). Influence of data filters on the position
917 and precision of paleomagnetic poles: What is the optimal sampling strategy? *Geochemistry,*
918 *Geophysics, Geosystems*, 23(4), e2021GC010269.

919 Godínez-Urban, A., Lawton, T. F., Molina Garza, R. S., Iriondo, A., Weber, B., & López-Martínez,
920 M. (2011). Jurassic volcanic and sedimentary rocks of the La Silla and Todos Santos Formations,
921 Chiapas: Record of Nazas arc magmatism and rift-basin formation prior to opening of the Gulf of
922 Mexico. *Geosphere*, 7(1), 121–144.

923 Goldhammer, R. K. (1999). Mesozoic sequence stratigraphy and paleogeographic evolution of
924 northeast Mexico.

925 Gómez Torres, R. C. (2022). Geoquímica en roca total y zircones de rocas Mágmaticas del
926 Jurásico-Paleógeno en el Bloque de San Julián, Zacatecas, México. [Masters Tesis]. Universidad
927 Autónoma de Nuevo León. p. 139.

928 González-León, C. M., Vázquez-Salazar, M., Navarro, T. S., Solari, L. A., Nourse, J. A., Del Rio-
929 Salas, R., Lozano-Santacruz, R., Arvizu, O. P., & Valenzuela Chacón, J. C. (2021). Geology and
930 geochronology of the Jurassic magmatic arc in the Magdalena quadrangle, north-central Sonora,
931 Mexico. *Journal of South American Earth Sciences*, 108, 103055.
932 <https://doi.org/10.1016/j.jsames.2020.103055>

933 Grajales-Nishimura, J. M., Terrell, D. J., & Damon, P. E. (1992). Evidencias de la prolongación
934 del arco magmático cordillerano del Triásico Tardío-Jurásico en Chihuahua. Durango y Coahuila:
935 *Boletín de La Asociación Mexicana de Geólogos Petroleros*, 42(2), 1–18.

936 Gray, G. G., & Lawton, T. F. (2011). New constraints on timing of Hidalgoan (Laramide)
937 deformation in the Parras and La Popa basins, NE Mexico. *Boletín de La Sociedad Geológica*
938 *Mexicana*, 63(2), 333–343.

939 Gubbins, D., & Herrero-Bervera, E. (2007). *Encyclopedia of Geomagnetism and Paleomagnetism*.
940 Springer Science & Business Media.

941 Guerra Roel, R. (2019). Análisis estructural de la zona norte del bloque de San Julián, Zacatecas
942 México [Masters, Universidad Autónoma de Nuevo León]. <http://eprints.uanl.mx/18367/>

943 Gutiérrez-Alonso, G., Fernández-Suárez, J., & Weil, A. B. (2004). Orocline triggered lithospheric
944 delamination. In *Special Paper 383: Orogenic curvature: Integrating paleomagnetic and structural*
945 *analyses (Vol. 383, pp. 121–130)*. Geological Society of America. [https://doi.org/10.1130/0-8137-](https://doi.org/10.1130/0-8137-2383-3(2004)383[121:OTLD]2.0.CO;2)
946 [2383-3\(2004\)383\[121:OTLD\]2.0.CO;2](https://doi.org/10.1130/0-8137-2383-3(2004)383[121:OTLD]2.0.CO;2)

947 Gutiérrez-Alonso, G., Fernández-Suárez, J., Weil, A. B., Brendan Murphy, J., Damian Nance, R.,
948 Corfú, F., & Johnston, S. T. (2008). Self-subduction of the Pangaeon global plate. *Nature*
949 *Geoscience*, 1(8), Article 8. <https://doi.org/10.1038/ngeo250>

950 Gutiérrez-Navarro, R., Fitz Diaz, E., Barboza-Gudiño, J., & Stockli, D. (2021). Shortening and
951 exhumation of Sierra de Catorce in northeastern Mexico, in light of ⁴⁰Ar/³⁹Ar illite dating and

952 U–Th/He zircon thermochronology. *Journal of South American Earth Sciences*, 111, 103334.
953 <https://doi.org/10.1016/j.jsames.2021.103334>

954 Henry, C. D., & Aranda-Gómez, J. J. (1992). The real southern Basin and Range: Mid- to Late
955 Cenozoic extension in Mexico. *Geology*, 20(8), 701–704. [https://doi.org/10.1130/0091-](https://doi.org/10.1130/0091-7613(1992)020<0701:TRSBAR>2.3.CO;2)
956 [7613\(1992\)020<0701:TRSBAR>2.3.CO;2](https://doi.org/10.1130/0091-7613(1992)020<0701:TRSBAR>2.3.CO;2)

957 Hernández-Romano, U., Aguilera-Franco, N., Martínez-Medrano, M., & Barceló-Duarte, J. (1997).
958 Guerrero-Morelos Platform drowning at the Cenomanian–Turonian boundary, Huitziltepec area,
959 Guerrero State, southern Mexico. *Cretaceous Research*, 18(5), 661–686.

960 Hindle, D., & Burkhard, M. (1999). Strain, displacement and rotation associated with the
961 formation of curvature in fold belts; the example of the Jura arc. *Journal of Structural Geology*,
962 21(8), 1089–1101. [https://doi.org/10.1016/S0191-8141\(99\)00021-8](https://doi.org/10.1016/S0191-8141(99)00021-8)

963 Imlay, R. W., Cepeda, E., Alvarez, M., & Diaz, T. (1948). Stratigraphic relations of certain Jurassic
964 formations in eastern Mexico. *AAPG Bulletin*, 32(9), 1750–1761.

965 INEGI. (2023). Biblioteca digital de Mapas. Instituto Nacional de Estadística y Geografía. INEGI.
966 <https://www.inegi.org.mx/app/mapas/>

967 Jelinek, V. (1981). Characterization of the magnetic fabric of rocks. *Tectonophysics*, 79(3–4),
968 T63–T67.

969 Jiménez, G., Speranza, F., Faccenna, C., Bayona, G., & Mora, A. (2014). Paleomagnetism and
970 magnetic fabric of the Eastern Cordillera of Colombia: Evidence for oblique convergence and
971 nonrotational reactivation of a Mesozoic intracontinental rift. *Tectonics*, 33(11), 2233–2260.
972 <https://doi.org/10.1002/2014TC003532>

973 Johnston, S. T. (2001). The Great Alaskan Terrane Wreck: Reconciliation of paleomagnetic and
974 geological data in the northern Cordillera. *Earth and Planetary Science Letters*, 193(3), 259–272.
975 [https://doi.org/10.1016/S0012-821X\(01\)00516-7](https://doi.org/10.1016/S0012-821X(01)00516-7)

976 Johnston, S. T., Weil, A. B., & Gutiérrez-Alonso, G. (2013). Oroclines: Thick and thin. *GSA*
977 *Bulletin*, 125(5–6), 643–663. <https://doi.org/10.1130/B30765.1>

978 Jones, N. W., McKee, J. W., Anderson, T. H., & Silver, L. T. (1995). Jurassic volcanic rocks in
979 northeastern Mexico: A possible remnant of a Cordilleran magmatic arc. In C. Jacques-Ayala, C.
980 M. González-Léon, & J. Roldán-Quintana (Eds.), *Studies on the Mesozoic of Sonora and adjacent*
981 *areas* (Vol. 301, p. 0). Geological Society of America. <https://doi.org/10.1130/0-8137-2301-9.179>

982 Kirschvink, J. L. (1980). The least-squares line and plane and the analysis of palaeomagnetic data.
983 *Geophysical Journal International*, 62(3), 699–718.

984 Kollmeier, J. M., van der Pluijm, B. A., & Van der Voo, R. (2000). Analysis of Variscan dynamics;
985 early bending of the Cantabria–Asturias Arc, northern Spain. *Earth and Planetary Science Letters*,
986 181(1), 203–216. [https://doi.org/10.1016/S0012-821X\(00\)00203-X](https://doi.org/10.1016/S0012-821X(00)00203-X)

987 Koymans, M. R., Langereis, C. G., Pastor-Galán, D., & van Hinsbergen, D. J. (2016).
988 Paleomagnetism. org: An online multi-platform open-source environment for paleomagnetic data
989 analysis. Elsevier.

990 Koymans, M. R., van Hinsbergen, D. J. J., Pastor-Galán, D., Vaes, B., & Langereis, C. G. (2020).
991 Towards FAIR paleomagnetic data management through Paleomagnetism. Org 2.0. *Geochemistry,*
992 *Geophysics, Geosystems*, 21(2), e2019GC008838.

993 Kruiver, P. P., Dekkers, M. J., & Heslop, D. (2001). Quantification of magnetic coercivity
994 components by the analysis of acquisition curves of isothermal remanent magnetisation. *Earth and*
995 *Planetary Science Letters*, 189(3–4), 269–276.

996 Lawton, T. F., & Molina Garza, R. S. (2014). U-Pb geochronology of the type Nazas Formation
997 and superjacent strata, northeastern Durango, Mexico: Implications of a Jurassic age for
998 continental-arc magmatism in north-central Mexico. *GSA Bulletin*, 126(9–10), 1181–1199.
999 <https://doi.org/10.1130/B30827.1>

1000 Li, P., Rosenbaum, G., & Donchak, P. J. (2012). Structural evolution of the Texas Orocline, eastern
1001 Australia. *Gondwana Research*, 22(1), 279–289.

1002 López-Infanzón, M. L. (1986). Estudio Petrogenético De Las Rocas Igneas En Las Formaciones
1003 Huizachal Y Nazas. *Boletín de La Sociedad Geológica Mexicana*, 47(2), 1–41.

1004 Maffione, M., Speranza, F., Faccenna, C., & Rossello, E. (2010). Paleomagnetic evidence for a
1005 pre-early Eocene (~50Ma) bending of the Patagonian orocline (Tierra del Fuego, Argentina):
1006 Paleogeographic and tectonic implications. *Earth and Planetary Science Letters*, 289(1), 273–286.
1007 <https://doi.org/10.1016/j.epsl.2009.11.015>

1008 Marshak, S. (1988). Kinematics of orocline and arc formation in thin-skinned orogens. *Tectonics*,
1009 7(1), 73–86. <https://doi.org/10.1029/TC007i001p00073>

1010 Marshak, S. (2004). Salients, Recesses, Arcs, Oroclines, and Syntaxes—A Review of Ideas
1011 Concerning the Formation of Map-view Curves in Fold-thrust Belts. In K. R. McClay (Ed.), *Thrust*
1012 *Tectonics and Hydrocarbon Systems* (Vol. 82, p. 0). American Association of Petroleum
1013 Geologists. <https://doi.org/10.1306/M82813C9>

1014 Martini, M., & Ortega-Gutiérrez, F. (2018). Tectono-stratigraphic evolution of eastern Mexico
1015 during the break-up of Pangea: A review. *Earth-Science Reviews*, 183, 38–55.
1016 <https://doi.org/10.1016/j.earscirev.2016.06.013>

1017 Martini, M., Solari, L., & Camprubí, A. (2013). Kinematics of the Guerrero terrane accretion in
1018 the Sierra de Guanajuato, central Mexico: New insights for the structural evolution of arc–
1019 continent collisional zones. *International Geology Review*, 55(5), 574–589.
1020 <https://doi.org/10.1080/00206814.2012.729361>

1021 Martini, M., Solé, J., Garduño-Martínez, D. E., Puig, T. P., & Omaña, L. (2016). Evidence for two
1022 Cretaceous superposed orogenic belts in central Mexico based on paleontologic and K-Ar
1023 geochronologic data from the Sierra de los Cuarcos. *Geosphere*, 12(4), 1257–1270.
1024 <https://doi.org/10.1130/GES01275.1>

1025 Mauel, D. J., Lawton, T. F., González-León, C., Iriondo, A., & Amato, J. M. (2011). Stratigraphy
1026 and age of Upper Jurassic strata in north-central Sonora, Mexico: Southwestern Laurentian record
1027 of crustal extension and tectonic transition. *Geosphere*, 7(2), 390–414.
1028 <https://doi.org/10.1130/GES00600.1>

1029 Maxbauer, D. P., Feinberg, J. M., & Fox, D. L. (2016). MAX UnMix: A web application for
1030 unmixing magnetic coercivity distributions. *Computers & Geosciences*, 95, 140–145.
1031 <https://doi.org/10.1016/j.cageo.2016.07.009>

1032 McElhinny, M. W., & McFadden, P. L. (1999). *Paleomagnetism: Continents and Oceans*. Elsevier.

1033 McFadden, P. L., & McElhinny, M. W. (1988). The combined analysis of remagnetization circles
 1034 and direct observations in palaeomagnetism. *Earth and Planetary Science Letters*, 87(1), 161–172.
 1035 [https://doi.org/10.1016/0012-821X\(88\)90072-6](https://doi.org/10.1016/0012-821X(88)90072-6)

1036 Meert, J. G., Pivarunas, A. F., Evans, D. A. D., Pisarevsky, S. A., Pesonen, L. J., Li, Z.-X., Elming,
 1037 S.-Å., Miller, S. R., Zhang, S., & Salminen, J. M. (2020). The magnificent seven: A proposal for
 1038 modest revision of the Van der Voo (1990) quality index. *Tectonophysics*, 790, 228549.
 1039 <https://doi.org/10.1016/j.tecto.2020.228549>

1040 Mixon, R. B., Murray, G. E., & Teodoro, D. G. (1959). Age and Correlation of Huizachal Group
 1041 (Mesozoic), State of Tamaulipas, Mexico1: ADDENDUM. *AAPG Bulletin*, 43(4), 757–771.
 1042 <https://doi.org/10.1306/0BDA5ED3-16BD-11D7-8645000102C1865D>

1043 Molina-Garza, R. S., & Iriondo, A. (2005). La Megacizalla Mojave-Sonora: La hipótesis, la
 1044 controversia y el estado actual de conocimiento. *Boletín de la Sociedad Geológica Mexicana*, 57(1),
 1045 1–26. <https://doi.org/10.18268/bsgm2005v57n1a1>

1046 Molina-Garza, R. S., Pindell, J., & Montaña Cortés, P. C. (2020). Slab flattening and tractional
 1047 coupling drove Neogene clockwise rotation of Chiapas Massif, Mexico: Paleomagnetism of the
 1048 Eocene El Bosque Formation. *Journal of South American Earth Sciences*, 104, 102932.
 1049 <https://doi.org/10.1016/j.jsames.2020.102932>

1050 Montes, C., Bayona, G., Cardona, A., Buchs, D. M., Silva, C. A., Morón, S., Hoyos, N., Ramírez,
 1051 D. A., Jaramillo, C. A., & Valencia, V. (2012). Arc-continent collision and orocline formation:
 1052 Closing of the Central American seaway. *Journal of Geophysical Research: Solid Earth*, 117(B4).
 1053 <https://doi.org/10.1029/2011JB008959>

1054 Nemkin, S. R., Chávez-Cabello, G., Fitz-Díaz, E., van der Pluijm, B., & Van der Voo, R. (2019).
 1055 Concurrence of folding and remagnetization events in the Monterrey Salient (NE Mexico).
 1056 *Tectonophysics*, 760, 58–68. <https://doi.org/10.1016/j.tecto.2017.12.002>

1057 Nieto-Samaniego, Á. F., Ferrari, L., Alaniz-Alvarez, S. A., Labarthe-Hernández, G., & Rosas-
 1058 Elguera, J. (1999). Variation of Cenozoic extension and volcanism across the southern Sierra

1059 Madre Occidental volcanic province, Mexico. *Geological Society of America Bulletin*, 111(3),
1060 347–363.

1061 Ocampo-Díaz, Y. Z. E., Pinzon-Sotelo, M. P., Chávez-Cabello, G., Ramírez-Díaz, A., Martínez-
1062 Paco, M., Velasco-Tapia, F., Guerrero-Suastegui, M., Barboza-Gudiño, J. R., Ocampo-Díaz, Y. Z.
1063 E., Pinzon-Sotelo, M. P., Chávez-Cabello, G., Ramírez-Díaz, A., Martínez-Paco, M., Velasco-
1064 Tapia, F., Guerrero-Suastegui, M., & Barboza-Gudiño, J. R. (2016). Propuesta nomenclatural y
1065 análisis de procedencia de la Formación Concepción del Oro (antes Formación Caracol):
1066 Implicaciones sobre la evolución tectónica del sur de Norteamérica durante el Cretácico Tardío.
1067 *Revista mexicana de ciencias geológicas*, 33(1), 3–33.

1068 Ogg, J. G. (2020). Chapter 5—Geomagnetic Polarity Time Scale. In F. M. Gradstein, J. G. Ogg,
1069 M. D. Schmitz, & G. M. Ogg (Eds.), *Geologic Time Scale 2020* (pp. 159–192). Elsevier.
1070 <https://doi.org/10.1016/B978-0-12-824360-2.00005-X>

1071 O'Reilly, W. (1984). Applications of rock and mineral magnetism. In W. O'Reilly (Ed.), *Rock and*
1072 *Mineral Magnetism* (pp. 194–212). Springer US. https://doi.org/10.1007/978-1-4684-8468-7_9

1073 Ortega-Flores, B., Solari, L. A., Martini, M., & Ortega-Obregón, C. (2020). The Guerrero terrane,
1074 a para-autochthonous block on the paleo-Pacific continental margin of North America: Evidence
1075 from zircon U-Pb dating and Hf isotopes. [https://doi.org/10.1130/2020.2546\(08\)](https://doi.org/10.1130/2020.2546(08))

1076 Padilla y Sánchez, R. J. (1985). Las estructuras de la Curvatura de Monterrey, estados de Coahuila,
1077 Nuevo León, Zacatecas y San Luis Potosí. *Revista Mexicana de Ciencias Geológicas*, 6(1), 1–20.

1078 Pantoja-Alor, J. (1972). Datos geológicos y estratigráficos de la Formación Nazas (memoria), II
1079 Convención Nacional. Mazatlán, Sinaloa, Sociedad Geológica Mexicana, 25–31.

1080 Parés, J. M. (2015). Sixty years of anisotropy of magnetic susceptibility in deformed sedimentary
1081 rocks. *Frontiers in Earth Science*, 3. <https://www.frontiersin.org/articles/10.3389/feart.2015.00004>

1082 Parolari, M., Martini, M., Gómez-Tuena, A., Ortega-Gutiérrez, F., Errázuriz-Henao, C., &
1083 Cavazos-Tovar, J. G. (2022). The petrogenesis of Early–Middle Jurassic magmatism in southern
1084 and central Mexico and its role during the break-up of Western Pangaea. *Geological Magazine*,
1085 159(6), 873–892. <https://doi.org/10.1017/S0016756822000061>

1086 Pastor-Galán, D. (2022). From supercontinent to superplate: Late Paleozoic Pangea's inner
1087 deformation suggests it was a short-lived superplate. *Earth-Science Reviews*, 226, 103918.
1088 <https://doi.org/10.1016/j.earscirev.2022.103918>

1089 Pastor-Galán, D., Groenewegen, T., Brouwer, D., Krijgsman, W., & Dekkers, M. J. (2015). One
1090 or two oroclinal in the Variscan orogen of Iberia? Implications for Pangea amalgamation. *Geology*,
1091 43(6), 527–530. <https://doi.org/10.1130/G36701.1>

1092 Pastor-Galán, D., Gutiérrez-Alonso, G., Dekkers, M. J., & Langereis, C. G. (2017).
1093 Paleomagnetism in Extremadura (Central Iberian zone, Spain) Paleozoic rocks: Extensive
1094 remagnetizations and further constraints on the extent of the Cantabrian orocline. *Journal of*
1095 *Iberian Geology*, 43(4), 583–600. <https://doi.org/10.1007/s41513-017-0039-x>

1096 Pastor-Galán, D., Gutiérrez-Alonso, G., & Weil, A. B. (2011). Orocline timing through joint
1097 analysis: Insights from the Ibero-Armorican Arc. *Tectonophysics*, 507(1), 31–46.
1098 <https://doi.org/10.1016/j.tecto.2011.05.005>

1099 Pastor-Galán, D., Gutiérrez-Alonso, G., & Weil, A. B. (2020). The enigmatic curvature of Central
1100 Iberia and its puzzling kinematics. *Solid Earth*, 11(4), 1247–1273. [https://doi.org/10.5194/se-11-](https://doi.org/10.5194/se-11-1247-2020)
1101 1247-2020

1102 Pastor-Galán, D., Gutiérrez-Alonso, G., Zulauf, G., & Zanella, F. (2012). Analogue modeling of
1103 lithospheric-scale orocline buckling: Constraints on the evolution of the Iberian-Armorican Arc.
1104 *GSA Bulletin*, 124(7–8), 1293–1309. <https://doi.org/10.1130/B30640.1>

1105 Pastor-Galán, D., Martín-Merino, G., & Corrochano, D. (2014). Timing and structural evolution
1106 in the limb of an orocline: The Pisuerga–Carrión Unit (southern limb of the Cantabrian Orocline,
1107 NW Spain). *Tectonophysics*, 622, 110–121. <https://doi.org/10.1016/j.tecto.2014.03.004>

1108 Pastor-Galán, D., Pueyo, E. L., Diederer, M., García-Lasanta, C., & Langereis, C. G. (2018). Late
1109 Paleozoic Iberian Orocline(s) and the Missing Shortening in the Core of Pangea. *Paleomagnetism*
1110 *From the Iberian Range*. *Tectonics*, 37(10), 3877–3892. <https://doi.org/10.1029/2018TC004978>

1111 Pastor-Galán, D., Spencer, C. J., Furukawa, T., & Tsujimori, T. (2021). Evidence for crustal
1112 removal, tectonic erosion and flare-ups from the Japanese evolving forearc sediment provenance.
1113 *Earth and Planetary Science Letters*, 564, 116893. <https://doi.org/10.1016/j.epsl.2021.116893>

1114 Patiño-Mendez, G. (2022). Analisis de la Fabrica Magnética en lavas plegadas de la Formación
 1115 Nazas, Bloque de San Julian, Zacatecas, México. [Batchelor tesis]. Universidad Autónoma de
 1116 Nuevo León.

1117 Pindell, J., & Kennan, L. (2001). Kinematic Evolution of the Gulf of Mexico and Caribbean. In R.
 1118 H. Fillon, N. C. Rosen, P. Weimer, A. Lowrie, H. Pettingill, R. L. Phair, H. H. Roberts, & H. H.
 1119 van Hoom (Eds.), *Petroleum Systems of Deep-Water Basins—Global and Gulf of Mexico*
 1120 *Experience* (Vol. 21, p. 0). SEPM Society for Sedimentary Geology.
 1121 <https://doi.org/10.5724/gcs.01.21.0193>

1122 Ramírez-Peña, C. F. (2017). Análisis de la deformación progresiva en la zona sur del sector
 1123 transversal de Parras y la Saliente de Monterrey, México. PhD. Tesis, Universidad Autónoma de
 1124 Nuevo León, Facultad de Ciencias de la Tierra.

1125 Ramírez-Peña, C. F., & Chávez-Cabello, G. (2017). Age and evolution of thin-skinned
 1126 deformation in Zacatecas, Mexico: Sevier orogeny evidence in the Mexican Fold-Thrust Belt.
 1127 *Journal of South American Earth Sciences*, 76, 101–114.
 1128 <https://doi.org/10.1016/j.jsames.2017.01.007>

1129 Ramírez-Peña, C. F., Chávez-Cabello, G., Fitz-Díaz, E., Aranda-Gómez, J. J., & Valdés, R. S.
 1130 (2019). Uplift and syn-orogenic magmatism in the Concepción del Oro Block: A thick-skinned
 1131 (Laramide style?) contractional structure in the Mexican Fold-Thrust Belt. *Journal of South*
 1132 *American Earth Sciences*, 93, 242–252. <https://doi.org/10.1016/j.jsames.2019.04.012>

1133 Rezaeian, M., Kuijper, C. B., van der Boon, A., Pastor-Galán, D., Cotton, L. J., Langereis, C. G.,
 1134 & Krijgsman, W. (2020). Post-Eocene coupled oroclinal in the Talesh (NW Iran): Paleomagnetic
 1135 constraints. *Tectonophysics*, 786, 228459. <https://doi.org/10.1016/j.tecto.2020.228459>

1136 Rogers, C. L., De Cserna, Z., & VLOTEN, V. (1963). Plutonic rocks of northern Zacatecas and
 1137 adjacent areas, Mexico. US Geological Survey Professional Paper, C7–C10.

1138 Rubio Cisneros, I. I. (2012). Análisis de procedencia de las formaciones el Alamar, La Boca y La
 1139 Joya Noreste de México (triásico superior-jurásico medio) [Phd, Universidad Autónoma de Nuevo
 1140 León]. <http://eprints.uanl.mx/3223/>

1141 Rubio Cisneros, I. I., Ramírez Fernández, J. A., & García Obregón, R. (2011). Análisis preliminar
1142 de procedencia de rocas clásticas jurásicas del valle de Huizachal, Sierra Madre Oriental:
1143 Influencia del vulcanismo sinsedimentario y el basamento cristalino. *Boletín de La Sociedad*
1144 *Geológica Mexicana*, 63(2), 137–156.

1145 Rubio-Cisneros, I. I., & Lawton, T. F. (2011). Detrital zircon U-Pb ages of sandstones in
1146 continental red beds at Valle de Huizachal, Tamaulipas, NE Mexico: Record of Early-Middle
1147 Jurassic arc volcanism and transition to crustal extension. *Geosphere*, 7(1), 159–170.
1148 <https://doi.org/10.1130/GES00567.1>

1149 Salvador, A. (1987). Late Triassic-Jurassic Paleogeography and Origin of Gulf of Mexico Basin1.
1150 *AAPG Bulletin*, 71(4), 419–451. [https://doi.org/10.1306/94886EC5-1704-11D7-](https://doi.org/10.1306/94886EC5-1704-11D7-8645000102C1865D)
1151 [8645000102C1865D](https://doi.org/10.1306/94886EC5-1704-11D7-8645000102C1865D)

1152 SGM. (2023). Cartas impresas disponibles del Servicio Geológico Mexicano.
1153 <https://www.sgm.gob.mx/CartasDisponibles/>

1154 Shaanan, U., Rosenbaum, G., Li, P., & Vasconcelos, P. (2014). Structural evolution of the Early
1155 Permian Nambucca Block (New England Orogen, eastern Australia) and implications for oroclinal
1156 bending. *Tectonics*, 33(7), 1425–1443. <https://doi.org/10.1002/2013TC003426>

1157 Shaw, J., Johnston, S. T., Gutiérrez-Alonso, G., & Weil, A. B. (2012). Oroclines of the Variscan
1158 orogen of Iberia: Paleocurrent analysis and paleogeographic implications. *Earth and Planetary*
1159 *Science Letters*, 329–330, 60–70. <https://doi.org/10.1016/j.epsl.2012.02.014>

1160 Silva-Romo, G., Arellano-Gil, J., Mendoza-Rosales, C., & Nieto-Obregón, J. (2000). A submarine
1161 fan in the Mesa Central, Mexico. *Journal of South American Earth Sciences*, 13(4–5), 429–442.

1162 Silver, L. T., & Anderson, T. H. (1974). Possible left-lateralearly to middle Mesozoic disruption
1163 of the south-western North American craton margin, *Geological Society of America Abstracts and*
1164 *Programs*, 6, 955–956.

1165 Stern, R. J., & Dickinson, W. R. (2010). The Gulf of Mexico is a Jurassic backarc basin. *Geosphere*,
1166 6(6), 739–754. <https://doi.org/10.1130/GES00585.1>

1167 Sussman, A. J., & Weil, A. B. (2004). *Orogenic Curvature: Integrating Paleomagnetic and*
1168 *Structural Analyses*. Geological Society of America.

1169 Tarling, D., & Hrouda, F. (1993). *Magnetic Anisotropy of Rocks*. Springer Science & Business
1170 Media.

1171 Tauxe, L. (2010). *Essentials of Paleomagnetism*. Univ of California Press.

1172 Tauxe, L., & Watson, G. S. (1994). The fold test: An eigen analysis approach. *Earth and Planetary*
1173 *Science Letters*, 122(3), 331–341. [https://doi.org/10.1016/0012-821X\(94\)90006-X](https://doi.org/10.1016/0012-821X(94)90006-X)

1174 Torsvik, T. H., Van der Voo, R., Preeden, U., Mac Niocaill, C., Steinberger, B., Doubrovine, P.
1175 V., Van Hinsbergen, D. J., Domeier, M., Gaina, C., & Tohver, E. (2012). Phanerozoic polar wander,
1176 palaeogeography and dynamics. *Earth-Science Reviews*, 114(3–4), 325–368.

1177 Venegas Rodríguez, G., Barboza-Gudiño, J., & López-Doncel, R. (2009). Geochronology of
1178 detritic zircons in Lower Jurassic beds of the Sierra de Catorce and El Alamito areas, San Luis
1179 Potosí State. *Revista Mexicana de Ciencias Geológicas*, 26, 466–481.

1180 Weil, A. B., Gutiérrez-Alonso, G., & Wicks, D. (2013). Investigating the kinematics of local thrust
1181 sheet rotation in the limb of an orocline: A paleomagnetic and structural analysis of the Esla
1182 tectonic unit, Cantabrian–Asturian Arc, NW Iberia. *International Journal of Earth Sciences*, 102(1),
1183 43–60. <https://doi.org/10.1007/s00531-012-0790-3>

1184 Weil, A. B., Van der Voo, R., & van der Pluijm, B. A. (2001). Oroclinal bending and evidence
1185 against the Pangea megashear: The Cantabria-Asturias arc (northern Spain). *Geology*, 29(11),
1186 991–994. [https://doi.org/10.1130/0091-7613\(2001\)029<0991:OBAEAT>2.0.CO;2](https://doi.org/10.1130/0091-7613(2001)029<0991:OBAEAT>2.0.CO;2)

1187 Weil, A. B., & Yonkee, A. (2009). Anisotropy of magnetic susceptibility in weakly deformed red
1188 beds from the Wyoming salient, Sevier thrust belt: Relations to layer-parallel shortening and
1189 orogenic curvature. *Lithosphere*, 1(4), 235–256. <https://doi.org/10.1130/L42.1>

1190 Weil, A. B., Yonkee, A., & Sussman, A. (2010). Reconstructing the kinematic evolution of curved
1191 mountain belts: A paleomagnetic study of Triassic red beds from the Wyoming salient, Sevier
1192 thrust belt, U.S.A. *GSA Bulletin*, 122(1–2), 3–23. <https://doi.org/10.1130/B26483.1>

1193 Yonkee, A., & Weil, A. B. (2010). Reconstructing the kinematic evolution of curved mountain
1194 belts: Internal strain patterns in the Wyoming salient, Sevier thrust belt, U.S.A. *GSA Bulletin*,
1195 122(1–2), 24–49. <https://doi.org/10.1130/B26484.1>

1196 Yonkee, W. A., & Weil, A. B. (2015). Tectonic evolution of the Sevier and Laramide belts within
1197 the North American Cordillera orogenic system. *Earth-Science Reviews*, 150, 531–593.

1198 Zachary, D. W. (2012). Stratigraphic Controls on the Structural Evolution of the Sierra Madre
1199 Oriental Fold-thrust Belt, Eastern Mexico [Msc Thesis]. University of Houston.

1200 Zavala-Monsiváis, A., Barboza-Gudiño, J. R., Velasco-Tapia, F., & García-Arreola, M. E. (2012).
1201 Sucesión volcánica Jurásica en el área de Charcas, San Luis Potosí: Contribución al entendimiento
1202 del Arco Nazas en el noreste de México. *Boletín de La Sociedad Geológica Mexicana*, 64(3), 277–
1203 293.

1204 Zhou, Y., Murphy, M. A., & Hamade, A. (2006). Structural development of the Peregrina–
1205 Huizachal anticlinorium, Mexico. *Journal of Structural Geology*, 28(3), 494–507.

1206 Zijderveld, J. D. A. (1967). AC demagnetization of rocks: Analysis of results, *Methods in*
1207 *Paleomagnetism* DW Collinson, KM Creer, SK Runcorn, 254–286. Elsevier, New York.

1208

1209

1210

Figure 1 Map of Mexico.

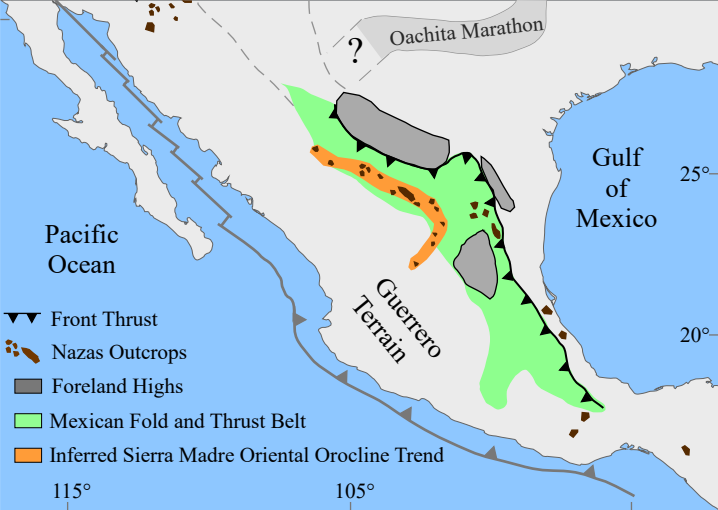


Figure 2 Geological and Trend Map.

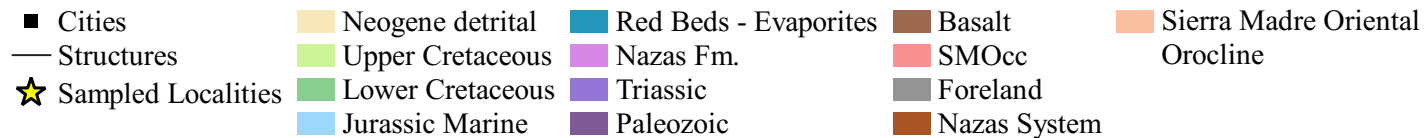
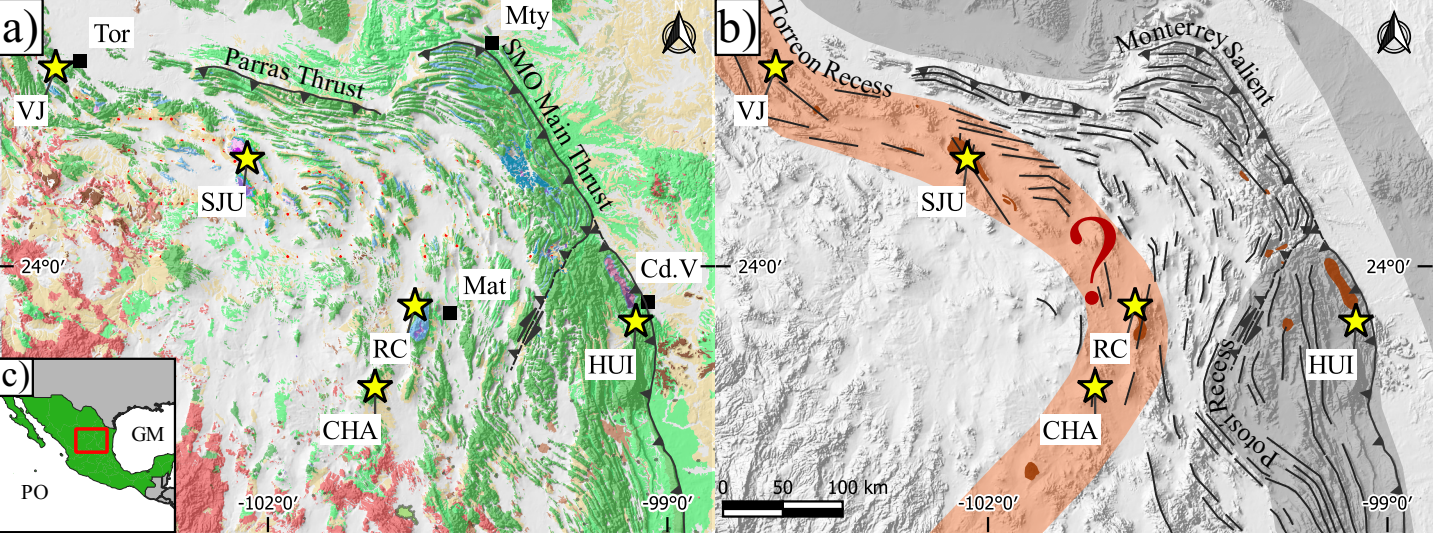


Figure 3 Magnetic Properties.

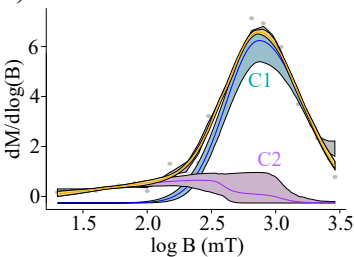
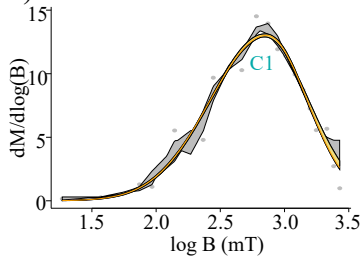
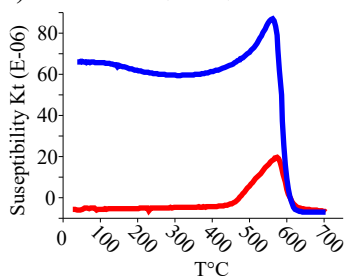
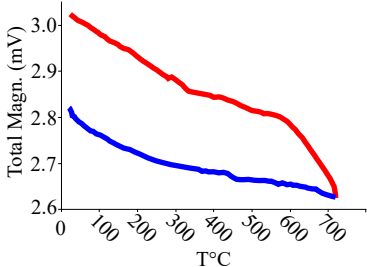
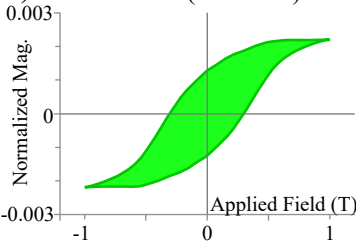
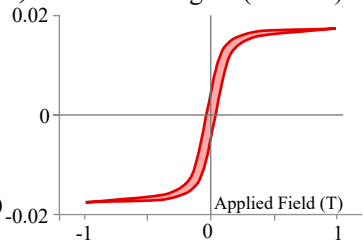
a) Villa Juárez (NA04)**b) Villa Juárez (NA02)****c) Villa Juárez (NA01)****d) Caopas (MIR3)****e) Nazas North (NRN 1.2)****f) Mina San Miguel (MSM 7)**

Figure 4 AMS.

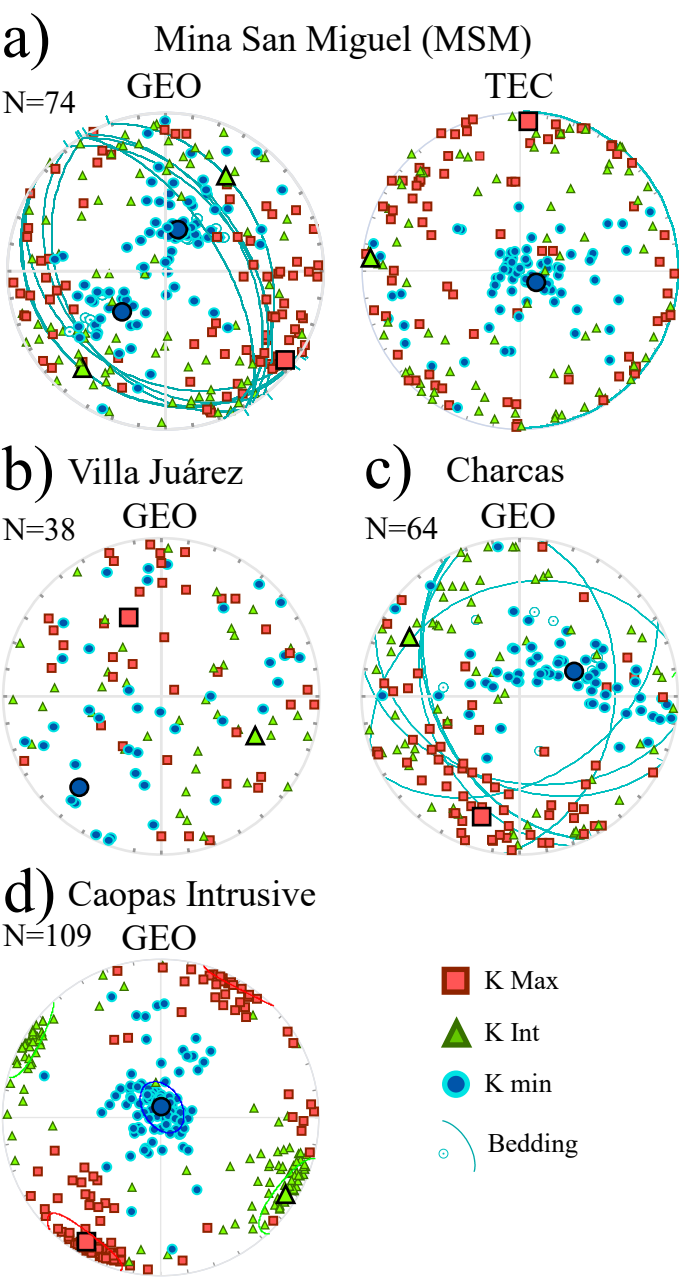
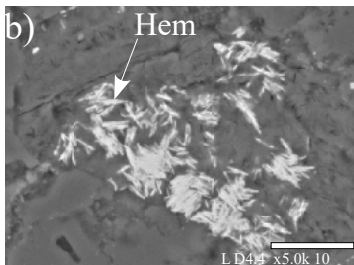
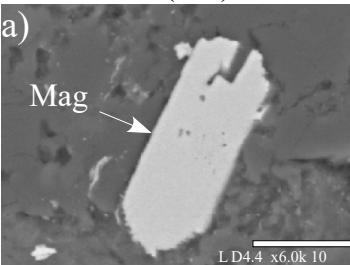


Figure 5 SEM Images.

Villa Juárez (NA)



Mina San Miguel (MSM)

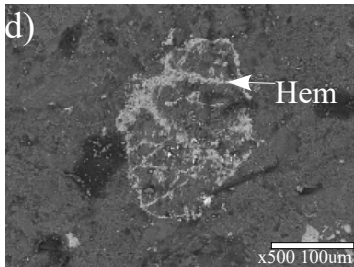
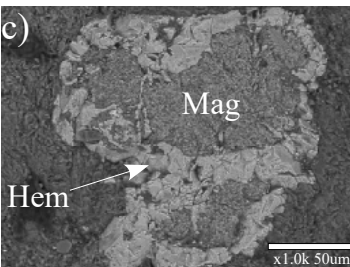
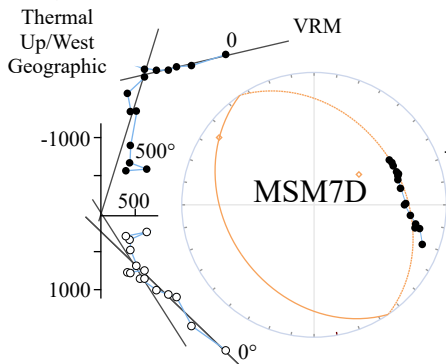
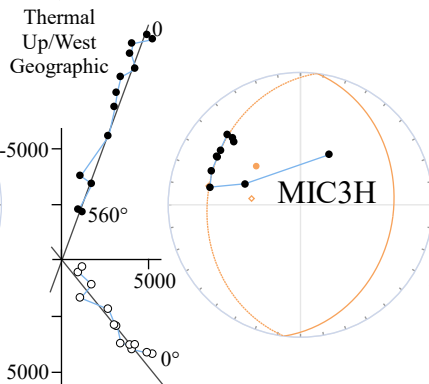


Figure 6 Zijderveld diagrams.

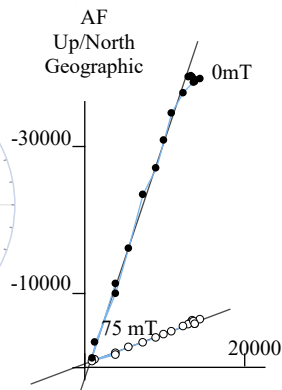
a) MSM 12B



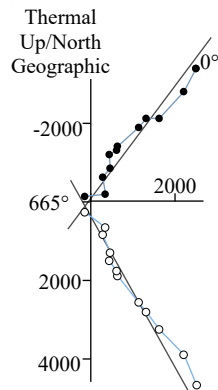
b) MIR 2E



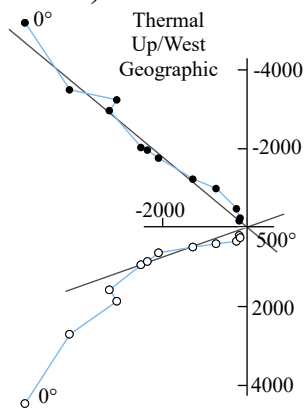
c) CHA 10B



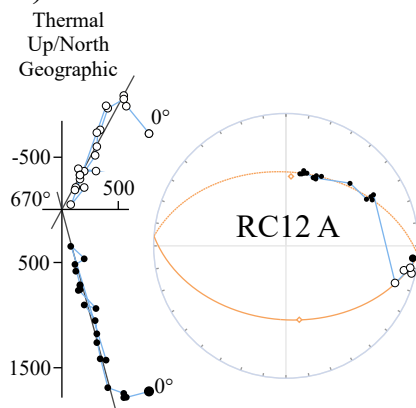
d) NA07-9A



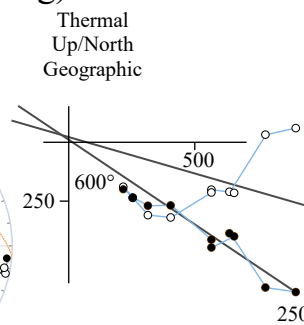
e) ALI5 D



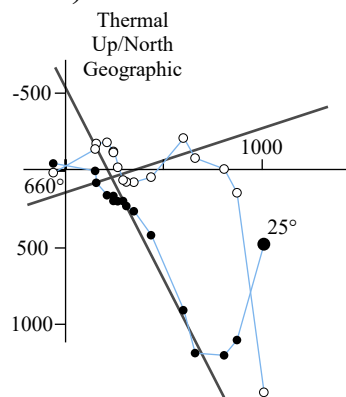
f) RC11 A



g) HUI29 F



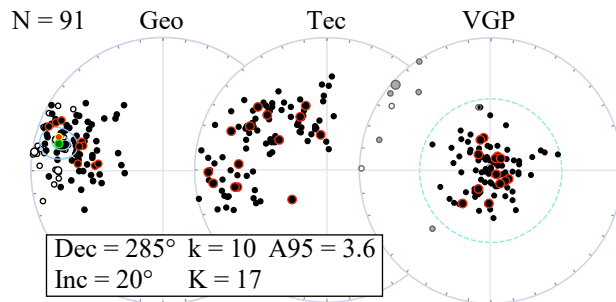
h) HUI47 B



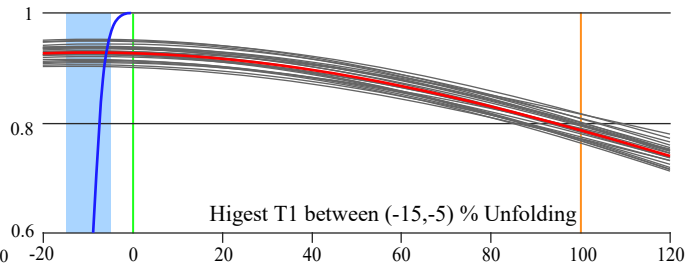
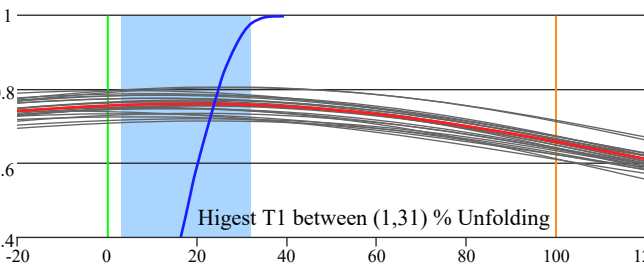
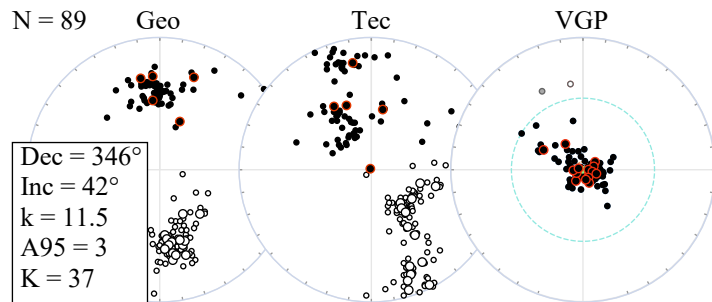
● Horizontal Projection ○ Vertical Projection ◇ Interpretation Fitted ○ Fitted Great Circle — Isolated PCA

Figure 7 Equal area projections.

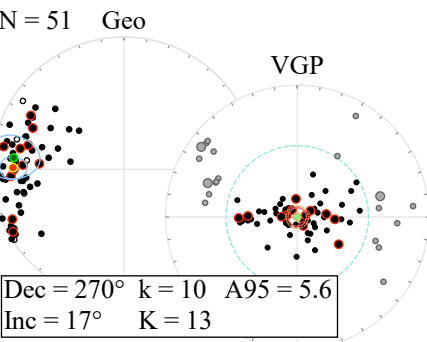
a) Mina San Miguel



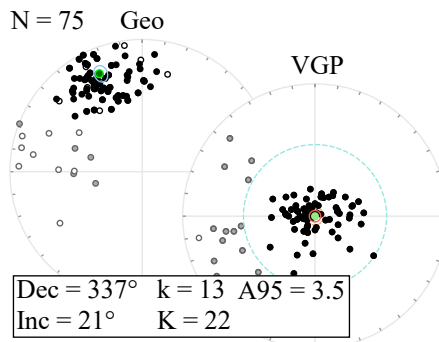
b) Real de Catorce



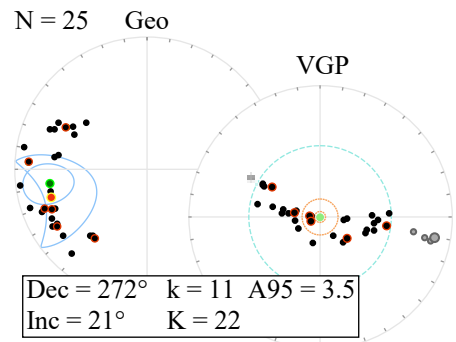
c) Caopas Intrusive



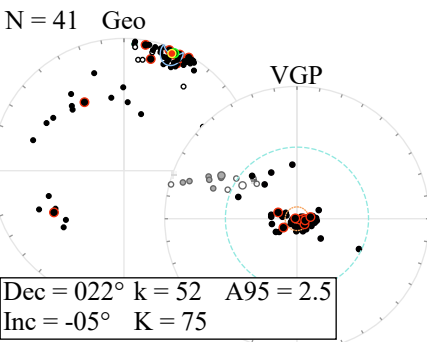
d) Huizachal



e) Nazas North



f) Charcas



g) Villa Juárez

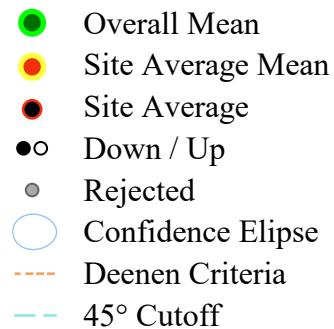
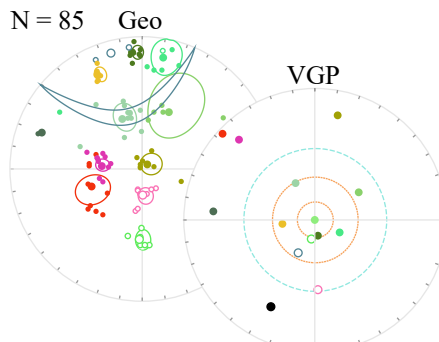
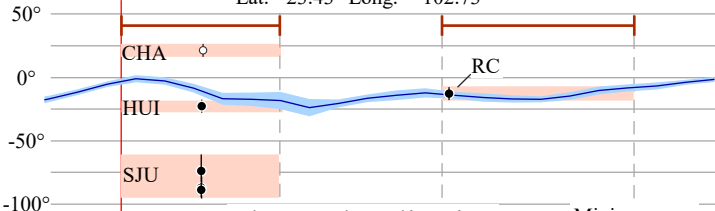


Figure 8 Observed dec-Inc.

Observed Declination

Lat. = 23.43° Long. = -102.73°



Observed Inclination

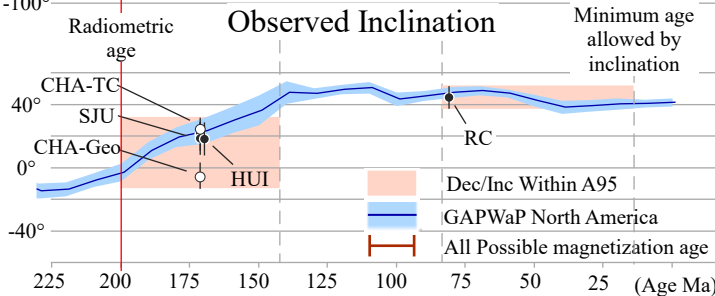


Figure 9 Rotations.

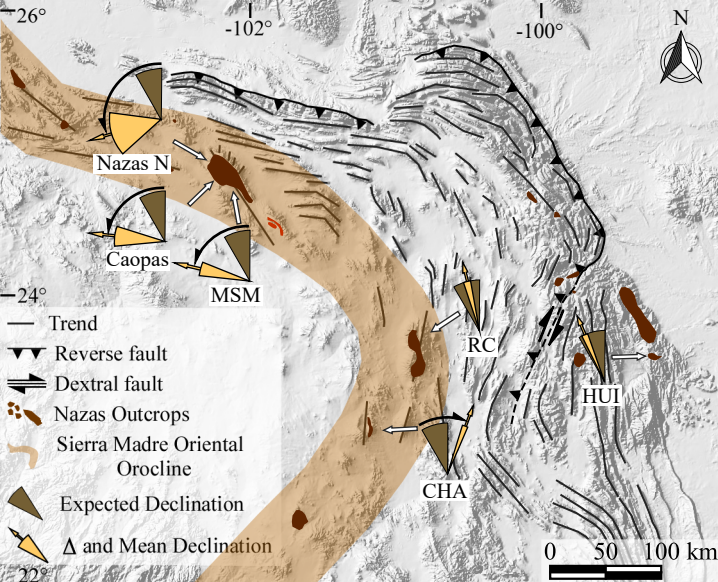


Table 1. Mean directions geographic and tectonic coordinate systems.

	N	Ns	mDec	mInc	k	a95	K	A95	A95		ΔD_x	ΔI_x
Geographic									Min	Max		
Huizachal	75	89	337.1	20.87	13.8	4.57	22.65	3.52	2.13	5.4	3.58	6.36
Charcas	41	41	22.02	-5.05	52.98	3.1	75.96	2.58	2.72	7.9	2.58	5.13
Real de Catorce	89	91	346.9	42.95	41.41	2.36	37.13	2.49	1.99	4.85	2.75	3.25
MSM	91	101	285.8	20.95	10.15	4.9	17.5	3.65	1.97	4.78	3.72	6.6
Caopas *	51	69	270.7	17.59	10.1	6.61	13.4	5.66	2.49	6.89	5.73	10.54
Nazas North *	25	37	272.5	21.41	11.56	8.9	12.61	8.49	3.31	10.79	8.65	15.28
Tectonic	N	Ns	mDec	mInc	k	a95	K	A95	A95		ΔD_x	ΔI_x
									Min	Max		
Huizachal	78	89	333.2	27.02	10.17	5.29	15.86	4.16	2.1	5.27	4.29	7.03
Charcas	41	41	20.35	30.7	52.74	3.1	75.87	2.58	2.72	7.9	2.69	4.15
Real de Catorce	85	91	326.7	39.72	9.81	5.17	13.52	4.34	2.03	4.99	4.7	6.02
MSM	73	101	294.8	35.17	7.45	6.53	8.79	5.94	2.16	5.49	6.3	8.92
Caopas *	51	69	270.7	17.59	10.1	6.61	13.4	5.66	2.49	6.89	5.73	10.54
Nazas North *	25	37	263	27.46	12.89	8.39	14.45	7.89	3.31	10.79	8.15	13.26

N number of demagnetized specimens, *Ns* number of specimens that passed the Cutoff, *mDec* mean declination, *mInc* mean inclination of the 95% confidence cone about site-mean direction, *K* precision parameter of the poles, *A95* radius of 95% confidence circle, *A95min* describe the minimum and maximum values of *A95* allowed to considered the average representative. ΔD_x , uncertainty in inclination, * Locality shows high VGP elongation see text for detail.

Pole Lng	Pole Lat	Coordinates	
		Lat.	Long.
151.59	57.74	23.587	-99.23
36.02	56.55	23.095	-101.2
185.05	77.02	23.7	-100.9
175.72	16.44	24.893	-102.1
180.79	5.38	24.834	-102.2
186.14	0.17	24.936	-102.2
Pole Lng	Pole Lat	Coordinates	
		Lat	Long.
162.1	57.42	23.587	-99.23
3.04	69.79	23.096	-101.2
182.15	56.07	23.701	-100.9
185.79	32.91	24.894	-102.1
180.79	5.38	24.834	-102.2
195.26	-9.64	24.937	-102.2

*linationg, k recision parameter, a95 radius
 le around paleomagnetic pole, A95min and
 ty in declination; ΔIx, uncertainty in*

The Sierra Madre Oriental Orocline. Paleomagnetism of The Nazas System in North-Central México

Rafael Guerra Roel¹, Daniel Pastor Galán^{2,3}, Gabriel Chávez-Cabello^{*4}, César Francisco Ramírez-Peña⁴, José Jorge Aranda Gómez⁵, Gerardo Patiño Méndez⁴, Giovanny Nova R.⁶, Alejandro Rodríguez-Parra⁷, Roberto Stanley Molina Garza^{†5}.

1 Universidad Autónoma de Nuevo León, Posgrado de la Facultad de Ciencias de la Tierra. Carretera a Cerro Prieto Km 8, Ex. Hacienda de Guadalupe, Linares N.L., México, C.P. 67700.

2 Universidad de Granada. Facultad de Ciencias de la Universidad de Granada. Av. de Fuente Nueva, s/n, 18071 Granada, España.

3 Frontier Research Institute for Interdisciplinary Science, Tohoku University, Japan.

4 Universidad Autónoma de Nuevo León, Facultad de Ciencias de la Tierra. Carretera a Cerro Prieto Km 8, Ex. Hacienda de Guadalupe, Linares N.L., México, C.P. 67700.

5 Universidad Nacional Autónoma de México, Centro de Geociencias, Juriquilla, Qro. 76230, México.

6 Instituto de Geociências, Universidade de São Paulo. São Paulo, Brasil

7. Ministerio de Minas y Energía, Colombia; Calle 43 # 57 -31, Can, Bogotá, Bogotá Colombia.

† Deceased

* Corresponding author: gabriel.chavezcbi@uanl.edu.mx

ABSTRACT

Curved mountain belts are spectacular natural features, which contain crucial 3D information about the tectonic evolution of orogenic systems. The Mesozoic units exposed at the Cordilleran Mexican Fold and Thrust belt in NE Mexico show a striking curvature that has not been explained nor included in the existent tectonic models of the region. We have investigated with paleomagnetism and rock magnetism the kinematic history of that curvature, which is observed in the rocks of the Jurassic Nazas igneous province and its overlying red beds. Our results show a complex history of remagnetizations that occurred during the Late Jurassic and Cretaceous, as well as clockwise and counterclockwise vertical axis rotations of up to 50° respectively in each limb of

the curvature. Although our data cannot provide precise timing for such rotations yet, our results confirm that the Mexican Fold and Thrust Belt underwent post-Late Jurassic orocline bending or bucking in NE Mexico.

KEYWORDS

Sierra Madre Oriental Orocline; Paleomagnetism; Mexican Fold and Thrust Belt; Remagnetization; Nazas Igneous Province.

1 Introduction

Orogenic belts are the most visible product of plate tectonics in the continents. Whereas their cross-section views are the most valuable source of information to understand orogenesis in 2D, their lateral variations are the best opportunity to understand their tectonic evolution and the curvature's kinematics in 3D (Gutiérrez-Alonso et al., 2008; Pastor-Galán, 2022). The kinematic classifications of orogenic curvatures (Johnston et al., 2013; Pastor-Galán et al., 2017; Sussman & Weil, 2004) distinguish (a) Primary arcs, which are those orogens whose curvature pre-dates the orogenic building (e.g., Jura mountains: Hindle & Burkhard, 1999); and (b) Oroclines (Carey, 1955) that are the orogenic curvatures product of vertical axis rotations. Oroclines can be classed as progressive oroclines: that is portions of orogens that were curved during the main deformation pulse, such as the Talesh (Rezaeian et al., 2020); and secondary oroclines, where the portion of an orogen was bent or buckled after the main deformation phase (e.g., the New England Oroclines, Li et al., 2012). The mechanisms that form oroclines may involve from the uppermost portion of the crust at the level where thrust faults develop (Marshak, 1988, 2004), to the whole lithosphere (Gutiérrez-Alonso et al., 2004; Pastor-Galán et al., 2012; Bagheri and Gol, 2020). Although many structural techniques can inform about the kinematics of curved orogens (Hindle & Burkhard, 1999; Kollmeier et al., 2000; Li et al., 2012; Pastor-Galán et al., 2011, 2014, 2017; Shaanan et al., 2014; Shaw et al., 2012; Weil & Yonkee, 2009; Yonkee & Weil, 2010; Bagheri and Gol, 2020), paleomagnetism is the best tool to do it, as the geomagnetic field is independent of the orogenic deformation (Abrajevitch et al., 2005; Eldredge et al., 1985; Pastor-Galán et al., 2015, 2018, 2020; Weil et al., 2001, 2010, 2013).

The American Cordillera runs along the Pacific coast of the Americas and includes several mountain belts (e.g., the Rockies, Sierra Madre Oriental and the Andes), extensive plateaus (Colorado, Atacama), primary curvatures (Colombian Eastern Cordillera: Jiménez et al., 2014); and oroclines (e.g., Alaska, Johnston, 2001; Panama, Montes et al., 2012; Bolivia, Eichelberger & McQuarrie, 2015; Patagonia, Maffione et al., 2010). The Sierra Madre Oriental is the northeastern portion of the Mexican Fold and Thrust Belt and shows a ~110 degrees curvature convex to the NE (Figure 1). The trend of this curvature is marked by outcrops of the Jurassic Nazas system (Nazas Igneous Province and associated sedimentary rock formations). This curvature has been interpreted as a primary arc representing the shape of the subduction zone during the Jurassic (Barboza-Gudiño et al., 2021; Barboza-Gudiño et al., 2014; Barboza-Gudiño et al., 2008; Dickinson & Lawton, 2001; Godínez-Urban et al., 2011; Lawton & Molina Garza, 2014; Martini & Ortega-Gutiérrez, 2018; Molina-Garza et al., 2020; Stern & Dickinson, 2010) or as the result of large-scale transcurrent faults that fragmented and displaced the Nazas system (Anderson et al., 2005; Anderson & Schmidt, 1983; Jones et al., 1995; Molina-Garza & Iriondo, 2005; Silver & Anderson, 1974). Lack of data precludes testing these or any other hypotheses since the map view kinematics of the Mexican Fold and Thrust Belt are woefully unknown. In this work, we analyze new paleomagnetic data from the Jurassic Nazas System along this curvature. Our results show counterclockwise and clockwise rotations that allow us to propose the existence of the Sierra Madre Oriental Orocline (Figure 1).

2 Geological Setting

The tectonic history of México during the past 250 million years is coupled with the eastward subduction of the Kula-Farallon (Paleo-Pacific) plates under the North American plate (Fitz-Díaz et al., 2018 and references therein). The interaction of continental and oceanic plates along the Pacific coast formed a ~ 5000 km long arc where voluminous calc-alkaline- to alkaline magmatism occurred. The arc extended from northwestern Canada (DeCelles et al., 2009) to southern México (Campa-Uranga et al., 2004; Godínez-Urban et al., 2011) and included the Nazas igneous province (a.k.a. Mesozoic arc of Western North America or the Nazas Rift Province; Barboza-Gudiño et al., 2008; Busby & Centeno-García, 2022). This magmatic subprovince was active from the beginning of the Jurassic (~200 Ma) to the Callovian (~165 Ma) (Barboza-Gudiño et al., 2008; Bartolini et al., 2003; Busby & Centeno-García, 2022; Grajales-Nishimura et al., 1992; Jones et al., 1995; Parolari et al., 2022). From Late Triassic to Earliest Cretaceous, the effects of the breakup of Pangea combined with extension related to the roll-back of the paleo-pacific plates in western

Pangea formed a series of continental and marine basins (Barboza-Gudiño et al., 2021; Busby, 2023; Martini & Ortega-Gutiérrez, 2018; Pindell & Kennan, 2001), such as the broad Mesozoic Basin of Central México (Figure 1). In the northeastern portion of that basin, sedimentation began with the accumulation of eroded materials derived from the Nazas Igneous Province. The continued extensional setting during the Oxfordian (~160 Ma) triggered a large marine transgression responsible for the accumulation of a ~ 5 km thick marine sedimentary succession (hereafter “sedimentary cover”; Bartolini et al., 1999; Goldhammer, 1999; Gray & Lawton, 2011; Hernández-Romano et al., 1997; Ocampo-Díaz et al., 2016). In the studied area (Figure 2), there is evidence of ~165 Ma plutonism. The laccolithic emplacement of the Caopas pluton (Anderson et al., 1991; Guerra-Roel, 2019; López-Infanzón, 1986; Ramírez-Peña, 2017) transferred vertical and horizontal stresses that locally deformed the overlying rocks. Afterwards, due to the accretion of the Guerrero terrain during the Early Cretaceous (Busby, 2023; Centeno-García et al., 2008; Martini et al., 2013; Ortega-Flores et al., 2020) the sedimentary rocks of the Mesozoic Basin of Central Mexico were incorporated into the Mexican Fold and Thrust Belt. The Mexican Fold and Thrust Belt style of deformation is dominated by folds and thrusts that developed over a regional decollement (i.e., thin-skinned) where the sedimentary cover was transported in a northeast direction with fold wavelengths that increase from West to East (Eguiluz et al., 2000; Fitz-Díaz et al., 2018 and references therein). The age of regional folding in the hinterland of the Mexican Fold and Thrust Belt, syntectonic plutonism (Teyra and Peñuelo plutons Ramírez-Peña & Chávez-Cabello, 2017) and synorogenic clastic sedimentation (Concepción del Oro Formation; Ocampo-Díaz et al., 2016) has been bracketed between 90 and 65 My (Fitz-Díaz et al., 2018; Ramírez-Peña & Chávez-Cabello, 2017). The Mexican Fold and Thrust Belt contains several recesses (e.g., Torreón and Potosí) and salient that portray obstacle tectonics with the forland highs (Monterrey, Figure 2; e.g., Chávez-Cabello et al., 2004; Nemkin et al., 2019; Padilla y Sánchez, 1985; Zachary, 2012). In localized areas along the trace of the Mexican Fold and Thrust Belt late high angle reverse faults cut the older folds and thrusts and expose Jurassic volcanic strata and, in some cases, Paleozoic basement (Chávez-Cabello et al., 2005; Fitz-Díaz et al., 2018; Guerra Roel, 2019; Mauel et al., 2011; Ramírez-Peña et al., 2019; Ramírez-Peña & Chávez-Cabello, 2017; Zhou et al., 2006).

2.1 The Nazas Igneous Province

The volcanic rocks of the Nazas Igneous Province (i.e., the Nazas Formation in México) crop out scattered in a winding band that crosses north-central México, and turns from a NW trend to a SE direction (Figure 1). The band is sub-parallel to the general trend of the Mexican Fold and Thrust Belt (Figure 2) The type locality of the Nazas Formation is in Cerritos Colorados near Villa Juárez,

Durango (Figure 2a; Lawton & Molina Garza, 2014; Pantoja-Alor, 1972). Isotopic ages of these rocks suggest a diachronic evolution of volcanism, with the oldest rocks (190 Ma) in the South (Barboza-Gudiño et al., 2008; Jones et al., 1995; Lawton & Molina Garza, 2014; López-Infanzón, 1986) and the youngest (160 Ma) in the northern part of the band (González-León et al., 2021; Mauel et al., 2011).

The Nazas Formation is a volcanic succession of lava flows, ignimbrites and volcanic breccias of andesitic to rhyolitic compositions interbedded with siliciclastic sediments (Barboza-Gudiño et al., 2021; Lawton & Molina Garza, 2014; Pantoja-Alor, 1972 and references therein). Its thickness is variable and ranges from 250 m to 1000 m (Clemons & McLeroy, 1965; Pantoja-Alor, 1972). Some hypabyssal and intrusive bodies with the same chemical composition and age have been attributed to the Nazas Igneous Province. These bodies are peraluminous and are interpreted as an arc setting (Barboza-Gudiño et al., 2021; Barboza-Gudiño et al., 2008; Bartolini et al., 2003; González-León et al., 2021; Mauel et al., 2011) or a rift environment as partial melting products of the Panafrican crust (Busby, 2023; Busby & Centeno-García, 2022; Martini & Ortega-Gutiérrez, 2018; Parolari et al., 2022). Bartolini et al. (2003) summarized all the reported ages of the Nazas Formation. Lawton & Molina Garza, (2014) published an updated list that included some correlated volcanic units in the United States and included zircon U-Pb ages of 180-178 Ma for the Lower member and 170-169 Ma for the Upper member. The youngest recorded ages (U-Pb in zircon) in México attributable to the Nazas Igneous Province yielded 158.1 ± 1 Ma and come from intrusive bodies exposed in Sonora (González-León et al., 2021).

2.2 Red Beds

In some localities, the top of the Nazas Formation is overlaid by a Jurassic pre-Oxfordian sedimentary succession of red sandstone, siltstone, conglomerate, breccia, and volcanoclastic reddish beds that have a direct contribution from the igneous province. These materials were deposited in continental to marine transitional environments. They are commonly addressed as Jurassic red beds and have been defined as La Joya and La Boca Formations (Barboza-Gudiño et al., 2008, 2010; Fastovsky et al., 2005; Imlay et al., 1948; Mixon et al., 1959; Rubio Cisneros et al., 2011b).

The La Boca Formation has two informal members. The lower member consists of lapilli tuffs, lava flows, volcanic breccias, and ignimbrites interbedded in equal proportion with volcanoclastics and detritus derived primarily from coeval volcanic rocks that represent deposits from the Nazas Igneous Province (Rubio-Cisneros & Lawton, 2011). The volcanic component in the La Boca

Formation gradually decreases towards the top of the stratigraphic unit. The lower and upper members are separated by an angular unconformity that ranges from a few degrees to 70°, an angle that increases in the vicinity of intrusions (Rubio-Cisneros & Lawton, 2011). The upper informal member of this formation is mostly red siliciclastic strata. These rocks fine upwards in a conglomerate, sandstone, and siltstone succession lacking fossil material (Fastovsky et al., 2005). La Boca Formation is overlain by La Joya Formation a siliciclastic unit with a basal fining upward conglomerate to reddish siltstone and mudstone. It was deposited in continental to a marginal marine environment with subordinate freshwater limestone and is overlain by the upper Jurassic-Paleogene sedimentary cover that starts with the Oxfordian Minas Viejas evaporites (Padilla y Sánchez, 1985; Rubio-Cisneros & Lawton, 2011; Salvador, 1987). The reported maximum depositional age for the La Boca Formation is 184 -183 Ma for the lower member and 167 Ma for the upper member (Rubio-Cisneros & Lawton, 2011). As for the La Joya formation its age has been inferred by stratigraphical correlation, however, Barboza-Gudiño et al. (2012) reported zircon ages as young as 166.2 ± 1.9 Ma at the top of this unit in Real de Catorce and Rubio-Cisneros & Lawton, (2011) reported a U-Pb zircon age of 163.6 ± 2.6 at its base in Huizachal Valley. Barboza-Gudiño et al., (2021) presented a complete summary of the stratigraphy and lithological correlations of all the known localities of the Nazas Igneous Province in Mexico.

During the last recorded episode of horizontal crustal shortening of the Mexican Fold and Thrust Belt (Upper Cretaceous-Eocene), these Jurassic units were exhumed in some parts of the thrust belt (Figure 2b; Fitz-Díaz et al., 2018; Gutiérrez-Navarro et al., 2021; Lawton & Molina Garza, 2014; Ramírez-Peña et al., 2019; Ramírez-Peña & Chávez-Cabello, 2017).

3 Sampling Strategy

We collected a total of 620 core samples of 2.5 cm diameter with a gas-powered drill and oriented them with a Pomeroy orienting fixture and a Brunton Pocket Transit compass. 355 cores come from the Nazas Formation and the remainder 265 from the red bed formations that overlay it. In some localities, we collected oriented blocks and later drilled them in the laboratory. The Nazas Formation samples were collected in three separate localities representing different trends of the Nazas Igneous Province (Figure. 2a): (1) Villa Juárez locality in the state of Durango, located 20 km west of the city of Torreon, Coahuila; (2) The San Julián Uplift locality, in the northern part of the state of Zacatecas; and (3) Charcas which is located 7 km west of the city of the same name in the state of San Luis Potosí. The sedimentary rocks were collected from the La Joya and La Boca Formations: (1) Real de Catorce located in the Sierra de Catorce also in the state of San Luis

Potosi; and (2) in the Huizachal Valley, 18 km SE of the city of Ciudad Victoria, Tamaulipas (Figure 2b).

3.1 Villa Juárez, Durango (25.501°N, -103.621° E)

The local age of the volcanic rocks in this locality is 200-178 Ma for the lower member and 170-169 Ma Upper member (Barboza-Gudiño et al., 2021; Lawton & Molina Garza, 2014). We collected between 2 and 3 oriented blocks in each of the 17 sites (labeled NA01-NA17) from 4 individual andesitic lava flows. We obtained a total of 85 cores from the oriented blocks. Lava flows are interbedded with volcano-sedimentary rocks in the Villa Juárez anticline, which has an axial trend and plunge of $\sim 315^\circ/18^\circ$. The sampled limbs do not show noticeable evidence of penetrative deformation. Although the precise age of the folding is unknown, the structure is attributed to thin-skinned deformation coupled with the buttressing effect of the Coahuila block, an adjacent basement high. Sediments accumulated in the basin were thrust over the southern margin of the block during the Late Cretaceous (Lawton & Molina Garza, 2014).

3.2 San Julián Uplift (24.837°N, -102.174° E)

The San Julian Uplift is a basement block that contains the largest outcrop of the Nazas Formation in México. The block was exhumed during Eocene-Oligocene thick-skinned tectonic event (Guerra-Roel, 2019; Ramírez-Peña, 2017; Ramírez-Peña et al., 2019; Ramírez-Peña & Chávez-Cabello, 2017). The thick-skinned faults cut in high angles the pre-existing Cretaceous thin-skinned structures, which formed during the early stages of development of the Mexican-Fold and Thrust Belt. The NE limit of the San Julián Uplift is the Las Norias fault zone, a high-angle reverse fault that disrupted and refolded the overlying anticlines tilting them towards the NE (Guerra-Roel, 2019, Ramírez-Peña 2017).

In this locality, the Nazas Igneous Province system is represented by volcanosedimentary, volcanic, and sub-volcanic rocks of the Nazas Formation, and the Caopas intrusive body (Gómez-Torres, 2022; López-Infanzón, 1986; Ramírez-Peña, 2017; Rogers et al., 1963). The volcanic rocks of the Nazas formation upper member are primarily composed of andesitic and dacitic lava flows, volcanic domes, and associated volcanic breccias. The Nazas Formation lower member is locally constituted of metasedimentary material, tuff, ash, breccia, and andesitic lava flows. These rocks show foliation and low metamorphic grade of greenschist facies with chlorite as the main metamorphic mineral. The zircon U-Pb age for the Nazas Formation in this locality is 174 ± 2 Ma (Ramírez-Peña, 2017). The Caopas intrusive corresponds to a Middle Jurassic plutonic body of

intermediate composition emplaced in the Nazas Formation. This body shows a porphyritic texture and, in some of its upper parts, evidence of dynamic metamorphism (porphyroblasts and mineral lineation). The Caopas intrusive yielded a U-Pb in zircons age of 165 ± 3 Ma (Ramírez-Peña, 2017).

From this locality, we collected a total of 256 samples in three separate areas: Mina San Miguel (coded MSM), Nazas North (ALI, NRN), and the Caopas intrusive body (MIC, MIR, MIRN; supplementary table ST2). The samples corresponding to the Mina San Miguel were collected in an anticline at the eastern border of the San Julián Uplift; and the Nazas N sites came from the northern part of the block. All the samples belonging to the MSM area and sites Mic1, Mic2, and Mic3 of the Caopas intrusive were drilled in situ (10-15 samples per site). The rest of the sites of the Caopas area (Mic4 – Mic7) were collected as oriented blocks (one per site). From each block, we obtained four cores in the laboratory. The poor outcrop exposure of the lava flow succession in the MSM and Nazas N areas, together with their thickness (20-30 m), weathering conditions, and compositional and textural similarities among flows made the task of identifying individual lava flows a challenge.

The Nazas Formation in the MSM area shows folds with trend/plunge of $142^\circ/10^\circ$ that is oblique to the main East-West trend of the structures in the transversal sector of the Mexican Fold and Thrust Belt (see Parras thrust in Figure 2). A second series of younger folds with N- to NE-trends was recognized by Ramírez-Peña (2017) and Guerra Roel (2019). This structural trend is absent in rocks of the Nazas Formation, but it is characteristic of the eastern borderline structures of the San Julián Uplift.

3.3 Charcas, San Luis Potosí (23.131°N , -101.188°E)

The Nazas Formation in Charcas is composed by lava flows and pyroclastic rocks of andesitic composition, interbedded with volcanoclastic material and volcanic breccias. These rocks were dated (U-Pb in zircon) in 179 ± 1 Ma (Zavala-Monsiváis et al., 2012). Jurassic red beds overlie unconformably the Nazas Formation. The structure and exhumation mechanism has not been studied in detail in this locality, and it is only described as an anticlinorium. However, it is noted that the structure is in the same crustal block as the Real de Catorce locality (see 3.4).

In this locality we collected samples along the San Antonio River covering about 80 m of the exposed stratigraphic succession of the Nazas Formation. The outcrop is composed by a stack of lava flows, and volcanic breccia of andesitic composition interbedded with thin ignimbrites and

ash-fall tuffs. 60 cores were collected in 10 sites of the Nazas Formation labeled **CHA-1 to CHA-10** that cover four different andesitic lava flows, interbedded tuff, and epiclastic deposits. Each sampled site corresponds to distinct units no thicker than 2 m, with the exception of sites CHA-1 and CHA-2 that were collected from a single epiclastic deposit.

3.4 Real de Catorce (23.621°N, -100.855° E)

In this locality, the older rocks crop out in the core of an antiformal stack (Gutiérrez-Navarro et al., 2021). The antiformal stack structure formed between 91-52 Ma, based on an $^{40}\text{Ar}/^{39}\text{Ar}$ age obtained from neogenic illite collected from a shear zone (Gutiérrez-Navarro et al., 2021). The cooling ages of ~50 Ma (U-Pb-He in zircon) from a dacitic pluton emplaced in the Nazas Formation have been interpreted as the exhumation age due to deep high-angle reverse faults (thick-skinned event), which delimit the Real de Catorce block. The Nazas Formation unconformably rests atop Triassic clastic rocks of the Potosí fan (Centeno-García et al., 2005; Silva-Romo et al., 2000) and yielded U-Pb age of 174.7 ± 1.3 Ma in zircon. (Barboza-Gudiño et al., 2012). The La Joya Formation lies unconformably over the Nazas Formation. In this locality, The La Joya Formation is composed of a 200 m thick sedimentary succession of continental (bottom) to marginal marine (top) conglomerates, sandstones, and shale in a grain-decreasing order from bottom to top. This Formation shows signs of deformation features that suggests that it acted as a decollement, which was developed in the Late Cretaceous during the thin-skinned deformation event (Gutiérrez-Navarro et al., 2021). The La Joya Formation's maximum depositional U-Pb age, inferred from detrital zircons is 166.2 ± 1.9 Ma (Barboza-Gudiño et al., 2012).

We sampled 103 cores in the Real de Catorce area in a coarsening upward 60 m thick succession of sandstones. The samples were collected on the fine-grain portion of the outcrop and distributed in 16 sites labeled **RC11 - RC26**. Each core accounts for a single bed.

3.5 Huizachal Valley (23.588°N-99.222° E)

The locality contains outcrops of the Nazas Formation in the core of a structural dome overlain by the Jurassic red beds of the La Boca and La Joya Formations (Rubio-Cisneros & Lawton, 2011). The top of the Nazas Formation is interbedded with the clastics of the lower member of La Boca Formation and they are separated by an angular unconformity. This lower member consists of lapilli tuffs, lava flows, volcanic breccias, ignimbrites and rhyolites interbedded with volcanoclastics with detritus derived primarily from volcanic rocks of the Nazas igneous province.

The volcanic component in the La Boca Formation gradually decreases towards the top of the stratigraphic unit (Rubio-Cisneros & Lawton, 2011). The La Boca Formation has been divided into two informal members separated by an angular unconformity that ranges from few degrees to 70° (Rubio-Cisneros & Lawton, 2011). The upper member consists of a fining upwards red beds succession that includes conglomerate, sandstone, and siltstone beds with scant fossils (Fastovsky et al., 2005). La Boca Formation is overlain by La Joya Formation. Both formations were deposited in continental to marginal marine environments (Rubio Cisneros et al., 2011a; Salvador, 1987). Detrital zircon analysis in this locality places the maximum deposition age of the La Boca Formation at ~190 Ma (Rubio-Cisneros & Lawton, 2011), as for the La Joya Formation maximum depositional age, inferred from detrital zircons is ~166 Ma (Venegas-Rodríguez et al., 2009). We drilled 105 samples from La Joya and La Boca Formations in this locality. The sampled formations crop out at the core of an anticline along the valley. Seven sites, with a total of 45 samples, labeled **HUI42 – HUI48** correspond to La Boca Formation, which consists of fine to coarse red sandstones. Samples were collected in the middle portion of the upper member, closer to the anticline axis. 62 cores distributed in nine sites labeled **HUI28 – HUI40** were collected from the La Joya Formation on the northwestern limb of the anticline, in an outcrop that lays along a secondary dirt road approximately 1 km SW from the previously sampled La Boca Formation. Each site sampled comprises a single stratum of about two meters thick.

4. Methods and Results

4.1 Isothermal Remanent Magnetization (IRM) and Hysteresis Loops

4.1.1 Villa Juárez

Isothermal Remanent Magnetization (IRM) curves were obtained at the Paleomagnetism and Magnetism Laboratory at the Centro de Geociencias of the Universidad Nacional Autónoma de México. The procedure was carried out using an in-house built impulse magnetizer which is capable of generating fields up to 5 T. The acquired magnetization was measured in a JR6 spinner magnetometer from AGICO. Eleven samples belonging to eight sites in the Villa Juárez locality were selected for IRM acquisition curves (NA01, NA02, NA05, and NA10 of andesitic and tuff composition along with volcano-sedimentary samples labeled NA04, NA06, NA07, NA08). In this process, we induced an IRM in a progressively increasing field (20 – 2900 mT) and afterward, we

applied a back-field demagnetization in a progressive order (10 – 700 mT) following the method described by Kruiver et al. (2001)

IRM curves were unmixed using the MAX Unmix web application (Maxbauer et al., 2016) to determine the main magnetic minerals contributing to the cumulative IRM. The Gradient Acquisition Plots (Figures 4a and 4b) show two components in the coercivity spectra. One with a mid-saturation value $\log B_{1/2}$ between 2.85 and 3 (Figure 3b), and a second one between 1.7 and 2. Most of the results show a gradual increment towards the 1 T and higher and the samples do not reach saturation at 3 T. From the analyses, we infer two mineral phases with distinct coercivities, a “soft phase” that we identified as magnetite with H_{cr} that varies between 50 – 100 mT and a “hard phase” with values between 700 and 1000 mT, possibly hematite. The main contribution to the coercivity spectra is given by the $\log B_{1/2} > 100\text{mT}$ and $< 1000\text{mT}$, which is usually accredited to phases of hematite and is present in both volcanic and volcano-sedimentary rocks of this locality. The remaining IRM unmixing graphs are available in Supplementary file SF1.

4.1.2 San Julián

IRM and hysteresis loops were obtained in a Micromag model 2900 with two Tesla magnets, Princeton Measurements Corporation, noise level $2 \times 10^{-9} \text{ Am}^2$ in the Paleomagnetism and Magnetism Laboratory at the Centro de Geociencias of the Universidad Nacional Autónoma de México. Curves were measured on representative specimens of the sampled localities. These tests were made at room temperature and a field of 1 T was applied in 10 mT increments. The results show noisy curves and are similar for most of the samples. The minerals that hold the NRM for the volcanic samples reach saturation in the range below 400 mT suggesting that their remanence is controlled by ferrimagnetic phases (probably Ti-magnetite; Gubbins & Herrero-Bervera, 2007; Supplementary file SF2).

At the same time, we also measured hysteresis loops at room temperature on a Micromag model 2900 with two Tesla magnets, Princeton Measurements Corporation, noise level $2 \times 10^{-9} \text{ Am}^2$. In total we measured 26 representative samples. Samples mass ranged from 40 to 50 mg and were measured using a P1 phenolic probe. The maximum applied field was 1 T in increments of 20 mT on an average time of 600 ms. The coarse grain texture of the Caopas intrusive along with the scarcity of magnetic mineralogy resulted in noisy results (dia-/para- magnetic) for the intrusive rock samples. Although the curves did not reach saturation at 1 T, interpretable results both show

hysteresis loops that resemble those of superparamagnetic magnetite (grain size <10 nm; Dunlop & Özdemir, 1997) with a possible minor content of a hard phase (likely hematite: Figure 3f). The NRN sites of the sampled andesites from Nazas North area (Figure 3e) also shows a hysteresis loop with a high coercivity phase that does not saturate at 1 T, we also interpret this phase as hematite (Gubbins & Herrero-Bervera, 2007).

4.2 Thermomagnetic curves

4.2.1 Villa Juárez

We performed the thermomagnetic curves for this locality in the Ivar Giæver Geomagnetic Laboratory (University of Oslo) on a Kappabridge AGICO MFK1-FA equipped with a CS-4 furnace and processed with Cureval8 (AGICO) (Chadima & Hrouda, 2009) and were corrected for stability values and density. We measured the magnetic susceptibility in runs from 0° to 700 °C in an Ar atmosphere in nine selected pulverized samples. Irreversible curves are evident due to mineralogical alterations during heating, in most of the curves a drop in susceptibility is noticed around the Curie temperature for low Ti-magnetite (~580 °C), and in some cases a less evident drop around the Néel temperature (~700 °C) for hematite (Figure 2c and supplementary file SF5).

4.2.2 San Julián

We performed one thermomagnetic analysis per site in the San Julián locality in an in-house built horizontal translation type Curie balance with a sensitivity of approximately 5×10^{-9} Am² in the Paleomagnetism and Rock Magnetism Laboratory of the Centro de Geociencias, Universidad Nacional Autónoma de México (UNAM, Querétaro). Due to the small amounts of magnetic material in some of the samples, the tests were carried out on concentrates previously separated using hand magnets. Between 300 to 400 mg of ground, sample was used for each experiment. The Curie balance was programmed to continuously heat the sample to 700 °C and gradually cool to room temperature at heating and cooling rates of approximately 10 °C min⁻¹.

Curves for all the volcanic samples progressively demagnetized when heating, some samples showed sharp drops in magnetization in temperatures between 600 and 700 °C indicative of hematite (O'Reilly, 1984). In other samples (e.g., MSM7), magnetization started to decrease around the 500 °C (supplementary file SF4b), which may indicate the coexistence of magnetite and hematite (Dunlop & Özdemir, 1997). Some curves showed a subtle presence of sulfides

suggested by a small magnetization increase between 400 and 500 °C (e.g., De Boer & Dekkers, 1998). On all the volcanic samples we could only see a major phase with mineralogical alteration during heating, commonly hematite to maghemite due to temperature increment (Dunlop & Özdemir, 1997), and in some cases paramagnetic curves (Gubbins & Herrero-Bervera, 2007). Samples from the Caopas intrusive show analogous behavior as the volcanic samples (Supplementary file SF4a).

4.3 Anisotropy of Magnetic Susceptibility (AMS)

Anisotropy of magnetic susceptibility (AMS) is a sensitive technique that has several applications. We applied this methodology as a proxy for describing deformation in weakly deformed rocks (e.g., Parés, 2015; Weil & Yonkee, 2009). Graphically we represent AMS as an ellipsoid whose principal axes are $k_{\max} > k_{\text{int}} > k_{\min}$ (e.g., Parés, 2015 and references therein). The shape of the AMS ellipsoid depends on different features such as the orientation of mineral grains, compositional layering, the crystallographic orientation of individual minerals, distribution, and size of microfractures, and the grain shape and size (e.g., Butler, 1992; Tarling & Hrouda, 1993). The analyses were carried out in a Kappabridge model KLY-3 in the Paleomagnetism and Rock Magnetism Laboratory of the Centro de Geociencias, Universidad Nacional Autónoma de México (UNAM) in Juriquilla Querétaro, México. We present the AMS ellipsoid in terms of equal area projection (Figure 4) and shape parameter graphs both Flinn, (1962) and Jelinek, (1981) diagrams available in Supplementary file SF6.

4.3.1 San Julián

AMS results for this locality show uniform mean anisotropies close to the mean ($K_m \approx 592.7 \times 10^{-9}$) for both the Caopas and MSM areas. The anisotropy value (P) is low for the MSM area (< 1.02). In contrast, the Caopas intrusive shows slightly higher and more variable values (1.032-1.343). The results for both areas show pseudo-isotropic geometries and no apparent penetrative deformation. The MSM locality, Kmin axes are parallel to the poles of the lava-flow bedding describing an antiformal structure (Figure 4a). After unfolding, the Kmin axes group on the vertical, following the bedding data, suggesting a pre-folding vertical fabric (Figure 4a). The Caopas intrusive and the MSM areas show low anisotropy values that are archetypal pseudo-isotropic geometries. The Caopas intrusive locality shows a good grouping of the Kmin axis on the vertical which is representative of an internally undeformed intrusive body that only recorded the effects

of magmatic flow and gravity (Figure 4d). At the same time, the general direction of the magnetic lineation (Kmax) corresponds to the direction of the mineral lineation (NE-SW) observed on the field (Guerra- Roel, 2019).

4.3.2 Villa Juárez

The mean anisotropy value (Km) varies per site from 1.95×10^{-05} to 1.59×10^{-04} with mean values of 7.36×10^{-05} . And most of the samples show oblate shapes with low degree of anisotropy ($P = 1.026$). The results of the AMS ellipsoid show widespread distribution and poor grouping (Figure 4b). This behavior could represent an undeformed volcanic rock, which is consistent with field observations.

4.3.3 Charcas

The magnetic susceptibility (Km) in the analyzed samples from the Charcas locality, varies from 120.9×10^{-06} to 335.3×10^{-06} with a mean value of 207.8×10^{-06} and a $P = 1.24$. Samples from sites CHA1, CHA2, CHA4, CHA9, and CHA10 show oblate geometries. Sites CHA3, CHA5, and CHA8 show both prolate and oblate, and CHA6 and CHA7 only show prolate geometries (Supplementary file SF6). Kmin axes are parallel to the poles of the bedding except for sites CHA2, CHA3, and CHA6. AMS in Charcas seems to respond, at least partially, to loading (Figure 4c).

4.4 Scanning Electron Microscopy (SEM) and polarized light Microscopy

We analyzed the samples using a Scanning Electron Microscope (SEM) model TM-1000 Hitachi equipped with energy-dispersive X-ray spectroscopy (EDS: Oxford). This procedure was done in the Laboratory of Crustal Fluids in the Centro de Geociencias, Universidad Nacional Autónoma de México (CEGEO UNAM, Querétaro).

4.4.1 Villa Juárez

The SEM images were complemented with EDS scans that showed percentages of the elements present in the minerals (Supplementary file SF7). The images for this locality show the presence of Ti-Magnetite set in a non-conductive granular matrix (Figure 5a). Additionally, lamellar hematite crystals were observed in this locality (Figure 5b, see also supplementary file SF7).

4.4.2 San Julián

The results show the presence of anhedral magnetite crystals surrounded by hematite weathering rims. Hematite is also present as a secondary mineral that filled the fractures and, to a lesser extent, along the crystal cleavages of amphibole phenocrysts. These two magnetic mineral phases are the most prominent in the samples from this locality (Figures 5c and 5d, see also supplementary file SF7).

4.5 Paleomagnetism

We progressively demagnetized the samples using thermal (TH) and alternating fields (AF) demagnetization procedures. The paleomagnetic directions were analyzed with Paleomagnetism.org software (Koymans et al., 2016, 2020), which uses principal component analysis to define magnetic components (Kirschvink, 1980) and Fisher (1953) statistics to calculate averages and errors in directions and virtual geomagnetic poles (VGPs). Only directions with five or more demagnetization steps in line and maximum angular deviation (MAD) $< 15^\circ$ (McElhinny & McFadden, 1999) were considered as valid directions. We applied a 45° cut-off in each site to discard outlying points. We also used the McFadden & McElhinny (1988) method of combining great circles and best-fitted set point directions for samples where components were difficult to isolate (Figure 6). Two localities allow for a fold test (MSM and Real de Catorce localities: Figure 7).

Additionally, the reliability of each data set was tested with Deenen et al. (2011) criteria, that in general terms evaluates the scatter of VGPs. This criterion denotes that the ellipticity of the VGP scatter is the effect of paleosecular variation (PSV) and that a proper VGP distribution tends to be circular. Nonetheless, unaccounted structural corrections, inclination shallowing, and or vertical axis rotations may add additional scatter (ellipticity) to the associated distribution. Finally, to test the reliability of data from unique lava flows, we have compared the differences between the average of site means within a locality against the average of all individual directions (Figure 7). Summary of locality means is shown in Table 1.

Most of the samples from all localities show a low temperature/low coercivity component ($< 200^\circ\text{C}$ and $< 16\text{ mT}$.) that roughly fits with the Geo-axial dipole (GAD) expected for NE México during the Holocene. We interpret this component as a viscous remanent magnetization. (*e.g.*, Figure 6a) (Supplementary file SF8).

4.5.1 Villa Juárez (Nazas Formation)

The samples of this locality were demagnetized and measured in the shielded room of the Ivar Giæver Geomagnetic Laboratory in Norway. We demagnetized the samples in progressive variable steps using thermal and alternating fields demagnetization using a furnace model MMTD8oA for TH and an alternating fields demagnetizer model LDA-3A. After initial pilot tests, we determined that AF demagnetization was ineffective due to the presence of a high coercivity mineral (hematite). The NRM was measured in a superconducting rock magnetometer WSGI model 755 (2G Enterprises). The Zijderveld diagrams (Zijderveld, 1967) show a single component that progressively demagnetizes to the origin (Figure 6d). The ChRM components were isolated at high temperatures (~450 – 700 °C). At the site level, the direction means show high precision parameters in all samples but three ($k > 45$), whereas 5 out of 10 sites with $n > 3$ samples show $k > 100$, which we consider spot readings of the geomagnetic field. However, site averages do not concentrate ($k < 2$, without a cut-off and $k = 13$ after discarding more than half of site averages). Some site directions may represent reversed chrons, however, data is too scarce to confirm. For this reason, we were not able to obtain a mean dec/inc of this locality (results are available in Supplementary Table ST1).

4.5.2 San Julián Uplift (MSM, Caopas, and Nazas North)

We analyzed the samples from this locality in the paleomagnetism and rock magnetism laboratory in the Centro de Geociencias, UNAM Querétaro. The remanent magnetization was measured using an AGICO JR-6 spinner magnetometer. Thermal (TH) and Alternating Field (AF). Demagnetization was performed in a magnetically shielded room using a shielded furnace with a heating capacity up to 640 °C in increasing steps of 50 °C up to 500 °C. From 500 °C to 640 °C was finished 20 °C increments. After pilot tests, we determined that AF demagnetization was ineffective due to the presence of a high coercivity mineral (hematite).

Upon demagnetization, we identified a Characteristic Remanent Magnetization (ChRM) with a downward inclination and westerly direction, isolated between 500°-580 °C and 40-60 mT. We named this component W (for west). This component was present in 12 sites of the MSM locality (Figure 6a), 15 sites of the Caopas intrusive (Figure 6b), and 7 sites of the Nazas N (Figure 6e) in a total of 129 samples (for site mean parameters see Supplementary Table ST2). The W component in the MSM area shows a mean dec/inc of 285°/ 21° (geographic coordinates) downward and single polarity with a k of 10 and $K = 17.4$. The VGP projection is well rounded and the A95 value is in between the maximum and minimum of the Deenen (2011) envelope, suggesting that the

observed distribution scatter can be explained only as a function of the PSV. The dispersion (k) at the site level ranges between 20-50 with only MSM5 and MSM3 over 200 and MSM10 with the lowest (13) (Table 1). The fold test (Tauxe & Watson, 1994) shows a maximum between 1 and 31% unfolding (Figure 7a). This negative fold test reveals that the W component in MSM is the product of a post-folding remagnetization. The average of means and overall average show akin results (Figure 7a).

The W component in the Caopas intrusive shows progressive demagnetization and high unblocking temperatures between 400 and 560 °C (Figure 6b), and an average dec/inc 271°/ 17° in geographic coordinates (Figure 7c) with a precision parameter $k= 10$. The VGPs plotted for this area have a K of 13.40 and an $A95$ of 5.66 in between the $A95_{min}$ and $A95_{max}$ envelope (Table 1). The VGP plot reveals an elliptical shape, elongated W-E (Figure 7c). Despite being within Deenen's limits, we think that the elliptical shape indicates an external cause of additional scatter apart from PSV. We suspect an unaccounted structural or magnetic acquisition problem. Thus, we used this result with caution.

The last group of samples in the San Julián Uplift "Nazas North" behaves similarly but with larger dispersion for the W component. This locality lies on the northern part of the San Julián Uplift and they lack reliable structural correction due to poor exposure in the area. The mean dec/inc of the W component is 261°/26° and has a dispersion parameter $k= 8.3$. With almost 20° of Δ inclination and 11° Δ declination (Table 1). The directions in this area seem to follow a great circle and it shows an elongated W-E VGP projection (Figure 7e). Its $A95$ of 11.21 is larger than Deenen's $A95_{max}$, indicating additional sources of scatter not attributable to PSV. Although we cannot precisely identify the additional source of scatter, we think that it might be due to unidentified structural problems or magnetic acquisition. "Nazas North" area did not provide a dataset with enough quality to quantify vertical axis rotations or latitudinal motion. However, its average declination and inclination are analogous to MSM and Caopas intrusive areas reinforcing their meaning.

4.5.3 Charcas (Nazas Formation)

We performed part of the paleomagnetic analyses of this locality in the Paleomagnetism and Rock magnetism Laboratory of the Universidad Nacional Autónoma de México, Centro de Geociencias (UNAM, Querétaro) with an AGICO JR-6 spinner magnetometer. The rest of them were processed

in the University of Texas at Dallas (UTD, Geoscience Department Paleomagnetism and Rock Magnetism Lab) with the use of a cryogenic magnetometer 2G Enterprises. All demagnetization process was performed with AF. The components isolated by this procedure show a straight demagnetization line to the origin (Figure 6c) with low MAD (<5), only on sites CHA1, CHA9, and CHA10 (17 samples). Samples from sites CHA3, 4, 5, and 6 (22 samples) show little demagnetization, due to the presence of hematite, but all of them tend to the origin with analogous directions to CHA9 and CHA10. The component was isolated between 35 and 90 mT. CHA3 to CHA10 group well with a $\text{dec/inc} = 22^\circ/-05^\circ$ and $k = 53$; $K = 76$; and $A95 = 2.58$ (Table 1). Samples from CHA1 and CHA2 are different and discardable by any statistical cut-off criterion (Figure 7f). The dispersion parameter before and after tectonic correction is $k > 50$ and $K > 70$ in both specimen and site mean averages (Supplementary table ST3). This data suggests that sites CHA3-CHA10 represent a single spot-reading of the geomagnetic field, either because all sample layers represent a single cooling unit or because they were quickly remagnetized later.

4.5.4 Real de Catorce (Red beds “La Joya Formation”)

The samples were measured in the laboratories of the UNAM Querétaro and at UT Dallas, Texas. These samples were thermally demagnetized in progressive steps from 100 °C up to 670 °C. Samples show a single ChRM component showing a gradual demagnetization to the origin (Figure 6f). Overall results group around two sets of directions: one with $\text{dec/inc} = 358^\circ/40^\circ$ and $k = 45$, which is similar to the Holocene GAD for México; and a second one with reverse polarity $\text{dec/inc} = 166^\circ/42^\circ$ and $k = 41$. These two directions do not share a bootstrapped common true mean direction (Tauxe, 2010). However, they are not far from it, being the reversed component slightly rotated counterclockwise ($< 10^\circ$) (Figure 7b). The data of this locality allowed for a fold test (Tauxe & Watson, 1994) (Figure 7b). The fold test is negative with a maximum grouping between -15% to -5% unfolding. The VGPs projection shows a rounded shape (Figure 7b). By flipping the reversed directions, we obtain a mean dec/inc of $346^\circ/42^\circ$ with a k value of 41 (see Table 1, for site means see also supplementary table ST4).

4.5.5 Huizachal Valley (Red beds “La Joya and La Boca Fm”)

The samples of the Huizachal locality were analyzed in the laboratories of the UNAM, Juriquilla, Querétaro and at UT Dallas, Texas. We demagnetized all samples thermally following progressive heating steps from 100 °C up to 670 °C (Figure 6g). We identified a component isolated in the

temperature range between 450 °C and 650 °C combining 57 directions with 33 great circles (McFadden & McElhinny, 1988). This component has a mean dec/inc of 160°/-26° upwards with a $k = 14$, $K = 22$, and $A95 = 3.5$ (Table 1 for site means see also supplementary table ST5). The VGPs projection shows a roughly circular shape with a slight ellipticity W-E possibly indicating tectonic-induced scatter (Figure 7d).

5 Discussion

The curvature of the Sierra Madre Oriental that the Nazas System draws in North Central México has been mostly overlooked. The Nazas Igneous Province outcrop pattern has been interpreted as the result of: (1) Large scale left lateral faulting during the Late Jurassic (Anderson et al., 2005; Anderson & Schmidt, 1983; Jones et al., 1995; Molina-Garza & Iriondo, 2005; Silver & Anderson, 1974), or (2) The direct result of a curved segment in the subduction zone, thus representing a primary arc in the kinematic classification for curved orogens (Barboza-Gudiño et al., 2014; Barboza-Gudiño et al., 2008; Dickinson & Lawton, 2001; Godínez-Urban et al., 2011; Lawton & Molina Garza, 2014; Martini & Ortega-Gutiérrez, 2018; Molina-Garza et al., 2020; Stern & Dickinson, 2010). In our investigation of the studied area, we have found a tangled history of remagnetizations and vertical axis rotations, which are the result of a complex tectonic history that involved orocline bending or buckling.

5.1 Magnetization processes and timing: a complex puzzle

Our sample collection came from the Nazas system in NE México as defined by different authors (Barboza-Gudiño et al., 2004; Busby & Centeno-García, 2022; Lawton & Molina Garza, 2014; Parolari et al., 2022; Rubio-Cisneros & Lawton, 2011; Zavala-Monsiváis et al., 2012). All available data from these outcrops suggest that they share the same tectonic history and define an ~110° curvature (Fitz-Diaz 2018). The Mesozoic and Cenozoic geological history of NE México is complex and includes a wide range of tectonic processes: such as subduction, transtension, terrain accretion, folding and thrusting, and extension; all of them capable of producing remagnetizations and vertical axis rotations.

We think that the Villa Juárez locality is the only one from our collection whose magnetization is primary. Each site from this locality corresponds to a single lava flow. Lava flows cool quickly and record snapshots of the magnetic field. Therefore, many lava flows representing enough time

are needed to average out PSV (Deenen et al., 2011; Gerritsen et al., 2022). Most of our sites from the Villa Juárez locality show high concentration parameters (k) that are consistent with spot-readings of the geomagnetic field (Deenen et al., 2011; Gerritsen et al., 2022; Figure 7g and Supplementary table ST1). Although some remagnetization processes can produce high concentration parameters (e.g., Pastor-Galán et al., 2021) they usually remagnetize all lava flows from a rather small sampling area like Villa Juárez. In this locality, the average declination and inclination obtained from each lava flow differ noticeably (Figure 7g), and site averages fail to group around VGPs that resemble the GAD's PSV despite the strong consistency within each lava flow. We think that this particular result is the consequence of a primary magnetization acquired during the 195-180 Ma lapse, a time when the magnetic field was quite unstable and reversed and excursed frequently (e.g., Ogg, 2020). Unfortunately, our sampling did not include a large enough number of lava flows to average such a highly variable PSV. The dataset, therefore, does not meet the current reliability criteria (e.g., Gerritsen et al., 2022; Meert et al., 2020). In this locality, we have identified magnetite and hematite as the magnetic carriers (Figures 3a, 3b, and 3c). SEM images (Figure 5a and 5b) show a texture of well-formed euhedral to subhedral crystals of magnetite and hematite with no apparent neo-forming minerals, signs of alteration, weathering, nor apparent penetrative deformation, which supports the primary magnetization origin for Villa de Juárez locality. We, therefore, interpret an Early Jurassic (195 ± 7 My) magnetization corresponding with lava cooling (Barboza-Gudiño et al., 2021).

The samples collected at three areas of the San Julián Uplift locality (Mina San Miguel, Caopas, and Nazas North) contain the same two main magnetic carriers (hematite + magnetite), both documented in rock magnetic analyses (Figures 3d, 3e, and 3f) and in SEM studies (Figures 5c and 5d). However, in the MSM area hematite is associated with a secondary texture (newforming) as it appears to fill crystallographic cleavages and secondary cracks in other minerals (Figure 5d). This mineralogical ensemble together with a negative fold test (Figure 7a) indicate that NRM, at least for the MSM area, is the product of a post-folding remagnetization. The similarity between the obtained directions in the three areas in geographic coordinates and the lack of observed reversals recorded in them support the idea that the areas of Caopas and Nazas N were also (re)magnetized at the same time as the MSM area. All three areas of the San Julián Uplift locality show shallow inclinations (Figure 8) that fit the expected inclination for the Late Jurassic following Torsvik et al., (2012) Global APWP (GAPWaP) adapted for NE México (Koymans et al., 2016; Koymans et al., 2020).

Previous studies have interpreted the MSM anticline as a drape fold formed together with the reverse fault that exhumed the San Julián Uplift during the Eocene (Guerra Roel, 2019; Patiño-Mendez, 2022; Ramírez-Peña & Chávez-Cabello, 2017). However, the inferred age of folding (Eocene) and the post-folding magnetization but with shallow inclinations consistent with a Jurassic origin observed in this locality are incompatible (Figure 8). One option that explains the results could be a quick post-Eocene remagnetization of the studied samples that yielded a biased shallow inclination as a consequence of insufficient PSV averaging. However, this hypothesis is weak since the VGP circular shape and k parameters are both compatible with a correct averaging of the PSV. We think that our data supports a Late Jurassic remagnetization, and that the emplacement of igneous rocks is the best candidate to blame for this remagnetization event. So far, the only Jurassic deformation event described in the studied localities was caused by the emplacement of the plutonic intrusions ~165 Ma, such as the Caopas laccolith. This broadly spaced magmatism includes the emplacement of several intrusions at the Huizachal Valley (Fastovsky et al., 2005; García-Obregón, 2008; Rubio Cisneros, 2012; Rubio Cisneros et al., 2011c), which are blamed for originating the angular unconformities of 10° to 70° between the upper and lower members of La Boca and the one at the contact between La Boca and La Joya formations exposed in the vicinities of intrusions in the Huizachal Valley. We think that the intrusion of the Caopas laccolith might be large enough to generate at least part of the local antiformal structure in the San Julian Uplift. Subsequent cooling of the Caopas laccolith and post-emplacement fluid circulation would be the cause for the remagnetization.

We found eight sites (CHA3 to CHA10) in the Charcas locality that show a large directional consistency with a $k = 52$ at specimen level and $k = 87$ when considering the average of the site means. Such results indicate that either CHA3 to CHA10 sites correspond with a single cooling unit or that all sites were quickly remagnetized at the same time (Figure 6c and 7f Supplementary table ST3). CHA-1 and CHA-2 sites yielded very different directions (Figure 7f). Their differences might be explained either by an extreme PSV event during acquisition (either primarily or during a remagnetization) or by two or three different magnetization events. Unfortunately, our dataset is not large enough to support any of these or an alternative hypothesis.

The rocks sampled at the Huizachal and the Real de Catorce localities show distinctive red color that suggests the presence of pigmentary hematite at first glance. Therefore, we foresaw hematite as a magnetic carrier. Samples from both localities showed a high-temperature component, which was unblocked from 600 °C to the Néel temperature of hematite (700 °C). Samples from the Real

de Catorce locality did not pass the fold test, implying that their magnetization was acquired after folding (Figure 7b). Folding in the area has been dated (Ar-Ar in illite) in the age range between 90 and 70 Ma (Gutiérrez-Navarro et al., 2021). In contrast to San Julián Uplift locality, the inclinations are steeper in Real de Catorce and fit with those expected for Cretaceous and younger rocks (< 140 Ma; Figure 8). The occurrence of double polarity in them indicates that the samples did not remagnetize, or at least not completely, during the Cretaceous superchron that ended ~83 Ma (Ogg, 2020). Hypothesizing a precise age of remagnetization is challenging, but considering the folding age and the documented double polarity, we think that the probable causes are: (1) the initial thrusting of the Mexican Orogen, which in this area started during the Cenomanian (Gutiérrez-Navarro et al., 2021); and (2) the thin-skinned deformation event that lasted until the Late Cretaceous-Early Eocene (Gutiérrez-Navarro et al., 2021). We cannot rule out, however, a later (e.g., Eocene-Oligocene) remagnetization.

The fold test of the Huizachal locality (Supplementary files SF9) is inconclusive, and we do not have another field test to ascertain a relative timing for the magnetization. Nonetheless, we found no reversals registered in the samples from this locality, which spans over 18 million years of the Jurassic (184 – 166 Ma). We think that a secondary magnetization for the locality can better explain our results, as the geomagnetic field during that lapse in the Jurassic was extremely variable (Ogg, 2020). However, the inclinations (Figure 8), fit with a Late Jurassic remagnetization, no younger than 140 Ma, as they did in the San Julian Uplift locality.

5.2. Significance of vertical axis rotations curvature of the Sierra Madre Oriental in North Central México

Our results from the San Julián Uplift and Charcas locality show significant vertical axis rotations with respect to the expected declinations following the GAPWaP of Torsvik et al. (2012; Figure 9). The data of the San Julián uplift locality (MSM 285°/20°, Caopas 271°/17°, and Nazas N 272°/21°) shows > 59° of counterclockwise rotation regardless of the time of the remagnetization (Figures 8 and 9). In contrast, the Charcas data (020°/01°) show a potential clockwise rotation of up to ~30°. The data from Charcas seems to be a single spot-reading evidenced by its high *k* and *K* values. Therefore, we cannot use it to quantify vertical axis rotations. However, the deviation from the GAPWaP is large enough to, at least, suspect that there may be a significant clockwise rotation. The mean direction obtained (346°/42°) in the Real de Catorce locality, does not differ from the expected declination for anytime younger than 160 Ma (Figures 8 and 9).

To our knowledge, the main tectonic events that may explain the observed rotations in NE México are: (1) The Late Jurassic-Early Cretaceous extensional-transtensional (right lateral) event responsible for the opening of the Gulf of México and the translation of the Yucatan block (Martini & Ortega-Gutiérrez, 2018; Pindell & Kennan, 2001) and/or the Nazas back-arc extension (Busby, 2023; Barboza-Gudiño et al., 2021; Dickinson and Lawton, 2001); (2) the Early to Late Cretaceous closure of the Mesozoic Basin of Central México during the Guerrero Superterrane accretion (Centeno-García et al., 2008; Martini et al., 2016; Ortega-Flores et al., 2020) and the subsequent formation of the Mexican Fold and Thrust Belt (Fitz-Díaz et al., 2018 and references therein); (3) the Eocene thick-skinned deformation event (Chávez-Cabello et al., 2005; Guerra-Roel, 2019; Gutiérrez-Navarro et al., 2021; Mauel et al., 2011; Patiño-Mendez, 2022; Ramírez-Peña et al., 2019; Ramírez-Peña & Chávez-Cabello, 2017) and (4) the Basin and Range extension event (Henry and Aranda-Gómez, 1992; Aranda-Gómez & McDowell, 1998; Del Pilar-Martínez et al., 2020; Nieto-Samaniego et al., 1999)

The vertical axis rotations documented in the studied localities seem to correlate with the changes in the trend of the regional structures in each locality (Figure 9) suggesting that the inferred curvature (Figure 9) is an orocline *sensu* Johnston et al. (2013) and Pastor-Galán et al. (2017). The Nazas system in NE Mexico represents the base of the stratigraphic successions exposed at the Sierra Madre Oriental in addition, the curvature and the trend of the Mexican Fold and Thrust Belt in NE México are roughly parallel, a fact that suggests a genetic relationship between them (Figure 2). For these reasons, we term the structure the Sierra Madre Oriental Orocline. Preliminarily, we hypothesize two scenarios for the formation of Sierra Madre Oriental Orocline:

(1) The observed rotations of the Nazas system could have started during the late stages of the opening of the Mesozoic Basin of Central México and were amplified during the development of the Mexican orogen (c.f., Fitz-Díaz et al., 2018). In this case, the curvature of the Nazas system would be a secondary orocline. Whether this feature is of crustal or lithospheric scale is yet to be determined. The curvature drawn by the Late sedimentary cover (the Late Jurassic-Cretaceous rocks resting atop the rocks of the Nazas system; Figure 2) could be either: (a) a primary feature that mimics the original shape of the sedimentary basin, a case similar to the Jura mountains (e.g., Hindle & Burkhard, 1999); or (b) a progressive orocline formed due to the tightening of the preexisting curvature during the development of the Mexican Fold and Thrust Belt (Fitz-Díaz et al., 2018), akin to the Sevier belt in the U.S.A. (e.g., Yonkee & Weil, 2015).

(2) The curvature of the Nazas System in NE México is the result of thin-skinned tectonics developed during Late Cretaceous-Paleogene differential shortening. This phenomenon progressively tightened the curvature and caused opposite rotations on each end of the thrust sheets, which simultaneously affected both the Nazas System and the younger sedimentary cover exposed at the Sierra Madre Oriental.

The existence of an orocline bending or buckling event of such magnitude is an intriguing event that can modify the way the tectonic history of Northeastern Mexico has been interpreted. However, we realize that data is still scarce, incomplete, and scattered. We urge for more and better paleomagnetic and structural data to solve this new and exciting challenge.

6. Conclusions

- We have documented a Late Jurassic, widespread, remagnetization event that affected the Nazas System (i.e., the Nazas Formation and overlying red bed formations) in NE Mexico. The 165 Ma plutonism is the best candidate to trigger that event. We have also found another remagnetization event that we dated as young as 75 Ma.
- Rocks of the Nazas System underwent significant vertical axis rotations, which are congruent with the orientations of regional structures exposed in Mexican Fold and Thrust Belt in Northeastern Mexico.
- The recognized rotations in the Nazas system suggest orocline bending or buckling and not a primary curvature.
- We propose the Sierra Madre Oriental Orocline, which is a $\sim 110^\circ$ curved mountain belt that spans from Durango to San Luis Potosí states in Northeastern Mexico, for a distance of at least 450 km.

Acknowledgments

RGR thanks the CONAHCYT for the support in the form of a doctoral scholarship, and also the funding provided by a Ramón y Cajal Fellow granted to DPG (RYC2019-028244-I) funded by MCIN/AEI/ 10.13039/501100011033 and by the “European Social Fund Investing in your future”. **DPG** is funded by a Grant PID2021-128801NA-I00 funded by MCIN/AEI/10.13039/501100011033, a Ramón y Cajal Fellow RYC2019-028244-I funded by MCIN/AEI/ 10.13039/501100011033 and by the “European Social Fund Investing in your future”, and a Leonardo grant 2022 to researchers and cultural creators (LEO22-2-3010) from the bank BBVA. **GCC** is grateful for the support from PAICYT projects: CT1248-20, CT1626-21, and 36-CAT-2022. **JJAG** gratefully acknowledges PAPIIT UNAM grants IN106820 and IG101523. **GN** thanks the Mexican Science Agency (CONAHCYT) for the support in the form of a MSc scholarship. We appreciate the support of Professor John W. Geissman for the access to the University of Texas paleomagnetism laboratory. Part of the data sets in this paper are the late **Roberto Stanley Molina Garza’s** unpublished work, a friend and a mentor that will be missed.

Data Availability

Raw and interpreted Paleomagnetic data will be uploaded and available in open access servers that respect the FAIR principles such as paleomagnetism.org, MagIC and/or Zenodo when the article is accepted for publication. Data will also be available at reviewer’s request if needed.

Captions

Figure 1. Distribution of the Nazas outcrops in México and the alleged trend of the Sierra Madre Oriental Orocline. Dashed lines in the upper part of the map show the inferred orogen continuity in northern Mexico and southern USA. The Mesozoic Basin of Central México is represented as the Mexican Fold and Thrust Belt (modified from Fitz-Díaz et al., 2018).

Figure 2. (a) Synthetic geological map and regional distribution of the localities sampled in northeastern México. (b) General trend of the inferred curvature of the Sierra Madre Oriental Orocline. Note the presence of the Monterrey salient and the Potosí and Torreón recesses, and the distribution and localization of the Nazas Formation and associated Red beds outcrops. Acronyms: **Cd. V**= Ciudad Victoria; **CHA**= Charcas; **GM**= Gulf of México; **HV**= Huizachal Valley; **Mat**= Matehuala; **Mty**= Monterrey; **PO**= Pacific Ocean; **RC**= Real de Catorce; **SJU**= San Julián Uplift; **Tor**= Torreón; **SMO**: Sierra Madre Oriental; **VJ**= Villa Juárez) (Modified from open-source vector data from INEGI, 2023; and SGM, 2023)

Figure 3. Rock magnetic properties graphs of representative samples. (a) and (b) Gradient Acquisition plots of IRM acquisition curves of the Villa Juárez locality using MAX UnMix

(Maxbauer et al., 2016). Grey dots and the yellow curve represent the smoothed IRM data and modeled coercivity distribution, respectively. Shaded areas represent 95% confidence intervals associated with each component. These plots show mid saturation ($B_{1/2}$) of 1.7 for (a) and 2.85 for (b), magnetite, and hematite phases, respectively. (c) Magnetic susceptibility (Kt) vs. temperature ($^{\circ}\text{C}$) curve for the Villa Juárez locality showing Hematite. (d) Total magnetization vs. temperature ($^{\circ}\text{C}$) for the Caopas intrusive showing hematite and magnetite unblocking temperatures. Red and blue lines represent heating and cooling, respectively. The hysteresis loops were executed in magnetic field increments of 20 mT on an average time of 600 ms and are corrected for paramagnetic-diamagnetic influence. The Nazas North loop (e) shows a high coercivity shape (probably hematite), and the Mina San Miguel Locality shows a thin waist loop that we interpret as magnetite (f).

Figure 4. AMS results represented in an equal area projection for the analyzed sites in the (a) Mina San Miguel, (b) Villa Juárez, (c) Charcas show results of the volcanic rocks of the Nazas Formation, and (d) Caopas intrusive. Larger symbols represent site mean values. Light blue lines represent bedding. Shape parameter T vs Mean magnetic susceptibility K_m , and shape parameter T vs Anisotropy parameter P graphs, show low degree of anisotropy (Supplementary file SF6).

Figure 5. Scanning Electron photomicrographs of representative samples of the Nazas Formation in the localities of Villa Juárez and Mina San Miguel. Photomicrographs of samples collected at the Villa Juárez locality (a and b) show Fe oxides with compositions and texture of primary magnetite, Ti-magnetite, and hematite; the MSM locality Photomicrographs from Mina San Miguel samples show primary magnetite with alteration rims of hematite and hematite that grew in the fractures of an amphibole crystal.

Figure 6. Representative directions of the Nazas Formation are expressed in Zijderveld (1967) diagrams, and fitted great circles. (a) Mina de San Miguel locality, (b) Caopas Intrusive, (c) Charcas, (d) Villa Juárez, (e) Nazas North, and from the Red Beds localities. (f) Real de Catorce, and (g) Huizachal in Geographic Coordinate system. **AF** = Alternating Fields, **TH** = Thermal Demagnetization. **PCA** = Principal Component.

Figure 7. Equal area projections of the direction vectors of all the localities, their overall mean, site average and site average means. Bootstrapped fold test of the Mina de San Miguel and Real de Catorce localities. The projections show behavior of paleomagnetic directions during unfolding from 0% (geographic) to 100% (Tectonic). (a) Mina San Miguel locality with Foldtest. (b) Real de Catorce **Geo** = geographic; **Tec** = Tectonic; **VGP** = Virtual Geomagnetic Poles (locality mean parameters see Table 1)

Figure 8. Observed declinations and inclinations from sampled localities and Global Apparent Wander Path of the study area for North America (Torsvik et al., 2012) calculated with Paleomagnetism.org (Koymans et al., 2016, 2020). All localities are represented in geographic

coordinates except Charcas. Acronyms: **CHA-GEO** = Charcas in Geographic Coordinates; **CHA-TC**= Charcas in Tectonic Coordinates; **HUI** = Huizachal Valley; **RC** = Real de Catorce; **SJU** = San Julián Uplift.

Figure 9. Vertical axis rotations and structural trend of the area (**SJU** = San Julián Uplift; **HUI** = Huizachal Valley; **RC** = Real de Catorce; **CHA**= Charcas). The yellow fields represent the expected declinations from 200 Ma to present day (Torsvik et al., 2012). Direction means (observed declinations) within the expected direction range (yellow) are considered not rotated. Δ Dec: Calculated error for direction mean.

References

Abrajevitch, A. V., Ali, J. R., Aitchison, J. C., Badengzhu, Davis, A. M., Liu, J., & Ziabrev, S. V. (2005). Neotethys and the India–Asia collision: Insights from a palaeomagnetic study of the Dazhuqu ophiolite, southern Tibet. *Earth and Planetary Science Letters*, 233(1), 87–102. <https://doi.org/10.1016/j.epsl.2005.02.003>

Anderson, T. H., McKee, J. W., & Jones, N. W. (1991). A northwest trending, Jurassic Fold Nappe, northernmost Zacatecas, Mexico. *Tectonics*, 10(2), 383–401. <https://doi.org/10.1029/90TC02419>

Anderson, T. H., & Schmidt, V. A. (1983). The evolution of Middle America and the Gulf of Mexico–Caribbean Sea region during Mesozoic time. *Geological Society of America Bulletin*, 94(8), 941. [https://doi.org/10.1130/0016-7606\(1983\)94<941:TEOMAA>2.0.CO;2](https://doi.org/10.1130/0016-7606(1983)94<941:TEOMAA>2.0.CO;2)

Anderson, T. H., Silver, L. T., Nourse, J. A., McKee, J. W., & Steiner, M. B. (2005). The Mojave–Sonora megashear–Field and analytical studies leading to the conception and evolution of the hypothesis. *SPECIAL PAPERS-GEOLOGICAL SOCIETY OF AMERICA*, 393, 1.

Aranda-Gómez, J. J., & McDowell, F. W. (1998). Paleogene Extension in the Southern Basin and Range Province of Mexico: Syndepositional Tilting of Eocene Red Beds and Oligocene Volcanic Rocks in the Guanajuato Mining District. *International Geology Review*, 40(2), 116–134. <https://doi.org/10.1080/00206819809465201>

Bagheri, S. and Gol, S.D., 2020. The eastern iranian orocline. *Earth-Science Reviews*, 210, p.103322. ISSN 0012-8252. <https://doi.org/10.1016/j.earscirev.2020.103322>.

820 Barboza-Gudiño, J. R., Hoppe, M., Gómez-Anguiano, M., & Martínez-Macías, P. (2004).
821 Aportaciones para la interpretación estratigráfica y estructural de la porción noroccidental de la
822 Sierra de Catorce, San Luis Potosí, México. *Revista Mexicana de Ciencias Geológicas*, ISSN
823 1026-8774, Vol. 21, No. 3, 2004, 299-319, 21.

824 Barboza-Gudiño, J. R., Molina-Garza, R. S., & Lawton, T. F. (2012). Sierra de Catorce: Remnants
825 of the ancient western equatorial margin of Pangea in central Mexico. In J. J. Aranda-Gómez, G.
826 Tolson, & R. S. Molina-Garza (Eds.), *The Southern Cordillera and Beyond* (Vol. 25, p. 0).
827 Geological Society of America. [https://doi.org/10.1130/2012.0025\(01\)](https://doi.org/10.1130/2012.0025(01))

828 Barboza-Gudiño, J. R., Ocampo-Díaz, Y. Z. E., Zavala-Monsiváis, A., & López-Doncel, R. A.
829 (2014). Procedencia como herramienta para la subdivisión estratigráfica del Mesozoico temprano
830 en el noreste de México. *Revista Mexicana de Ciencias Geológicas*, 31, 303–324. Scopus.

831 Barboza-Gudiño, J. R., Orozco-Esquivel, M. T., Gómez-Anguiano, M., & Zavala-Monsiváis, A.
832 (2008). The Early Mesozoic volcanic arc of western North America in northeastern Mexico.
833 *Journal of South American Earth Sciences*, 25(1), 49–63.
834 <https://doi.org/10.1016/j.jsames.2007.08.003>

835 Barboza-Gudiño, J. R., Zavala-Monsiváis, A., Castellanos-Rodríguez, V., Jaime-Rodríguez, D., &
836 Almaraz-Martínez, C. (2021). Subduction-related Jurassic volcanism in the Mesa Central province
837 and contemporary Gulf of Mexico opening. *Journal of South American Earth Sciences*, 108,
838 102961. <https://doi.org/10.1016/j.jsames.2020.102961>

839 Barboza-Gudiño, J. R., Zavala-Monsiváis, A., Venegas-Rodríguez, G., & Barajas-Nigoche, L. D.
840 (2010). Late Triassic stratigraphy and facies from northeastern Mexico: Tectonic setting and
841 provenance. *Geosphere*, 6(5), 621–640. Scopus. <https://doi.org/10.1130/GES00545.1>

842 Bartolini, C., Lang, H., & Spell, T. (2003). Geochronology, Geochemistry, and Tectonic Setting
843 of the Mesozoic Nazas Arc in North-Central Mexico, and its Continuation to Northern South
844 America. 427–461.

845 Bartolini, C., Wilson, J. L., & Lawton, T. F. (1999). Mesozoic Sedimentary and Tectonic History
846 of North-central Mexico. Geological Society of America.

847 Busby, C. J. (2023). Guerrero-Alisitos-Vizcaino superterrane of western Mexico and its ties to the
848 Mexican continental margin (Gondwana and SW Laurentia). In S. J. Whitmeyer, M. L. Williams,
849 D. A. Kellett, & B. Tikoff (Eds.), *Laurentia: Turning Points in the Evolution of a Continent* (Vol.
850 220, p. 0). Geological Society of America. [https://doi.org/10.1130/2022.1220\(34\)](https://doi.org/10.1130/2022.1220(34))

851 Busby, C. J., & Centeno-García, E. (2022). The “Nazas Arc” is a continental rift province:
852 Implications for Mesozoic tectonic reconstructions of the southwest Cordillera, U.S. and Mexico.
853 *Geosphere*, 18(2), 647–669. <https://doi.org/10.1130/GES02443.1>

854 Butler, R. (1992). *Paleomagnetism: Magnetic Domains to Geologic Terranes*. Blackwell Science
855 Inc.

856 Campa-Uranga, M. F., García-Díaz, J. L., & Iriondo, A. (2004). El arco sedimentario del Jurásico
857 Medio (Grupo Tecocoyunca y Las Lluvias) de Olinalá. *GEOS Unión Geofísica Mexicana*, 24(2),
858 174.

859 Carey, S. W. (1955). The orocline concept in geotectonics-Part I. *Papers and Proceedings of the*
860 *Royal Society of Tasmania*, 89, 255–288.

861 Centeno-García, E., Anderson, T. H., Nourse, J. A., McKee, J. W., & Steiner, M. B. (2005).
862 Review of upper Paleozoic and lower Mesozoic stratigraphy and depositional environments,
863 central and west Mexico: Constraints on terrane analysis and paleogeography. *SPECIAL*
864 *PAPERS-GEOLOGICAL SOCIETY OF AMERICA*, 393, 233.

865 Centeno-García, E., Guerrero-Suastegui, M., & Talavera-Mendoza, O. (2008). The Guerrero
866 Composite Terrane of western Mexico: Collision and subsequent rifting in a supra-subduction
867 zone. In A. E. Draut, Peter. D. Clift, & D. W. Scholl (Eds.), *Formation and Applications of the*
868 *Sedimentary Record in Arc Collision Zones* (Vol. 436, p. 0). Geological Society of America.
869 [https://doi.org/10.1130/2008.2436\(13\)](https://doi.org/10.1130/2008.2436(13))

870 Chadima, M., & Hrouda, F. (2009). *Cureval 8.0: Thermomagnetic curve browser for windows*.
871 Agico. Inc, Brno.

872 Chávez-Cabello, G., Aranda-Gómez, J. J., Molina-Garza, R. S., Cossío-Torres, T., Arvizu-
873 Gutiérrez, I. R., & González-Naranjo, G. A. (2005). La falla San Marcos: Una estructura jurásica

874 de basamento multi reactivada del noreste de México. Boletín de La Sociedad Geológica Mexicana,
875 57(1), 27–52.

876 Chávez-Cabello, G., Cossío-Torres, T., & Peterson-Rodríguez, R. H. (2004). Change of the
877 maximum principal stress during the Laramide Orogeny in the Monterrey salient, northeast
878 México. *Orogenic Curvature: Integrating Paleomagnetic and Structural Analyses*: Geological
879 Society of America Special Paper, 383, 145–159.

880 Clemons, R. E., & McLeroy, D. F. (1965). Resumen de la geología de la Hoja Torreón, 13R-1 (1):
881 Universidad Nacional Autónoma de México. Instituto de Geología, Carta Geológica de México,
882 Serie, 1(100,000).

883 De Boer, C. B., & Dekkers, M. J. (1998). Thermomagnetic behavior of hematite and goethite as a
884 function of grain size in various non-saturating magnetic fields. *Geophysical Journal International*,
885 133(3), 541–552.

886 DeCelles, P. G., Ducea, M. N., Kapp, P., & Zandt, G. (2009). Cyclicity in Cordilleran orogenic
887 systems. *Nature Geoscience*, 2(4), Article 4. <https://doi.org/10.1038/ngeo469>

888 Deenen, M. H., Langereis, C. G., van Hinsbergen, D. J., & Biggin, A. J. (2011). Geomagnetic
889 secular variation and the statistics of palaeomagnetic directions. *Geophysical Journal International*,
890 186(2), 509–520.

891 Del Pilar-Martínez, A., Nieto-Samaniego, A. F., & Alaniz-Alvarez, S. A. (2020). Development of
892 a brittle triaxial deformation zone in the upper crust: The case of the southern Mesa Central of
893 Mexico. *Tectonics*, 39(11), e2020TC006166.

894 Dickinson, W. R., & Lawton, T. F. (2001). Carboniferous to Cretaceous assembly and
895 fragmentation of Mexico. *Geological Society of America Bulletin*, 113(9), 1142–1160.

896 Dunlop, D. J., & Özdemir, Ö. (1997). *Rock magnetism: Fundamentals and frontiers*. Cambridge
897 University Press.

898 Eguluz, S., Aranda, M., & Marrett, R. (2000). Tectónica de la Sierra Madre Oriental, México.
899 Boletín de La Sociedad Geológica Mexicana, 53(1), 1–26.

900 Eichelberger, N., & McQuarrie, N. (2015). Kinematic reconstruction of the Bolivian orocline.
 901 *Geosphere*, 11(2), 445–462. <https://doi.org/10.1130/GES01064.1>

902 Eldredge, S., Bachtadse, V., & Van der Voo, R. (1985). Paleomagnetism and the orocline
 903 hypothesis. *Tectonophysics*, 119(1–4), 153–179.

904 Fastovsky, D. E., Hermes, O. D., Strater, N. H., Bowring, S. A., Clark, J. M., Montellano, M., &
 905 Rene, H. R. (2005). Pre–Late Jurassic, fossil-bearing volcanic and sedimentary red beds of
 906 Huizachal Canyon, Tamaulipas, Mexico.

907 Fisher, R. A. (1953). Dispersion on a sphere. *Proceedings of the Royal Society of London. Series*
 908 *A. Mathematical and Physical Sciences*, 217(1130), 295–305.

909 Fitz-Díaz, E., Lawton, T. F., Juárez-Arriaga, E., & Chávez-Cabello, G. (2018). The Cretaceous-
 910 Paleogene Mexican orogen: Structure, basin development, magmatism and tectonics. *Earth-*
 911 *Science Reviews*, 183, 56–84.

912 Flinn, D. (1962). On folding during three-dimensional progressive deformation. *Quarterly Journal*
 913 *of the Geological Society*, 118(1–4), 385–428.

914 García-Obregón, R. (2008). Cartografía geológica y petrología del vulcanismo mesozoico en el
 915 Valle de Huizachal, Tamaulipas. [Tesis de Licenciatura]. Universidad Autónoma de Nuevo León.

916 Gerritsen, D., Vaes, B., & van Hinsbergen, D. J. (2022). Influence of data filters on the position
 917 and precision of paleomagnetic poles: What is the optimal sampling strategy? *Geochemistry,*
 918 *Geophysics, Geosystems*, 23(4), e2021GC010269.

919 Godínez-Urban, A., Lawton, T. F., Molina Garza, R. S., Iriondo, A., Weber, B., & López-Martínez,
 920 M. (2011). Jurassic volcanic and sedimentary rocks of the La Silla and Todos Santos Formations,
 921 Chiapas: Record of Nazas arc magmatism and rift-basin formation prior to opening of the Gulf of
 922 Mexico. *Geosphere*, 7(1), 121–144.

923 Goldhammer, R. K. (1999). Mesozoic sequence stratigraphy and paleogeographic evolution of
 924 northeast Mexico.

925 Gómez Torres, R. C. (2022). Geoquímica en roca total y zircones de rocas Mágmaticas del
926 Jurásico-Paleógeno en el Bloque de San Julián, Zacatecas, México. [Masters Tesis]. Universidad
927 Autónoma de Nuevo León. p. 139.

928 González-León, C. M., Vázquez-Salazar, M., Navarro, T. S., Solari, L. A., Nourse, J. A., Del Rio-
929 Salas, R., Lozano-Santacruz, R., Arvizu, O. P., & Valenzuela Chacón, J. C. (2021). Geology and
930 geochronology of the Jurassic magmatic arc in the Magdalena quadrangle, north-central Sonora,
931 Mexico. *Journal of South American Earth Sciences*, 108, 103055.
932 <https://doi.org/10.1016/j.jsames.2020.103055>

933 Grajales-Nishimura, J. M., Terrell, D. J., & Damon, P. E. (1992). Evidencias de la prolongación
934 del arco magmático cordillerano del Triásico Tardío-Jurásico en Chihuahua. Durango y Coahuila:
935 *Boletín de La Asociación Mexicana de Geólogos Petroleros*, 42(2), 1–18.

936 Gray, G. G., & Lawton, T. F. (2011). New constraints on timing of Hidalgoan (Laramide)
937 deformation in the Parras and La Popa basins, NE Mexico. *Boletín de La Sociedad Geológica*
938 *Mexicana*, 63(2), 333–343.

939 Gubbins, D., & Herrero-Bervera, E. (2007). *Encyclopedia of Geomagnetism and Paleomagnetism*.
940 Springer Science & Business Media.

941 Guerra Roel, R. (2019). Análisis estructural de la zona norte del bloque de San Julián, Zacatecas
942 México [Masters, Universidad Autónoma de Nuevo León]. <http://eprints.uanl.mx/18367/>

943 Gutiérrez-Alonso, G., Fernández-Suárez, J., & Weil, A. B. (2004). Orocline triggered lithospheric
944 delamination. In *Special Paper 383: Orogenic curvature: Integrating paleomagnetic and structural*
945 *analyses (Vol. 383, pp. 121–130)*. Geological Society of America. [https://doi.org/10.1130/0-8137-](https://doi.org/10.1130/0-8137-2383-3(2004)383[121:OTLD]2.0.CO;2)
946 [2383-3\(2004\)383\[121:OTLD\]2.0.CO;2](https://doi.org/10.1130/0-8137-2383-3(2004)383[121:OTLD]2.0.CO;2)

947 Gutiérrez-Alonso, G., Fernández-Suárez, J., Weil, A. B., Brendan Murphy, J., Damian Nance, R.,
948 Corfú, F., & Johnston, S. T. (2008). Self-subduction of the Pangaeon global plate. *Nature*
949 *Geoscience*, 1(8), Article 8. <https://doi.org/10.1038/ngeo250>

950 Gutiérrez-Navarro, R., Fitz Diaz, E., Barboza-Gudiño, J., & Stockli, D. (2021). Shortening and
951 exhumation of Sierra de Catorce in northeastern Mexico, in light of $^{40}\text{Ar}/^{39}\text{Ar}$ illite dating and

952 U–Th/He zircon thermochronology. *Journal of South American Earth Sciences*, 111, 103334.
 953 <https://doi.org/10.1016/j.jsames.2021.103334>

954 Henry, C. D., & Aranda-Gómez, J. J. (1992). The real southern Basin and Range: Mid- to Late
 955 Cenozoic extension in Mexico. *Geology*, 20(8), 701–704. [https://doi.org/10.1130/0091-](https://doi.org/10.1130/0091-7613(1992)020<0701:TRSBAR>2.3.CO;2)
 956 [7613\(1992\)020<0701:TRSBAR>2.3.CO;2](https://doi.org/10.1130/0091-7613(1992)020<0701:TRSBAR>2.3.CO;2)

957 Hernández-Romano, U., Aguilera-Franco, N., Martínez-Medrano, M., & Barceló-Duarte, J. (1997).
 958 Guerrero-Morelos Platform drowning at the Cenomanian–Turonian boundary, Huitziltepec area,
 959 Guerrero State, southern Mexico. *Cretaceous Research*, 18(5), 661–686.

960 Hindle, D., & Burkhard, M. (1999). Strain, displacement and rotation associated with the
 961 formation of curvature in fold belts; the example of the Jura arc. *Journal of Structural Geology*,
 962 21(8), 1089–1101. [https://doi.org/10.1016/S0191-8141\(99\)00021-8](https://doi.org/10.1016/S0191-8141(99)00021-8)

963 Imlay, R. W., Cepeda, E., Alvarez, M., & Diaz, T. (1948). Stratigraphic relations of certain Jurassic
 964 formations in eastern Mexico. *AAPG Bulletin*, 32(9), 1750–1761.

965 INEGI. (2023). Biblioteca digital de Mapas. Instituto Nacional de Estadística y Geografía. INEGI.
 966 <https://www.inegi.org.mx/app/mapas/>

967 Jelinek, V. (1981). Characterization of the magnetic fabric of rocks. *Tectonophysics*, 79(3–4),
 968 T63–T67.

969 Jiménez, G., Speranza, F., Faccenna, C., Bayona, G., & Mora, A. (2014). Paleomagnetism and
 970 magnetic fabric of the Eastern Cordillera of Colombia: Evidence for oblique convergence and
 971 nonrotational reactivation of a Mesozoic intracontinental rift. *Tectonics*, 33(11), 2233–2260.
 972 <https://doi.org/10.1002/2014TC003532>

973 Johnston, S. T. (2001). The Great Alaskan Terrane Wreck: Reconciliation of paleomagnetic and
 974 geological data in the northern Cordillera. *Earth and Planetary Science Letters*, 193(3), 259–272.
 975 [https://doi.org/10.1016/S0012-821X\(01\)00516-7](https://doi.org/10.1016/S0012-821X(01)00516-7)

976 Johnston, S. T., Weil, A. B., & Gutiérrez-Alonso, G. (2013). Oroclines: Thick and thin. *GSA*
 977 *Bulletin*, 125(5–6), 643–663. <https://doi.org/10.1130/B30765.1>

978 Jones, N. W., McKee, J. W., Anderson, T. H., & Silver, L. T. (1995). Jurassic volcanic rocks in
979 northeastern Mexico: A possible remnant of a Cordilleran magmatic arc. In C. Jacques-Ayala, C.
980 M. González-Léon, & J. Roldán-Quintana (Eds.), *Studies on the Mesozoic of Sonora and adjacent*
981 *areas* (Vol. 301, p. 0). Geological Society of America. <https://doi.org/10.1130/0-8137-2301-9.179>

982 Kirschvink, J. L. (1980). The least-squares line and plane and the analysis of palaeomagnetic data.
983 *Geophysical Journal International*, 62(3), 699–718.

984 Kollmeier, J. M., van der Pluijm, B. A., & Van der Voo, R. (2000). Analysis of Variscan dynamics;
985 early bending of the Cantabria–Asturias Arc, northern Spain. *Earth and Planetary Science Letters*,
986 181(1), 203–216. [https://doi.org/10.1016/S0012-821X\(00\)00203-X](https://doi.org/10.1016/S0012-821X(00)00203-X)

987 Koymans, M. R., Langereis, C. G., Pastor-Galán, D., & van Hinsbergen, D. J. (2016).
988 Paleomagnetism. org: An online multi-platform open-source environment for paleomagnetic data
989 analysis. Elsevier.

990 Koymans, M. R., van Hinsbergen, D. J. J., Pastor-Galán, D., Vaes, B., & Langereis, C. G. (2020).
991 Towards FAIR paleomagnetic data management through Paleomagnetism. Org 2.0. *Geochemistry,*
992 *Geophysics, Geosystems*, 21(2), e2019GC008838.

993 Kruiver, P. P., Dekkers, M. J., & Heslop, D. (2001). Quantification of magnetic coercivity
994 components by the analysis of acquisition curves of isothermal remanent magnetisation. *Earth and*
995 *Planetary Science Letters*, 189(3–4), 269–276.

996 Lawton, T. F., & Molina Garza, R. S. (2014). U-Pb geochronology of the type Nazas Formation
997 and superjacent strata, northeastern Durango, Mexico: Implications of a Jurassic age for
998 continental-arc magmatism in north-central Mexico. *GSA Bulletin*, 126(9–10), 1181–1199.
999 <https://doi.org/10.1130/B30827.1>

1000 Li, P., Rosenbaum, G., & Donchak, P. J. (2012). Structural evolution of the Texas Orocline, eastern
1001 Australia. *Gondwana Research*, 22(1), 279–289.

1002 López-Infanzón, M. L. (1986). Estudio Petrogenético De Las Rocas Igneas En Las Formaciones
1003 Huizachal Y Nazas. *Boletín de La Sociedad Geológica Mexicana*, 47(2), 1–41.

1004 Maffione, M., Speranza, F., Faccenna, C., & Rossello, E. (2010). Paleomagnetic evidence for a
1005 pre-early Eocene (~50Ma) bending of the Patagonian orocline (Tierra del Fuego, Argentina):
1006 Paleogeographic and tectonic implications. *Earth and Planetary Science Letters*, 289(1), 273–286.
1007 <https://doi.org/10.1016/j.epsl.2009.11.015>

1008 Marshak, S. (1988). Kinematics of orocline and arc formation in thin-skinned orogens. *Tectonics*,
1009 7(1), 73–86. <https://doi.org/10.1029/TC007i001p00073>

1010 Marshak, S. (2004). Salients, Recesses, Arcs, Oroclines, and Syntaxes—A Review of Ideas
1011 Concerning the Formation of Map-view Curves in Fold-thrust Belts. In K. R. McClay (Ed.), *Thrust*
1012 *Tectonics and Hydrocarbon Systems* (Vol. 82, p. 0). American Association of Petroleum
1013 Geologists. <https://doi.org/10.1306/M82813C9>

1014 Martini, M., & Ortega-Gutiérrez, F. (2018). Tectono-stratigraphic evolution of eastern Mexico
1015 during the break-up of Pangea: A review. *Earth-Science Reviews*, 183, 38–55.
1016 <https://doi.org/10.1016/j.earscirev.2016.06.013>

1017 Martini, M., Solari, L., & Camprubí, A. (2013). Kinematics of the Guerrero terrane accretion in
1018 the Sierra de Guanajuato, central Mexico: New insights for the structural evolution of arc–
1019 continent collisional zones. *International Geology Review*, 55(5), 574–589.
1020 <https://doi.org/10.1080/00206814.2012.729361>

1021 Martini, M., Solé, J., Garduño-Martínez, D. E., Puig, T. P., & Omaña, L. (2016). Evidence for two
1022 Cretaceous superposed orogenic belts in central Mexico based on paleontologic and K-Ar
1023 geochronologic data from the Sierra de los Cuarcos. *Geosphere*, 12(4), 1257–1270.
1024 <https://doi.org/10.1130/GES01275.1>

1025 Mauel, D. J., Lawton, T. F., González-León, C., Iriondo, A., & Amato, J. M. (2011). Stratigraphy
1026 and age of Upper Jurassic strata in north-central Sonora, Mexico: Southwestern Laurentian record
1027 of crustal extension and tectonic transition. *Geosphere*, 7(2), 390–414.
1028 <https://doi.org/10.1130/GES00600.1>

1029 Maxbauer, D. P., Feinberg, J. M., & Fox, D. L. (2016). MAX UnMix: A web application for
1030 unmixing magnetic coercivity distributions. *Computers & Geosciences*, 95, 140–145.
1031 <https://doi.org/10.1016/j.cageo.2016.07.009>

1032 McElhinny, M. W., & McFadden, P. L. (1999). *Paleomagnetism: Continents and Oceans*. Elsevier.

1033 McFadden, P. L., & McElhinny, M. W. (1988). The combined analysis of remagnetization circles
 1034 and direct observations in palaeomagnetism. *Earth and Planetary Science Letters*, 87(1), 161–172.
 1035 [https://doi.org/10.1016/0012-821X\(88\)90072-6](https://doi.org/10.1016/0012-821X(88)90072-6)

1036 Meert, J. G., Pivarunas, A. F., Evans, D. A. D., Pisarevsky, S. A., Pesonen, L. J., Li, Z.-X., Elming,
 1037 S.-Å., Miller, S. R., Zhang, S., & Salminen, J. M. (2020). The magnificent seven: A proposal for
 1038 modest revision of the Van der Voo (1990) quality index. *Tectonophysics*, 790, 228549.
 1039 <https://doi.org/10.1016/j.tecto.2020.228549>

1040 Mixon, R. B., Murray, G. E., & Teodoro, D. G. (1959). Age and Correlation of Huizachal Group
 1041 (Mesozoic), State of Tamaulipas, Mexico1: ADDENDUM. *AAPG Bulletin*, 43(4), 757–771.
 1042 <https://doi.org/10.1306/0BDA5ED3-16BD-11D7-8645000102C1865D>

1043 Molina-Garza, R. S., & Iriondo, A. (2005). La Megacizalla Mojave-Sonora: La hipótesis, la
 1044 controversia y el estado actual de conocimiento. *Boletín de la Sociedad Geológica Mexicana*, 57(1),
 1045 1–26. <https://doi.org/10.18268/bsgm2005v57n1a1>

1046 Molina-Garza, R. S., Pindell, J., & Montaña Cortés, P. C. (2020). Slab flattening and tractional
 1047 coupling drove Neogene clockwise rotation of Chiapas Massif, Mexico: Paleomagnetism of the
 1048 Eocene El Bosque Formation. *Journal of South American Earth Sciences*, 104, 102932.
 1049 <https://doi.org/10.1016/j.jsames.2020.102932>

1050 Montes, C., Bayona, G., Cardona, A., Buchs, D. M., Silva, C. A., Morón, S., Hoyos, N., Ramírez,
 1051 D. A., Jaramillo, C. A., & Valencia, V. (2012). Arc-continent collision and orocline formation:
 1052 Closing of the Central American seaway. *Journal of Geophysical Research: Solid Earth*, 117(B4).
 1053 <https://doi.org/10.1029/2011JB008959>

1054 Nemkin, S. R., Chávez-Cabello, G., Fitz-Díaz, E., van der Pluijm, B., & Van der Voo, R. (2019).
 1055 Concurrence of folding and remagnetization events in the Monterrey Salient (NE Mexico).
 1056 *Tectonophysics*, 760, 58–68. <https://doi.org/10.1016/j.tecto.2017.12.002>

1057 Nieto-Samaniego, Á. F., Ferrari, L., Alaniz-Alvarez, S. A., Labarthe-Hernández, G., & Rosas-
 1058 Elguera, J. (1999). Variation of Cenozoic extension and volcanism across the southern Sierra

1059 Madre Occidental volcanic province, Mexico. *Geological Society of America Bulletin*, 111(3),
1060 347–363.

1061 Ocampo-Díaz, Y. Z. E., Pinzon-Sotelo, M. P., Chávez-Cabello, G., Ramírez-Díaz, A., Martínez-
1062 Paco, M., Velasco-Tapia, F., Guerrero-Suastegui, M., Barboza-Gudiño, J. R., Ocampo-Díaz, Y. Z.
1063 E., Pinzon-Sotelo, M. P., Chávez-Cabello, G., Ramírez-Díaz, A., Martínez-Paco, M., Velasco-
1064 Tapia, F., Guerrero-Suastegui, M., & Barboza-Gudiño, J. R. (2016). Propuesta nomenclatural y
1065 análisis de procedencia de la Formación Concepción del Oro (antes Formación Caracol):
1066 Implicaciones sobre la evolución tectónica del sur de Norteamérica durante el Cretácico Tardío.
1067 *Revista mexicana de ciencias geológicas*, 33(1), 3–33.

1068 Ogg, J. G. (2020). Chapter 5—Geomagnetic Polarity Time Scale. In F. M. Gradstein, J. G. Ogg,
1069 M. D. Schmitz, & G. M. Ogg (Eds.), *Geologic Time Scale 2020* (pp. 159–192). Elsevier.
1070 <https://doi.org/10.1016/B978-0-12-824360-2.00005-X>

1071 O'Reilly, W. (1984). Applications of rock and mineral magnetism. In W. O'Reilly (Ed.), *Rock and*
1072 *Mineral Magnetism* (pp. 194–212). Springer US. https://doi.org/10.1007/978-1-4684-8468-7_9

1073 Ortega-Flores, B., Solari, L. A., Martini, M., & Ortega-Obregón, C. (2020). The Guerrero terrane,
1074 a para-autochthonous block on the paleo-Pacific continental margin of North America: Evidence
1075 from zircon U-Pb dating and Hf isotopes. [https://doi.org/10.1130/2020.2546\(08\)](https://doi.org/10.1130/2020.2546(08))

1076 Padilla y Sánchez, R. J. (1985). Las estructuras de la Curvatura de Monterrey, estados de Coahuila,
1077 Nuevo León, Zacatecas y San Luis Potosí. *Revista Mexicana de Ciencias Geológicas*, 6(1), 1–20.

1078 Pantoja-Alor, J. (1972). Datos geológicos y estratigráficos de la Formación Nazas (memoria), II
1079 Convención Nacional. Mazatlán, Sinaloa, Sociedad Geológica Mexicana, 25–31.

1080 Parés, J. M. (2015). Sixty years of anisotropy of magnetic susceptibility in deformed sedimentary
1081 rocks. *Frontiers in Earth Science*, 3. <https://www.frontiersin.org/articles/10.3389/feart.2015.00004>

1082 Parolari, M., Martini, M., Gómez-Tuena, A., Ortega-Gutiérrez, F., Errázuriz-Henao, C., &
1083 Cavazos-Tovar, J. G. (2022). The petrogenesis of Early–Middle Jurassic magmatism in southern
1084 and central Mexico and its role during the break-up of Western Pangaea. *Geological Magazine*,
1085 159(6), 873–892. <https://doi.org/10.1017/S0016756822000061>

1086 Pastor-Galán, D. (2022). From supercontinent to superplate: Late Paleozoic Pangea's inner
 1087 deformation suggests it was a short-lived superplate. *Earth-Science Reviews*, 226, 103918.
 1088 <https://doi.org/10.1016/j.earscirev.2022.103918>

1089 Pastor-Galán, D., Groenewegen, T., Brouwer, D., Krijgsman, W., & Dekkers, M. J. (2015). One
 1090 or two oroclinal in the Variscan orogen of Iberia? Implications for Pangea amalgamation. *Geology*,
 1091 43(6), 527–530. <https://doi.org/10.1130/G36701.1>

1092 Pastor-Galán, D., Gutiérrez-Alonso, G., Dekkers, M. J., & Langereis, C. G. (2017).
 1093 Paleomagnetism in Extremadura (Central Iberian zone, Spain) Paleozoic rocks: Extensive
 1094 remagnetizations and further constraints on the extent of the Cantabrian orocline. *Journal of*
 1095 *Iberian Geology*, 43(4), 583–600. <https://doi.org/10.1007/s41513-017-0039-x>

1096 Pastor-Galán, D., Gutiérrez-Alonso, G., & Weil, A. B. (2011). Orocline timing through joint
 1097 analysis: Insights from the Ibero-Armorican Arc. *Tectonophysics*, 507(1), 31–46.
 1098 <https://doi.org/10.1016/j.tecto.2011.05.005>

1099 Pastor-Galán, D., Gutiérrez-Alonso, G., & Weil, A. B. (2020). The enigmatic curvature of Central
 1100 Iberia and its puzzling kinematics. *Solid Earth*, 11(4), 1247–1273. [https://doi.org/10.5194/se-11-](https://doi.org/10.5194/se-11-1247-2020)
 1101 1247-2020

1102 Pastor-Galán, D., Gutiérrez-Alonso, G., Zulauf, G., & Zanella, F. (2012). Analogue modeling of
 1103 lithospheric-scale orocline buckling: Constraints on the evolution of the Iberian-Armorican Arc.
 1104 *GSA Bulletin*, 124(7–8), 1293–1309. <https://doi.org/10.1130/B30640.1>

1105 Pastor-Galán, D., Martín-Merino, G., & Corrochano, D. (2014). Timing and structural evolution
 1106 in the limb of an orocline: The Pisuerga–Carrión Unit (southern limb of the Cantabrian Orocline,
 1107 NW Spain). *Tectonophysics*, 622, 110–121. <https://doi.org/10.1016/j.tecto.2014.03.004>

1108 Pastor-Galán, D., Pueyo, E. L., Diederer, M., García-Lasanta, C., & Langereis, C. G. (2018). Late
 1109 Paleozoic Iberian Orocline(s) and the Missing Shortening in the Core of Pangea. *Paleomagnetism*
 1110 *From the Iberian Range*. *Tectonics*, 37(10), 3877–3892. <https://doi.org/10.1029/2018TC004978>

1111 Pastor-Galán, D., Spencer, C. J., Furukawa, T., & Tsujimori, T. (2021). Evidence for crustal
 1112 removal, tectonic erosion and flare-ups from the Japanese evolving forearc sediment provenance.
 1113 *Earth and Planetary Science Letters*, 564, 116893. <https://doi.org/10.1016/j.epsl.2021.116893>

1114 Patiño-Mendez, G. (2022). Analisis de la Fabrica Magnética en lavas plegadas de la Formación
 1115 Nazas, Bloque de San Julian, Zacatecas, México. [Batchelor tesis]. Universidad Autónoma de
 1116 Nuevo León.

1117 Pindell, J., & Kennan, L. (2001). Kinematic Evolution of the Gulf of Mexico and Caribbean. In R.
 1118 H. Fillon, N. C. Rosen, P. Weimer, A. Lowrie, H. Pettingill, R. L. Phair, H. H. Roberts, & H. H.
 1119 van Hoom (Eds.), *Petroleum Systems of Deep-Water Basins—Global and Gulf of Mexico*
 1120 *Experience* (Vol. 21, p. 0). SEPM Society for Sedimentary Geology.
 1121 <https://doi.org/10.5724/gcs.01.21.0193>

1122 Ramírez-Peña, C. F. (2017). Análisis de la deformación progresiva en la zona sur del sector
 1123 transversal de Parras y la Saliente de Monterrey, México. PhD. Tesis, Universidad Autónoma de
 1124 Nuevo León, Facultad de Ciencias de la Tierra.

1125 Ramírez-Peña, C. F., & Chávez-Cabello, G. (2017). Age and evolution of thin-skinned
 1126 deformation in Zacatecas, Mexico: Sevier orogeny evidence in the Mexican Fold-Thrust Belt.
 1127 *Journal of South American Earth Sciences*, 76, 101–114.
 1128 <https://doi.org/10.1016/j.jsames.2017.01.007>

1129 Ramírez-Peña, C. F., Chávez-Cabello, G., Fitz-Díaz, E., Aranda-Gómez, J. J., & Valdés, R. S.
 1130 (2019). Uplift and syn-orogenic magmatism in the Concepción del Oro Block: A thick-skinned
 1131 (Laramide style?) contractional structure in the Mexican Fold-Thrust Belt. *Journal of South*
 1132 *American Earth Sciences*, 93, 242–252. <https://doi.org/10.1016/j.jsames.2019.04.012>

1133 Rezaeian, M., Kuijper, C. B., van der Boon, A., Pastor-Galán, D., Cotton, L. J., Langereis, C. G.,
 1134 & Krijgsman, W. (2020). Post-Eocene coupled oroclinal in the Talesh (NW Iran): Paleomagnetic
 1135 constraints. *Tectonophysics*, 786, 228459. <https://doi.org/10.1016/j.tecto.2020.228459>

1136 Rogers, C. L., De Cserna, Z., & VLOTEN, V. (1963). Plutonic rocks of northern Zacatecas and
 1137 adjacent areas, Mexico. US Geological Survey Professional Paper, C7–C10.

1138 Rubio Cisneros, I. I. (2012). Análisis de procedencia de las formaciones el Alamar, La Boca y La
 1139 Joya Noreste de México (triásico superior-jurásico medio) [Phd, Universidad Autónoma de Nuevo
 1140 León]. <http://eprints.uanl.mx/3223/>

1141 Rubio Cisneros, I. I., Ramírez Fernández, J. A., & García Obregón, R. (2011). Análisis preliminar
1142 de procedencia de rocas clásticas jurásicas del valle de Huizachal, Sierra Madre Oriental:
1143 Influencia del vulcanismo sinsedimentario y el basamento cristalino. *Boletín de La Sociedad*
1144 *Geológica Mexicana*, 63(2), 137–156.

1145 Rubio-Cisneros, I. I., & Lawton, T. F. (2011). Detrital zircon U-Pb ages of sandstones in
1146 continental red beds at Valle de Huizachal, Tamaulipas, NE Mexico: Record of Early-Middle
1147 Jurassic arc volcanism and transition to crustal extension. *Geosphere*, 7(1), 159–170.
1148 <https://doi.org/10.1130/GES00567.1>

1149 Salvador, A. (1987). Late Triassic-Jurassic Paleogeography and Origin of Gulf of Mexico Basin1.
1150 *AAPG Bulletin*, 71(4), 419–451. [https://doi.org/10.1306/94886EC5-1704-11D7-](https://doi.org/10.1306/94886EC5-1704-11D7-8645000102C1865D)
1151 [8645000102C1865D](https://doi.org/10.1306/94886EC5-1704-11D7-8645000102C1865D)

1152 SGM. (2023). Cartas impresas disponibles del Servicio Geológico Mexicano.
1153 <https://www.sgm.gob.mx/CartasDisponibles/>

1154 Shaanan, U., Rosenbaum, G., Li, P., & Vasconcelos, P. (2014). Structural evolution of the Early
1155 Permian Nambucca Block (New England Orogen, eastern Australia) and implications for oroclinal
1156 bending. *Tectonics*, 33(7), 1425–1443. <https://doi.org/10.1002/2013TC003426>

1157 Shaw, J., Johnston, S. T., Gutiérrez-Alonso, G., & Weil, A. B. (2012). Oroclines of the Variscan
1158 orogen of Iberia: Paleocurrent analysis and paleogeographic implications. *Earth and Planetary*
1159 *Science Letters*, 329–330, 60–70. <https://doi.org/10.1016/j.epsl.2012.02.014>

1160 Silva-Romo, G., Arellano-Gil, J., Mendoza-Rosales, C., & Nieto-Obregón, J. (2000). A submarine
1161 fan in the Mesa Central, Mexico. *Journal of South American Earth Sciences*, 13(4–5), 429–442.

1162 Silver, L. T., & Anderson, T. H. (1974). Possible left-lateralearly to middle Mesozoic disruption
1163 of the south-western North American craton margin, *Geological Society of America Abstracts and*
1164 *Programs*, 6, 955–956.

1165 Stern, R. J., & Dickinson, W. R. (2010). The Gulf of Mexico is a Jurassic backarc basin. *Geosphere*,
1166 6(6), 739–754. <https://doi.org/10.1130/GES00585.1>

1167 Sussman, A. J., & Weil, A. B. (2004). *Orogenic Curvature: Integrating Paleomagnetic and*
1168 *Structural Analyses*. Geological Society of America.

1169 Tarling, D., & Hrouda, F. (1993). *Magnetic Anisotropy of Rocks*. Springer Science & Business
1170 Media.

1171 Tauxe, L. (2010). *Essentials of Paleomagnetism*. Univ of California Press.

1172 Tauxe, L., & Watson, G. S. (1994). The fold test: An eigen analysis approach. *Earth and Planetary*
1173 *Science Letters*, 122(3), 331–341. [https://doi.org/10.1016/0012-821X\(94\)90006-X](https://doi.org/10.1016/0012-821X(94)90006-X)

1174 Torsvik, T. H., Van der Voo, R., Preeden, U., Mac Niocaill, C., Steinberger, B., Doubrovine, P.
1175 V., Van Hinsbergen, D. J., Domeier, M., Gaina, C., & Tohver, E. (2012). Phanerozoic polar wander,
1176 palaeogeography and dynamics. *Earth-Science Reviews*, 114(3–4), 325–368.

1177 Venegas Rodríguez, G., Barboza-Gudiño, J., & López-Doncel, R. (2009). Geochronology of
1178 detritic zircons in Lower Jurassic beds of the Sierra de Catorce and El Alamito areas, San Luis
1179 Potosí State. *Revista Mexicana de Ciencias Geológicas*, 26, 466–481.

1180 Weil, A. B., Gutiérrez-Alonso, G., & Wicks, D. (2013). Investigating the kinematics of local thrust
1181 sheet rotation in the limb of an orocline: A paleomagnetic and structural analysis of the Esla
1182 tectonic unit, Cantabrian–Asturian Arc, NW Iberia. *International Journal of Earth Sciences*, 102(1),
1183 43–60. <https://doi.org/10.1007/s00531-012-0790-3>

1184 Weil, A. B., Van der Voo, R., & van der Pluijm, B. A. (2001). Oroclinal bending and evidence
1185 against the Pangea megashear: The Cantabria-Asturias arc (northern Spain). *Geology*, 29(11),
1186 991–994. [https://doi.org/10.1130/0091-7613\(2001\)029<0991:OBAEAT>2.0.CO;2](https://doi.org/10.1130/0091-7613(2001)029<0991:OBAEAT>2.0.CO;2)

1187 Weil, A. B., & Yonkee, A. (2009). Anisotropy of magnetic susceptibility in weakly deformed red
1188 beds from the Wyoming salient, Sevier thrust belt: Relations to layer-parallel shortening and
1189 orogenic curvature. *Lithosphere*, 1(4), 235–256. <https://doi.org/10.1130/L42.1>

1190 Weil, A. B., Yonkee, A., & Sussman, A. (2010). Reconstructing the kinematic evolution of curved
1191 mountain belts: A paleomagnetic study of Triassic red beds from the Wyoming salient, Sevier
1192 thrust belt, U.S.A. *GSA Bulletin*, 122(1–2), 3–23. <https://doi.org/10.1130/B26483.1>

1193 Yonkee, A., & Weil, A. B. (2010). Reconstructing the kinematic evolution of curved mountain
1194 belts: Internal strain patterns in the Wyoming salient, Sevier thrust belt, U.S.A. *GSA Bulletin*,
1195 122(1–2), 24–49. <https://doi.org/10.1130/B26484.1>

1196 Yonkee, W. A., & Weil, A. B. (2015). Tectonic evolution of the Sevier and Laramide belts within
1197 the North American Cordillera orogenic system. *Earth-Science Reviews*, 150, 531–593.

1198 Zachary, D. W. (2012). Stratigraphic Controls on the Structural Evolution of the Sierra Madre
1199 Oriental Fold-thrust Belt, Eastern Mexico [Msc Thesis]. University of Houston.

1200 Zavala-Monsiváis, A., Barboza-Gudiño, J. R., Velasco-Tapia, F., & García-Arreola, M. E. (2012).
1201 Sucesión volcánica Jurásica en el área de Charcas, San Luis Potosí: Contribución al entendimiento
1202 del Arco Nazas en el noreste de México. *Boletín de La Sociedad Geológica Mexicana*, 64(3), 277–
1203 293.

1204 Zhou, Y., Murphy, M. A., & Hamade, A. (2006). Structural development of the Peregrina–
1205 Huizachal anticlinorium, Mexico. *Journal of Structural Geology*, 28(3), 494–507.

1206 Zijderveld, J. D. A. (1967). AC demagnetization of rocks: Analysis of results, *Methods in*
1207 *Paleomagnetism* DW Collinson, KM Creer, SK Runcorn, 254–286. Elsevier, New York.

1208

1209

1210

Supporting Information for

**THE SIERRA MADRE ORIENTAL OROCLINE.
PALEOMAGNETISM OF THE NAZAS SYSTEM IN NORTH-CENTRAL
MÉXICO**

Rafael Guerra Roel¹, Daniel Pastor Galán^{2,3}, Gabriel Chávez-Cabello⁴, César Francisco Ramírez-Peña⁴, José Jorge Aranda Gómez⁵, Gerardo Patiño Méndez ⁴, Giovanni Nova R.⁶, Alejandro Rodríguez-Parra⁷, Roberto Stanley Molina Garza†⁵.

1. Universidad Autónoma de Nuevo León, Posgrado de la Facultad de Ciencias de la Tierra. Carretera a Cerro Prieto Km 8, Ex. Hacienda de Guadalupe, Linares N.L., México, C.P. 67700.
2. Universidad de Granada. Facultad de Ciencias de la Universidad de Granada. Av. de Fuente Nueva, s/n, 18071 Granada, España.
3. Frontier Research Institute for Interdisciplinary Science, Tohoku University, Japan.
4. Universidad Autónoma de Nuevo León, Facultad de Ciencias de la Tierra. Carretera a Cerro Prieto Km 8, Ex. Hacienda de Guadalupe, Linares N.L., México, C.P. 67700.
5. Universidad Nacional Autónoma de México, Centro de Geociencias, Juriquilla, Qro. 76230, México.
6. Instituto de Geociências, Universida de de São Paulo. São Paulo, Brasil
- ⁷. Ministerio de Minas y Energía, Colombia; Calle 43 # 57 -31, Can, Bogota, Bogotá Colombia.

† Deceased

Contents of this file

Supporting Figures

- SF1 IRM Villa Juarez
- SF2 IRM San Julián Uplift
- SF3 Hysteresis Loops San Julián Uplift
- SF4a Curie curves Caopas
- SF4b Curie curves MSM
- SF5 Curie curves Villa Juarez
- SF6 Anisotropy of Magnetic Susceptibility graphs
- SF7 Scanning Electron Microscope Images
- SF8 Viscous Remanent Magnetization
- SF9 Huizachal Fold Test

Supporting Tables

ST1 Villa Juarez site means

ST2 San Julian Uplift site means

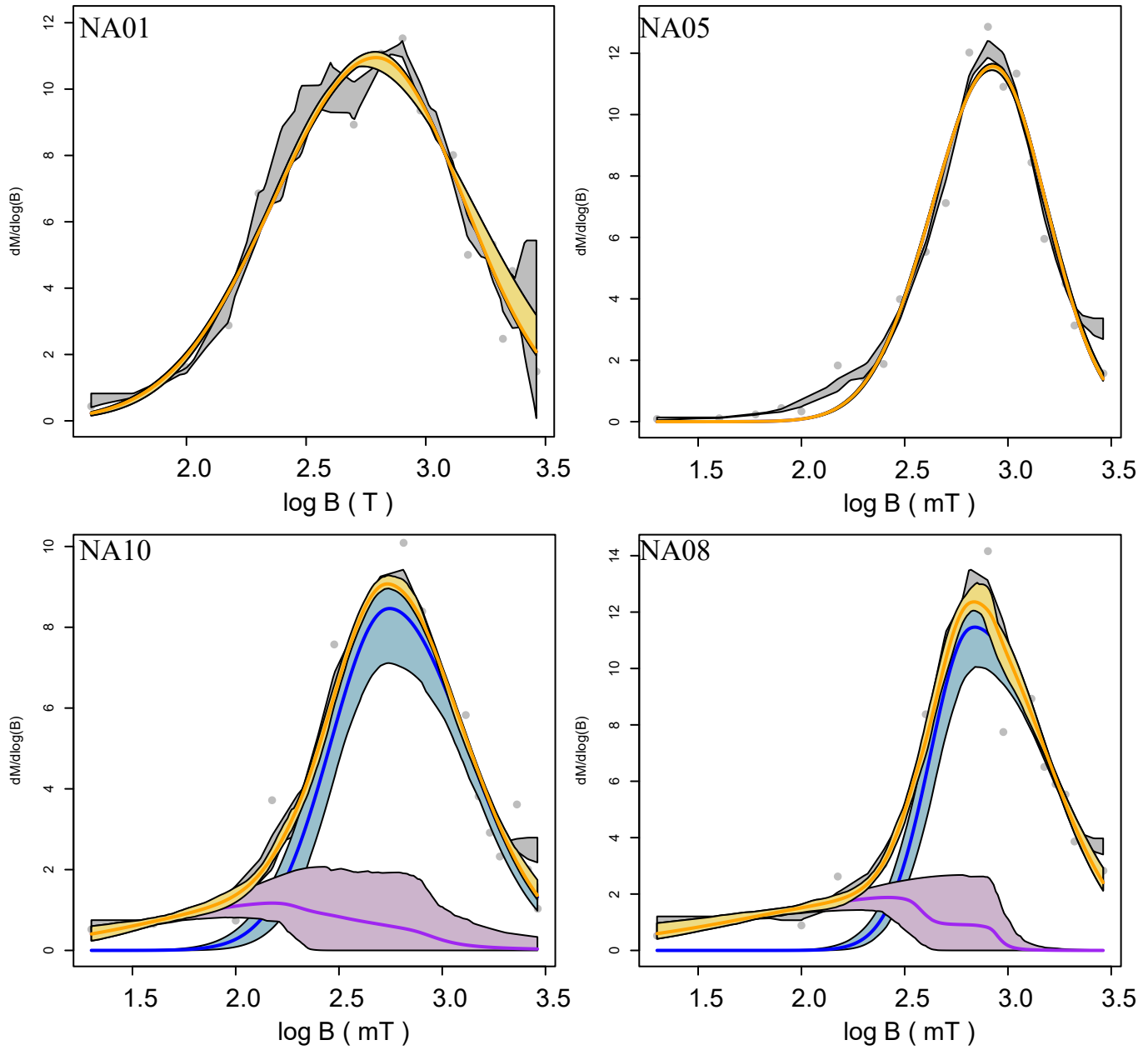
ST3-Charcas Site Means

ST4-Real de Catorce site means

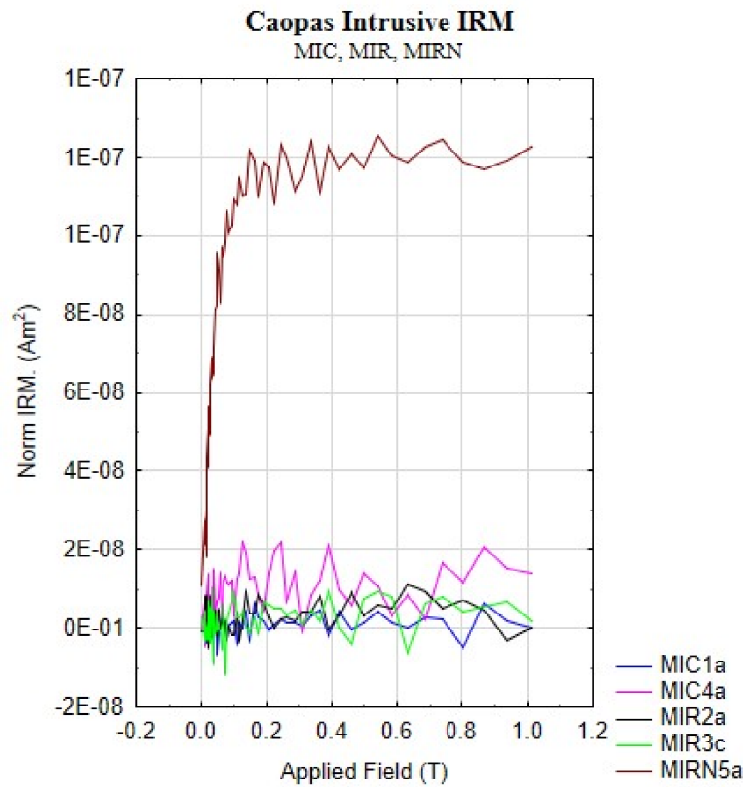
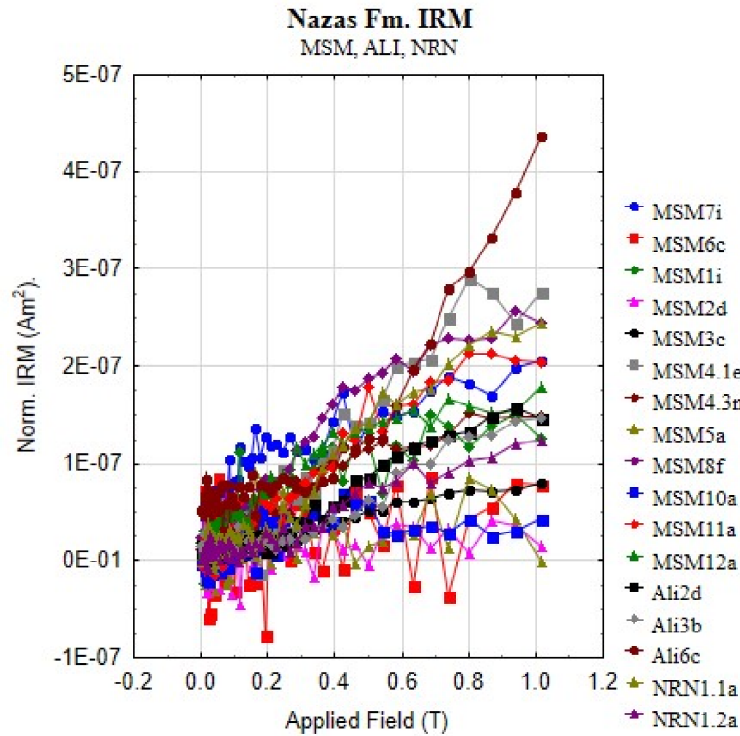
ST5-Huizachal site means

Introduction

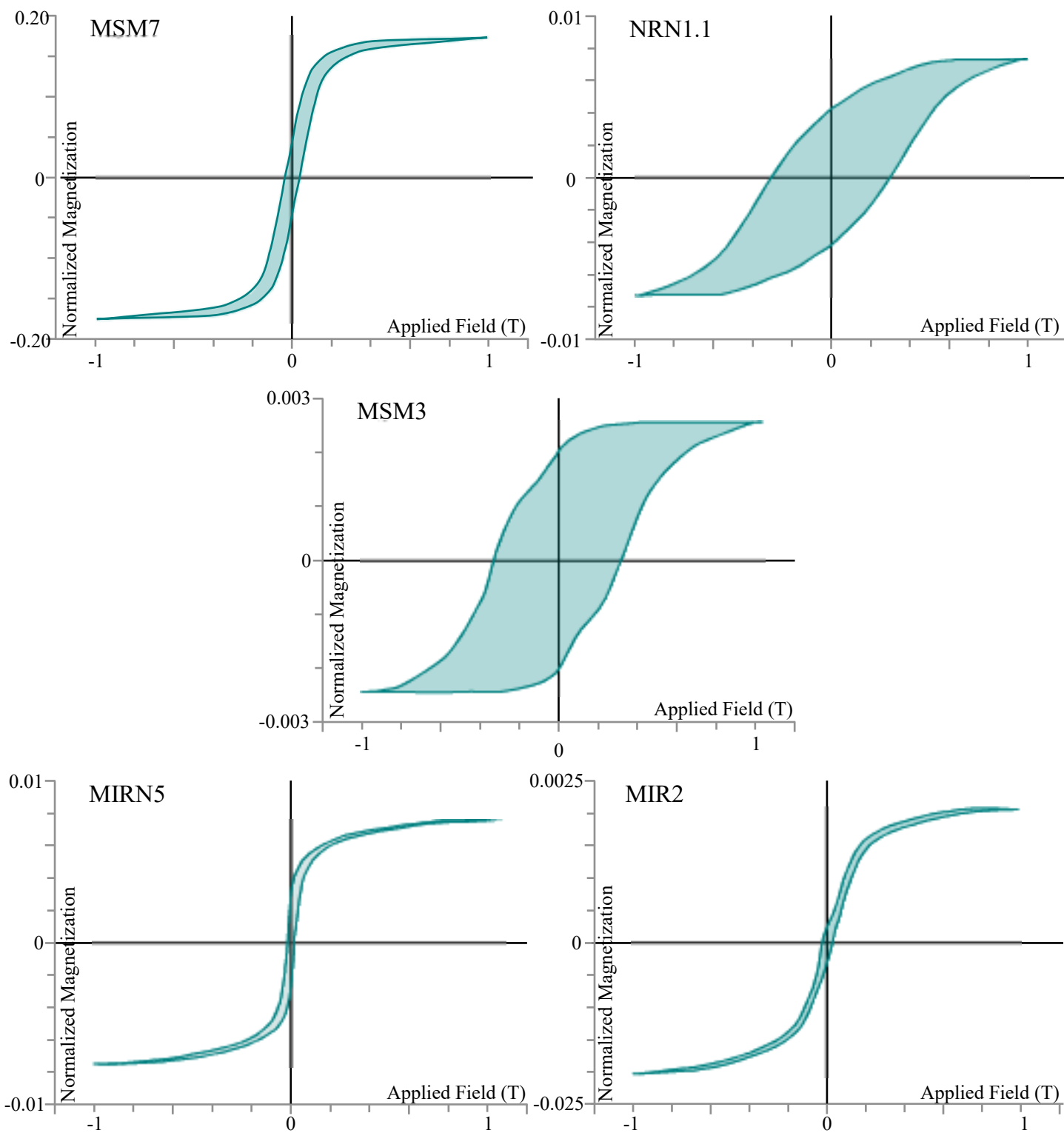
The figures and tables included here are supplementary to the main Rock magnetics and paleomagnetic analysis or are the raw uninterpreted results of the work. Here all of the graphs are included in the cases where only representative samples are shown in the manuscript.



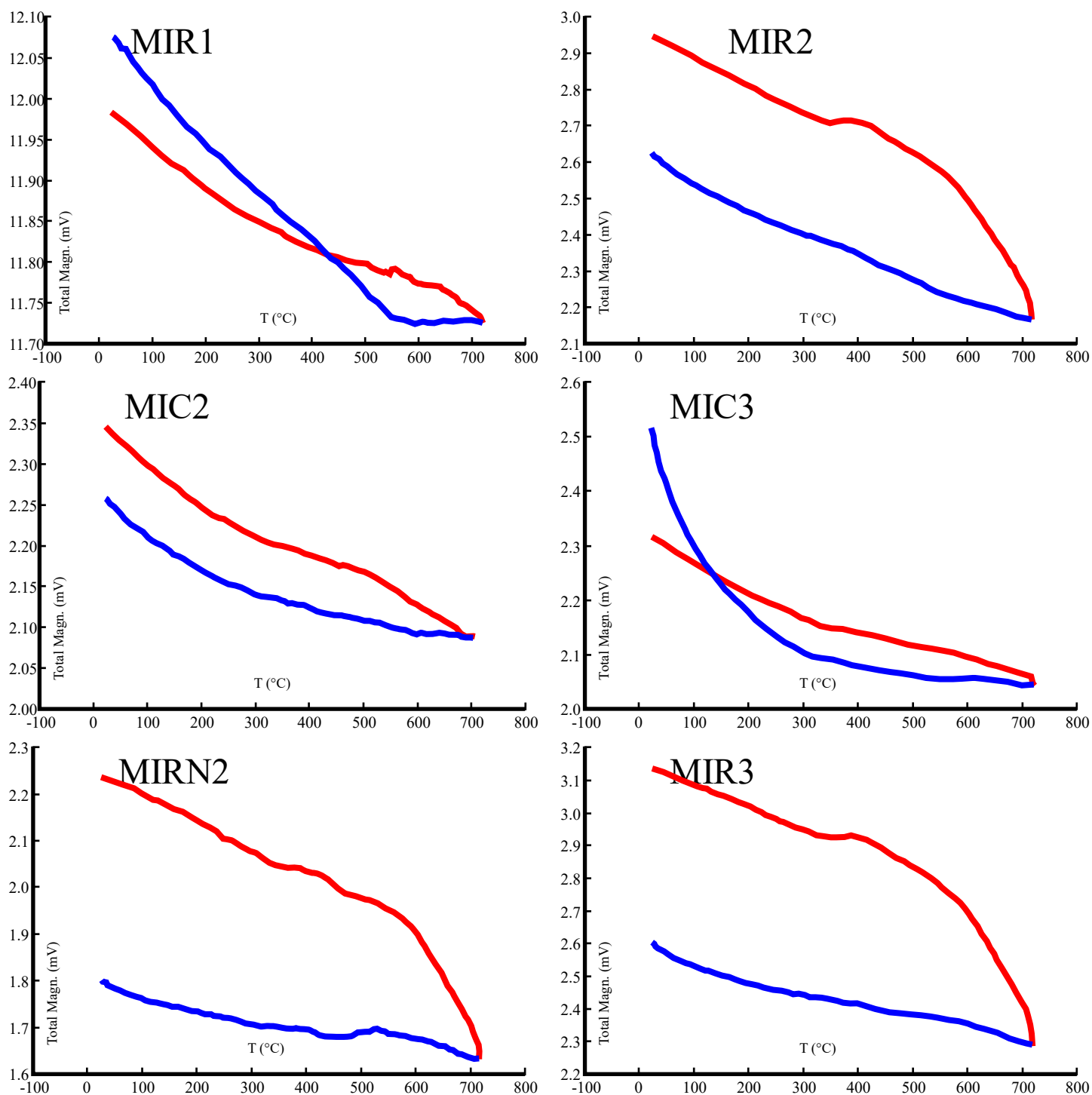
SF1. Gradient Acquisition plots of IRM acquisition curves of the Villa Juarez Locality using MAX UnMix (Maxbauer et al., 2016):Runs of representative samples of NA01, NA05, NA10 and NA08. Runs were carried in temperatures from 0° to 700°C in an Ar atmosphere. . Grey dots and the yellow curve represent the smoothed IRM data and modeled coercivity distribution, respectively. Shaded areas represent 95% confidence intervals associated with each component.



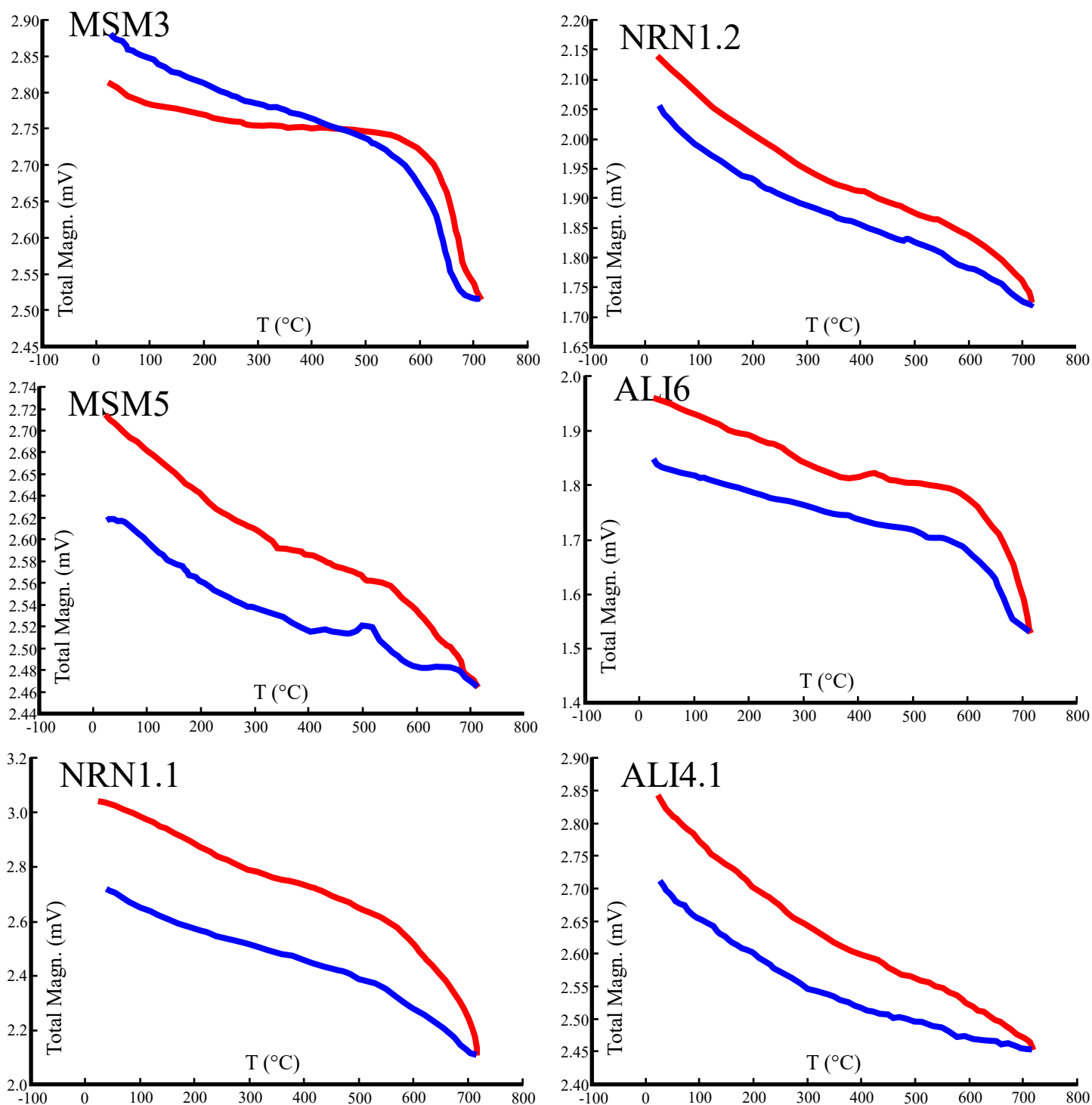
SF2. Isothermal remanent magnetization acquisition curves for the San Julián Uplift Locality (MSM, Caopas and Nazas North). They were obtained in a Micromag model 2900 with two Tesla magnets, Princeton Measurements Corporation, noise level $2 \times 10^{-9} \text{ Am}^2$. These tests were made at room temperature and a field of 1T was applied in 10mT increments



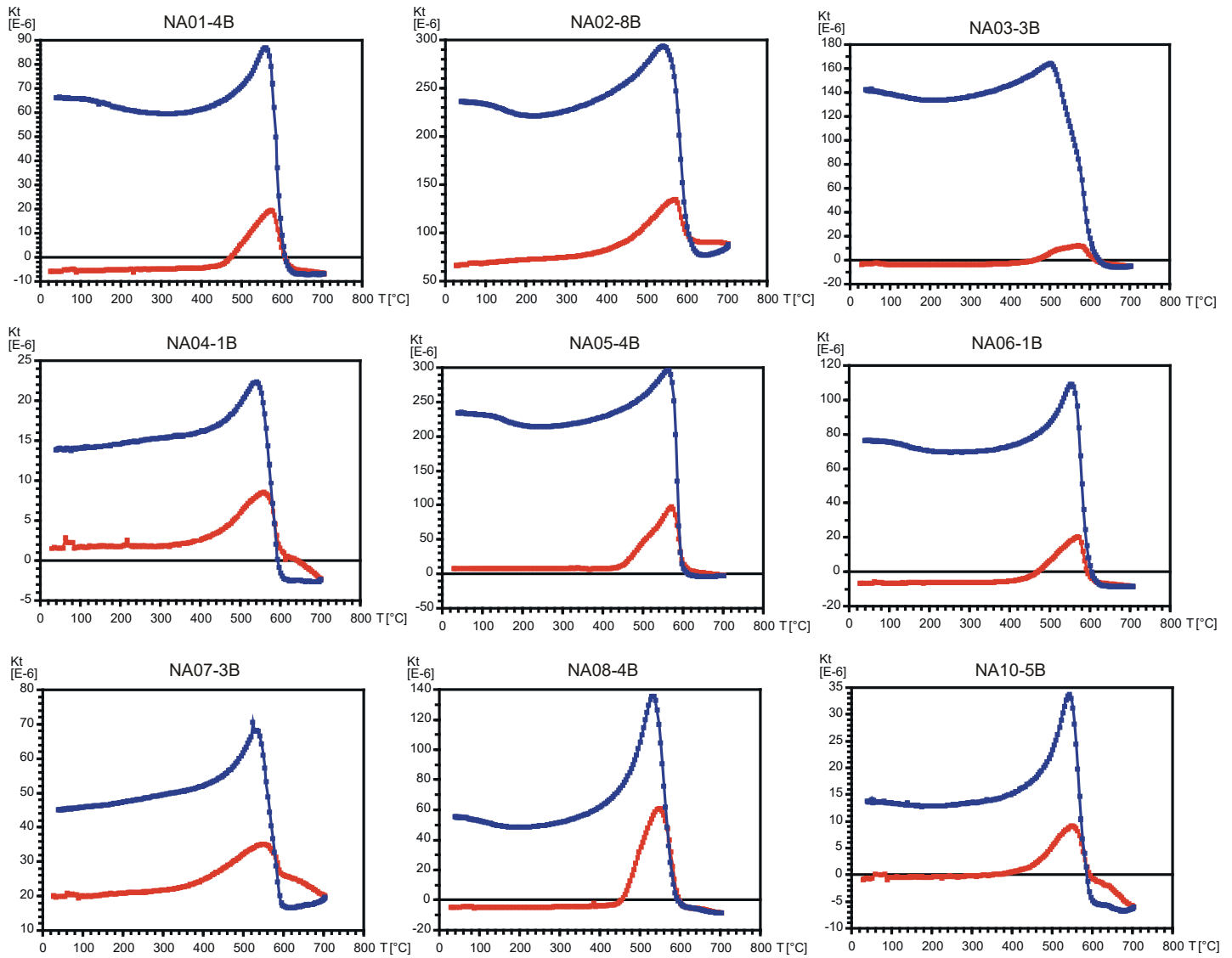
SF3. Hysteresis Loops of San Julián Uplift Locality (MSM and Nazas North): Thermomagnetic Runs of representative samples of MsM, NRN and ALI.



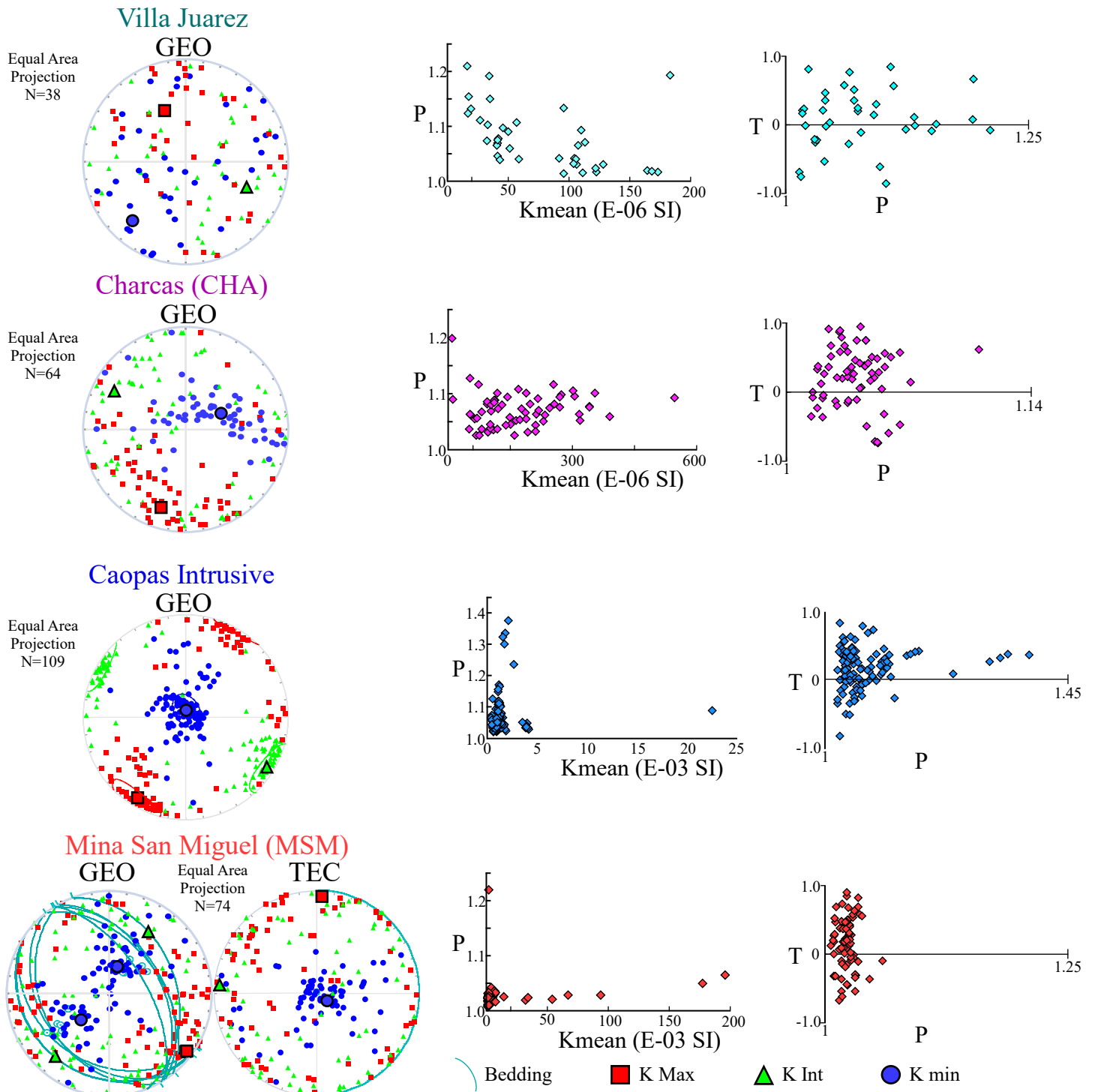
SF4a. Thermomagnetic Curves San Julián Uplift Locality (Caopas): Thermomagnetic Runs of representative samples MIR, MIRN and MIC.



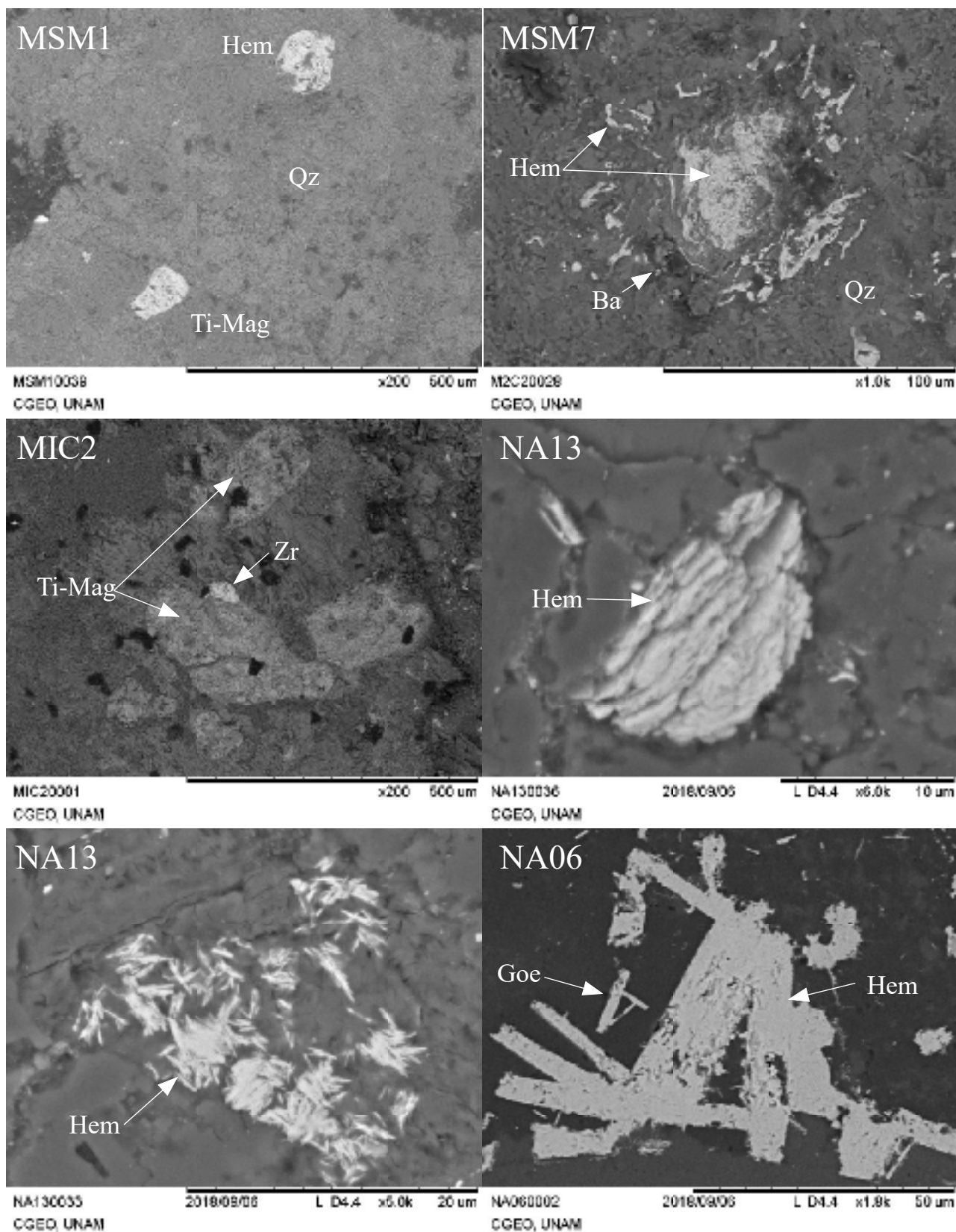
SF4b. Thermomagnetic Curves San Julián Uplift Locality (MSM and Nazas North): Thermomagnetic Runs of representative samples of MSM, NRN and ALI.



SF5. Thermomagnetic Curves Villa Juarez Locality Suseptibility vs Temperature: Thermomagnetic Runs of representative samples NA01-NA10.

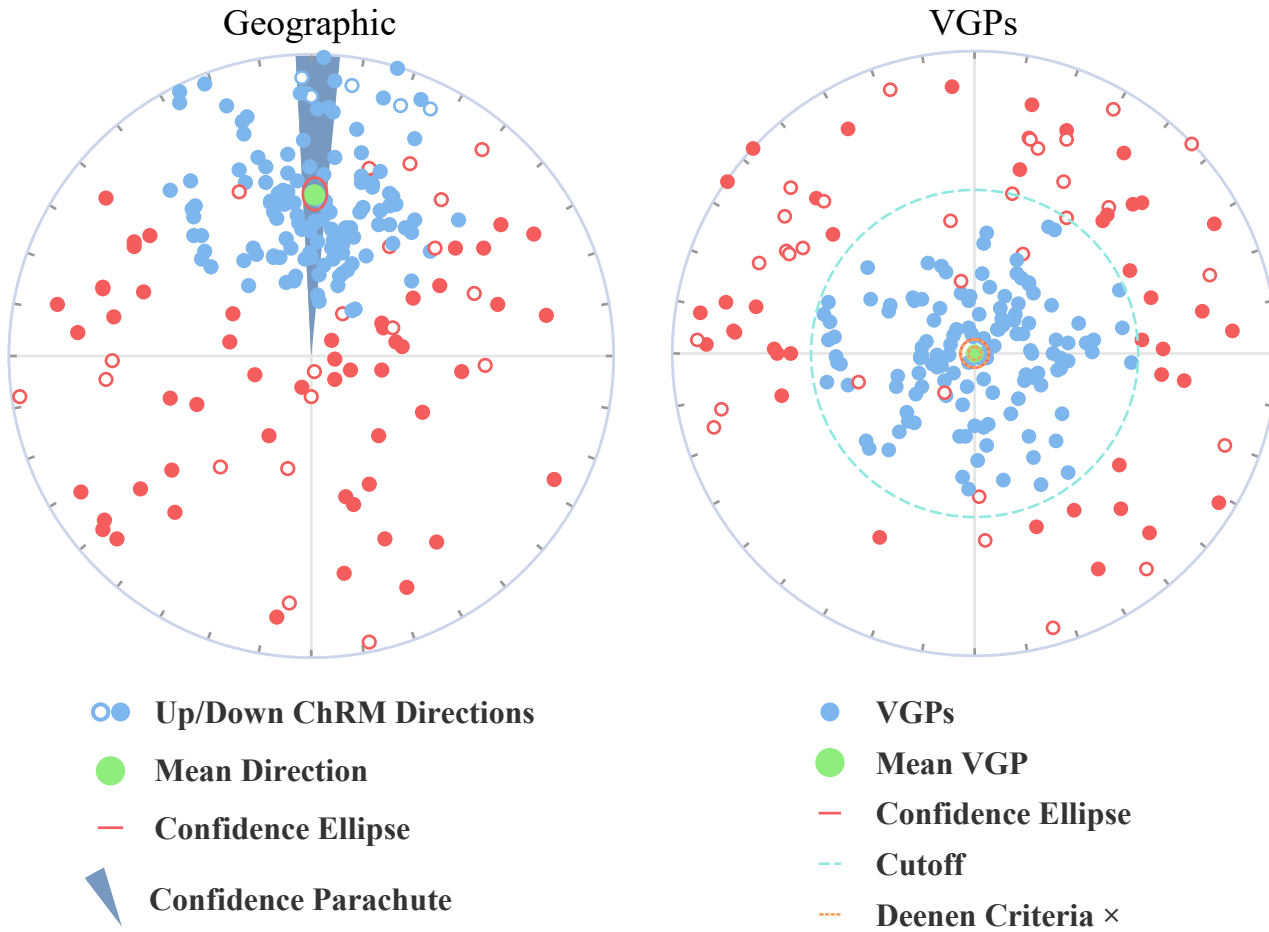


SF6. Anisotropy of Magnetic Suseptibility of the Villa Juárez, Charcas and San Julián Uplift Localites (MSM, Caopas): . Results are represented in an equal area projection for the analyzed sites. Larger symbols represent site mean. Light blue lines represent structural data. Shape parameter T vs Mean magnetic susceptibility K_m and shape parameter T vs Anisotropy parameter P graphs show low degree of anisotropy.



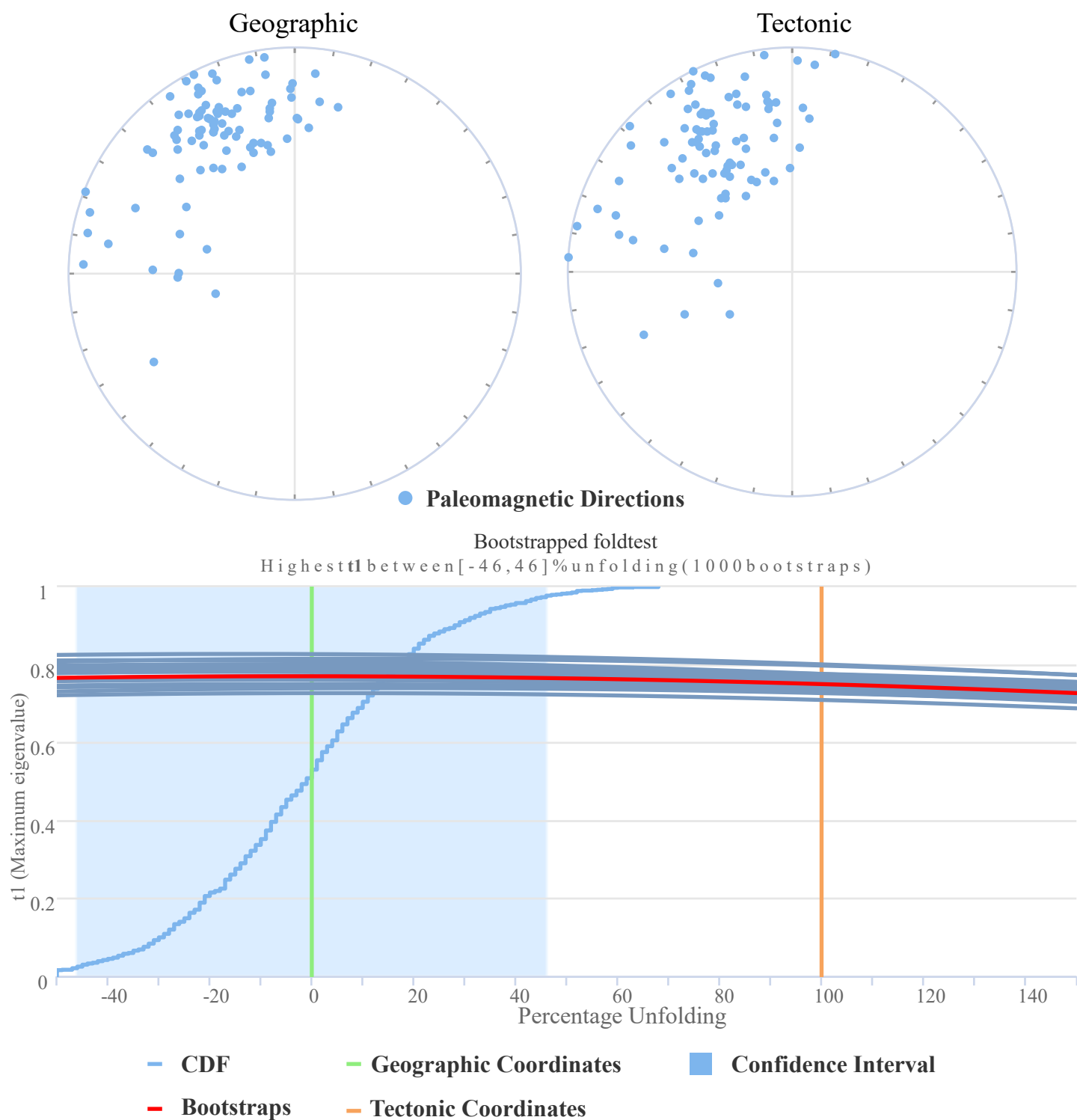
SF7. Scanning Electron Microscope images of selected samples from the Villa Juárez and San Julián Uplift localities. (**Hem**: hematite; **Mag**: Magnetite; **Ti-Mag**: Titanomagnetite; **Ba**: Barite; **Goe**: Goethite; **Qz**: Quartz).

Viscous Component



SF8. Viscous component present in all the samples collected in this work. This component was isolated below 200 °C and 16 mT. It resembles the present day magnetic field.

Huizachal Fold Test



SF9. Fold Test for the Huizachal locality. Inconclusive due to little to no change in the grouping of the geographic to the tilt corrected (Tectonic) directions.

Table ST1. Villa Juarez site mean directions in geographic coordinate system.

Geographic	N	Ns	mDec	mInc	k	a95	K	A95	A95		ΔD_x	ΔI_x	Pole Lng	Pole Lat	Coordinates	
									Min	Max					Lat.	Long.
NA-01	10	10	241.3	52.53	32.09	8.66	19.35	11.26	4.78	19.22	13.49	11.89	208.42	-6.39	25.495	-103.6
NA-02	11	11	263.1	62.28	136.1	3.93	67.28	5.61	4.6	18.1	7.75	4.62	209.16	12.61	25.495	-103.6
NA-03	8	8	152	-78.43	125.2	4.97	39.32	8.94	5.22	22.12	24.23	5.01	62	-44.09	25.495	-103.6
NA-04	6	6	175	-51.85	167.5	5.19	127.5	5.96	5.86	26.52	7.06	6.39	46.98	-81.64	25.497	-103.6
NA-05	6	8	9.6	10.73	29.75	12.49	72.54	7.92	5.86	26.52	7.95	15.43	48.58	68.79	25.492	-103.6
NA-06	7	7	0.02	30.98	156.7	4.84	345.1	3.25	5.51	24.07	3.4	5.22	76.2	81.35	25.498	-103.6
NA-07	12	12	305.1	65.84	36.52	7.28	20.82	9.74	4.44	17.14	14.68	7.32	211.14	42.42	25.519	-103.6
NA-08	5	5	14.41	58.14	18.9	18.06	11.78	23.26	6.3	29.75	30.45	21.35	289.06	73.02	25.511	-103.6
NA-10	8	8	257.4	83	58.89	7.28	17.26	13.72	5.22	22.12	83.97	7.16	241.6	21.96	25.508	-103.6
NA-12	2	2	344.6	24.8	46.6	37.45	47.4	37.12	9.09	52.99	38.27	64.44	128.09	71.04	25.526	-103.6
NA-13	1	1	277.4	12.98	0	NaN	NaN	NaN	12	82	NaN	NaN	169.15	9.51	25.544	-103.6
NA-17	5	5	331.9	33.15	224.3	5.12	404.8	3.81	6.3	29.75	4.01	5.91	156.34	62.89	25.516	-103.6

N number of demagnetized Specimens, *Ns* number of specimens that passed the Cutoff, *mDec* mean declination, *mInc* mean inclination, *k* recision parameter, *a95* radius of the 95% confidence cone about site-mean direction, *K* precision parameter of the poles, *A95* radius of 95% confidence circle around paleomagnetic pole, *A95min* and *A95max* describe the minimum and maximum values of *A95* allowed to considered the average representative. ΔD_x , uncertainty in declination; ΔI_x , uncertainty in inclination

Table ST2. San Julián Uplift site mean directions in geographic coordinate system.

Geographic	N	Ns	mDec	mInc	k	a95	K	A95	A95		ΔD_x	ΔI_x	Pole Lng	Pole Lat	Coordinates	
									Min	Max					Lat.	Long.
MSM1	9	13	296.21	15.53	26.28	10.23	47.57	7.54	4.98	20.54	7.61	14.27	170.14	9.3	24.9056	-102.154
MSM2	7	7	278.35	-2.02	55.17	8.2	166.7	4.69	5.51	24.07	4.69	9.37	163.44	7.19	24.901	-102.155
MSM3	5	5	291.2	8.53	453.94	3.6	591.5	3.15	6.3	29.75	3.16	6.19	162.69	21.02	24.895	-102.149
MSM4-1	5	5	270.07	-21.83	124.32	6.89	122.6	6.94	6.3	29.75	7.08	12.44	157.48	-4.63	24.895	-102.147
MSM4-2	5	5	274.03	47.56	95.3	7.88	63.78	9.65	6.3	29.75	11.02	11.42	193.1	14.79	24.895	-102.148
MSM4-3	14	14	289.57	35.35	26.35	7.89	22.99	8.47	4.18	15.55	8.99	12.69	178.83	25.76	24.895	-102.147
MSM5	6	6	287.82	18.63	204.13	4.7	263.74	4.13	5.86	26.52	4.19	7.63	169.3	20.15	24.892	-102.147
MSM6	6	6	294.27	12.59	46.92	9.88	94.96	6.91	5.86	26.52	6.95	13.33	163.42	24.78	24.892	-102.148
MSM7	6	6	286.05	-17.23	20.09	15.32	23.89	13.99	5.86	26.52	14.16	26.14	152.63	10.68	24.892	-102.148
MSM8	4	6	190.9	52.36	28.04	17.66	23.64	19.3	6.89	34.24	23.19	20.44	250.51	-20.24	24.888	-102.15
MSM9	6	6	274.55	35.75	18.5	15.99	23.07	14.25	5.86	26.52	15.16	21.2	185.84	12.7	24.888	-102.15
MSM10	4	4	276	49.39	13.97	25.48	10.43	29.87	6.89	34.24	35.21	33.92	195.35	17.21	24.887	-102.15
MSM11	6	6	285.92	34.43	44.59	10.14	42.91	10.34	5.86	26.52	10.94	15.73	179.51	22.04	24.885	-102.15
MSM12	6	6	287.22	37.04	24.39	13.84	20.81	15.03	5.86	26.52	16.09	21.88	180.86	24.21	24.884	-102.149
NRN1-2	4	4	102.14	-5.07	916.21	3.04	2253.6	1.94	6.89	34.24	1.94	3.85	344.98	-12.07	24.873	-102.2
NRN1-1	3	3	237.62	20.87	239.36	7.99	221.94	8.29	7.73	41.04	8.45	15.01	193.04	-23.48	24.873	-102.2
ALI6	3	3	247.3	23.37	70.48	14.8	75.22	14.32	7.73	41.04	14.65	25.25	188.98	-14.52	24.949	-102.238
ALI5	4	4	248.95	18.35	12.33	27.26	12.68	26.84	6.89	34.24	27.24	49.69	185.6	-14.07	24.954	-102.247
ALI4-2	3	3	332.9	20.46	100.81	12.34	125.72	11.04	7.73	41.04	11.23	20.06	143.57	60.48	24.953	-102.25
ALI4-1	4	4	273.61	11.61	21.8	20.13	48.59	13.31	6.89	34.24	13.39	25.82	171.81	6.03	24.953	-102.25
ALI3	4	4	216.97	34.82	336.22	5.02	257	5.74	6.89	34.24	6.08	8.68	215.08	-33.07	24.956	-102.253
ALI1	7	7	297.57	31.76	86.3	6.53	141.92	5.08	5.51	24.07	5.32	8.06	173.44	31.95	24.948	-102.261
MIC1	4	4	245.74	8.57	48.54	13.32	106.62	8.94	6.89	34.24	8.96	17.58	182.65	-19.81	24.818	-102.185
MIC2	8	8	284.04	26.56	16.84	13.9	21.77	12.14	5.22	22.12	12.52	20.64	176.09	18.72	24.816	-102.186
MIC3	8	8	280.89	8.65	6.89	22.74	8.64	19.98	5.22	22.12	20.04	39.28	167.33	12	24.815	-102.188
MIC4	7	7	266.54	15.8	42.23	9.4	86.07	6.54	5.51	24.07	6.61	12.36	176.74	0.24	24.813	-102.19
MIC6	4	4	213.38	29.03	127.8	8.16	361.75	4.84	6.89	34.24	5.02	7.97	215.47	-38.07	24.8	-102.201
MIC7	4	4	269.96	17.94	23.32	19.44	27.8	17.74	6.89	34.24	17.98	32.95	176.41	3.62	24.801	-102.198
MIR1	4	6	304.23	-8.69	4.22	50.95	6.46	39.19	6.89	34.24	39.33	77.05	164.17	7.64	24.856	-102.194
MIR2	2	4	281.48	21.37	72.88	29.69	70.67	30.16	9.09	52.99	30.79	54.31	209.43	44.63	24.8472	-102.2
MIR3	6	6	294.47	25.32	4.38	36.2	6.69	27.96	5.86	26.52	28.8	48.25	173.38	28.37	24.843	-102.208
MIR4	4	4	193.23	47.84	181.72	6.83	194.82	6.6	6.89	34.24	7.54	7.76	243.76	-34.61	24.836	-102.213
MIR5	2	2	273.86	36.21	15.17	69.36	17.7	63.4	9.09	52.99	72.21	93.62	184.99	12.89	24.831	-102.217
MIRN3	2	2	272.43	24.98	17.04	64.82	22.76	55.03	9.09	52.99	57.29	95.35	179.28	7.22	24.875	-102.228
MIRN4	2	2	331.71	41.24	9.15	95.67	7.2	114.69	9.09	52.99	82.79	154.6	172.71	62.67	24.88	-102.235
MIRN5	4	4	240.5	4.39	477.33	4.21	836.72	3.18	6.89	34.24	3.18	6.33	183.3	-25.48	24.88	-102.235

MIRN7	4	4	300.1	19.92	5.42	43.56	7.73	35.35	6.89	34.24	36.01	64.54	166.27	32.82	24.884	-102.248
-------	---	---	-------	-------	------	-------	------	-------	------	-------	-------	-------	--------	-------	--------	----------

N number of demagnetized Specimens, *Ns* number of specimens that passed the Cutoff, *mDec* mean declination, *mInc* mean inclination, *k* recision parameter, *a95* radius of the 95% confidence cone about site-mean direction, *K* precision parameter of the poles, *A95* radius of 95% confidence circle around paleomagnetic pole, *A95min* and *A95max* describe the minimum and maximum values of *A95* allowed to considered the average representative. ΔD_x , uncertainty in declination; ΔI_x , uncertainty in inclination

Table ST3. Charcas site mean directions in Geographic coordinate system.

Geographic	N	Ns	mDec	mInc	k	a95	K	A95	A95		ΔD_x	ΔI_x	Pole Lng	Pole Lat	Coordinates	
									Min	Max					Lat.	Long.
CHA1	5	6	238.9	38.67	73.98	8.95	62.03	9.79	6.3	29.75	10.55	13.85	203.9	-16.97	23.106	-101.2
CHA2	7	11	135.5	-33.47	25.19	12.26	21.9	13.19	5.51	24.07	13.9	20.36	347.31	-13.16	23.106	-101.2
CHA3	5	5	9.97	3.86	245.2	4.9	278.5	4.59	6.3	29.75	4.6	9.16	52.84	66.73	23.096	-101.2
CHA4	6	6	23.31	-4.8	66.8	8.26	105.8	6.54	5.86	26.52	6.55	13.02	34.07	55.83	23.096	-101.2
CHA5	6	6	26.44	-10.11	91.94	7.02	154.8	5.4	5.86	26.52	5.42	10.55	33.03	51.68	23.096	-101.2
CHA6	4	5	25.92	-2.79	123.9	8.29	190.5	6.67	6.89	34.24	6.68	13.32	15.17	45.93	23.096	-101.2
CHA7	6	6	26.54	-5.54	114	6.3	207.1	4.67	5.86	26.52	4.67	9.27	30.36	53.4	23.096	-101.2
CHA8	4	4	29.92	-1.81	265.1	5.65	372.8	4.76	6.89	34.24	4.77	9.52	24.23	52.28	23.096	-101.2
CHA9	5	6	13.48	-14.03	79.25	8.65	89.09	8.15	6.3	29.75	8.21	15.58	37.92	53.34	23.096	-101.2
CHA10	5	5	20.63	-2.85	53.48	10.56	82.04	8.5	6.3	29.75	8.5	16.96	36.69	58.3	23.096	-101.2

N number of demagnetized Specimens, *Ns* number of specimens that passed the Cutoff, *mDec* mean declination, *mInc* mean inclination, *k* recision parameter, *a95* radius of the 95% confidence cone about site-mean direction, *K* precision parameter of the poles, *A95* radius of 95% confidence circle around paleomagnetic pole, *A95min* and *A95max* describe the minimum and maximum values of *A95* allowed to considered the average representative. ΔD_x , uncertainty in declination; ΔI_x , uncertainty in inclination

Table ST4. Real de Catorce site mean directions in geographic coordinate system.

Geographic	N	Ns	mDec	mInc	k	a95	K	A95	A95		ΔD_x	ΔI_x	Pole Lng	Pole Lat	Coordinates	
									Min	Max					Lat.	Long.
RC11-R	5	5	162.9	-33.04	133	6.66	246.3	4.88	6.3	29.75	5.14	7.59	333.28	-73.12	23.7	-100.9
RC11-N	3	3	354.4	46.44	40.72	19.57	26.69	24.35	7.73	41.04	27.77	29.52	208.76	83.39	23.7	-100.9
RC12-R	7	7	162.8	-40.01	399.4	3.02	601	2.46	5.51	24.07	2.67	3.4	349.44	-74.25	23.7	-100.9
RC13-R	9	9	171.3	-39.56	217.6	3.5	221.2	3.47	4.98	20.54	3.75	4.83	342.58	-81.88	23.7	-100.9
RC14-R	5	5	160.5	-42	282.6	4.56	349.3	4.1	6.3	29.75	4.5	5.45	355.14	-72.09	23.7	-100.9
RC14-N	2	2	22.62	57.54	167.7	19.41	141	21.19	9.09	52.99	27.37	19.76	306.29	65.84	23.7	-100.9
RC15-R	6	6	136.9	-52.6	82.27	7.43	46.9	9.88	5.86	26.52	11.84	10.41	13.33	-50.93	23.7	-100.9
RC15-N	2	2	356.2	29.94	8.77	98.54	11.48	82.27	9.09	52.99	NaN	133.8	116.56	81.67	23.7	-100.9
RC16-R	6	6	151.9	-59.04	49.98	9.57	29.32	12.58	5.86	26.52	16.47	11.28	31.04	-60.49	23.7	-100.9
RC16-N	1	1	348.4	30.32	0	NaN	NaN	NaN	12	82	NaN	NaN	137.06	76.83	23.7	-100.9
RC17-R	7	7	175.4	-49.35	120.9	5.51	85.3	6.57	5.51	24.07	7.61	7.47	48.74	-82.21	23.7	-100.9
RC17-N	6	6	20.56	26.61	94.73	6.92	160.3	5.31	5.86	26.52	5.47	9.02	11.61	68.47	23.7	-100.9
RC18-R	6	6	174.1	-46.14	118.3	6.18	104.2	6.59	5.86	26.52	7.44	8.04	26.92	-83.16	23.701	-100.9
RC19-R	6	7	170.5	-43.66	71.58	7.97	73.21	7.88	5.86	26.52	8.74	10.13	26.1	-74.72	23.701	-100.9
RC21-R	6	6	173.1	-42.04	511.5	2.97	672.5	2.59	5.86	26.52	2.84	3.43	356.29	-83.7	23.701	-100.9
RC22-R	5	5	163.8	-44.24	90.86	8.07	71.2	9.13	6.3	29.75	10.16	11.59	1.66	-74.83	23.701	-100.9
RC23-R	6	6	170.9	-36.66	133.1	5.83	134.9	5.79	5.86	26.52	6.18	8.48	329.79	-81.14	23.701	-100.9
RC24-R	6	6	171.2	-31.67	16.91	16.77	24.3	13.87	5.86	26.52	14.52	22	320.29	-79.43	23.701	-100.9
RC25-R	4	4	169.3	-34.87	128.1	8.15	131.4	8.04	6.89	34.24	8.52	12.14	327.36	-79.07	23.702	-100.9
RC26-R	5	6	175.8	-40.02	301.8	4.41	280.5	4.58	6.3	29.75	4.96	6.32	57.31	-79.94	23.702	-100.9

N number of demagnetized Specimens, *Ns* number of specimens that passed the Cutoff, *mDec* mean declination, *mInc* mean inclination, *k* recision parameter, *a95* radius of the 95% confidence cone about site-mean direction, *K* precision parameter of the poles, *A95* radius of 95% confidence circle around paleomagnetic pole, *A95min* and *A95max* describe the minimum and maximum values of *A95* allowed to considered the average representative. ΔD_x , uncertainty in declination; ΔI_x , uncertainty in inclination

Table ST5. Huizachal site mean directions in geographic coordinate system.

Geographic	N	Ns	mDec	mInc	k	a95	K	A95	A95		ΔD_x	ΔI_x	Pole Lng	Pole Lat	Coordinates	
									Min	Max					Lat.	Long.
HUI28	5	5	155.1	-25.99	22.97	16.31	31.9	13.75	6.3	29.75	14.17	23.55	333.94	-64.25	23.588	-99.22
HUI29	6	6	98.71	3.74	21.35	14.84	28.56	12.75	5.86	26.52	12.76	25.42	345.59	-7.23	23.589	-99.22
HUI31	5	5	147.6	-30.56	54.51	10.46	55.69	10.34	6.3	29.75	10.79	16.67	343.73	-59.13	23.589	-99.22
HUI32-5	6	7	113.2	-1.76	4.42	35.98	10.48	21.71	5.86	26.52	21.71	43.38	331.83	-18.81	23.589	-99.22
HUI35	7	7	121	20.77	8.6	21.83	13.47	17.06	5.51	24.07	17.37	30.9	326.22	-22.56	23.589	-99.22
HUI36	7	7	86.12	7.99	9.54	20.6	18.11	14.57	5.51	24.07	14.61	28.72	348.02	5.31	23.589	-99.22
HUI37	6	6	158.6	-33.73	88.31	7.17	127.3	5.96	5.86	26.52	6.29	9.16	340.85	-69.65	23.59	-99.22
HUI38	7	7	164.5	-36.34	25	12.31	24.19	12.52	5.51	24.07	13.36	18.45	341.48	-75.58	23.59	-99.22
HUI40	7	7	86.05	12.42	18.67	14.34	26.19	12.02	5.51	24.07	12.09	23.2	346.44	6.55	23.59	-99.22
HUI42	6	7	357	60.25	24.69	13.75	12.86	19.41	5.86	26.52	26.21	16.88	254.54	65.25	23.585	-99.23
HUI43	4	4	149.9	-10.66	70.77	11	138.3	7.84	6.89	34.24	7.87	15.28	323.53	-55.76	23.585	-99.23
HUI44	5	5	175.7	-29.78	46.94	11.28	52.12	10.7	6.3	29.75	11.13	17.44	291.7	-81.44	23.584	-99.23
HUI45	5	5	357.4	43.1	56.51	10.27	58.84	10.06	6.3	29.75	11.12	13.07	209.67	86.42	23.584	-99.23
HUI46	5	5	150.6	-20.98	38.28	12.52	38.71	12.45	6.3	29.75	12.68	22.51	331.42	-59.31	23.584	-99.23
HUI47	5	6	164.9	-21.39	39.98	12.25	53.36	10.57	6.3	29.75	10.77	19.03	312.25	-66.06	23.584	-99.24
HUI48	6	7	161.6	-17.57	12.27	19.91	18.96	15.79	5.86	26.52	15.99	29.42	323.85	-65.65	23.584	-99.24

N number of demagnetized Specimens, *Ns* number of specimens that passed the Cutoff, *mDec* mean declination, *mInc* mean inclination, *k* recision parameter, *a95* radius of the 95% confidence cone about site-mean direction, *K* precision parameter of the poles, *A95* radius of 95% confidence circle around paleomagnetic pole, *A95min* and *A95max* describe the minimum and maximum values of *A95* allowed to considered the average representative. ΔD_x , uncertainty in declination; ΔI_x , uncertainty in inclination

